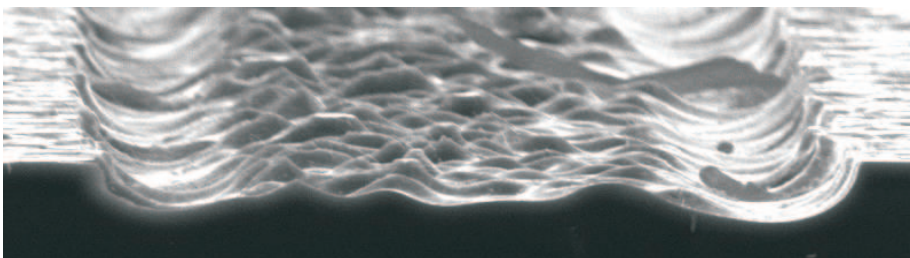
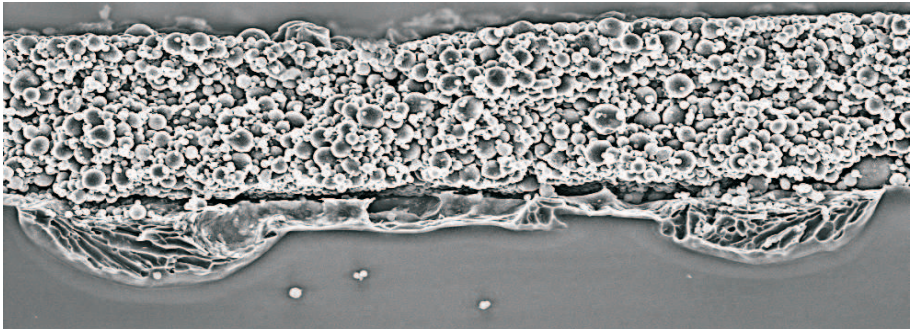


Elías Urrejola Davanzo

# **Aluminum-Silicon Contact Formation Through Narrow Dielectric Openings**

---

Application To Industrial High Efficiency Rear  
Passivated Solar Cells





# **Aluminum-Silicon Contact Formation Through Narrow Dielectric Openings**

---

Application To Industrial High Efficiency Rear  
Passivated Solar Cells

## **Dissertation**

zur Erlangung des akademischen Grades  
eines Doktors der Naturwissenschaften (Dr. rer. nat.)  
an der Universität Konstanz  
Mathematisch-Naturwissenschaftliche Sektion  
Fachbereich Physik

vorgelegt von

**Elías Urrejola Davanzo**

geboren am 21.02.1981 in Santiago, Chile

1. Referent: Prof. Dr. Ernst Bucher
  2. Referent: Apl. Prof. Dr. Johannes Boneberg
- Tag der mündlichen Prüfung: 23.05.2012



*a mis padres,  
inspiradores de toda luz,  
Manuel y Susi,  
con amor*

*"Renewable energies are inexhaustible. They do not destroy the environment. They are available everywhere. Their use facilitates solidarity with future generations. They secure the future of humankind."*

–Hermann Scheer, winner of the Right Livelihood Award  
(The 'Alternative Nobel Prize')



# CONTENTS

<b>1</b>	<b>Introduction</b>	<b>1</b>
1.1	Abstract	1
1.2	Motivation: Contact Formation for Rear Passivated Solar Cells	2
1.3	Outline of the Thesis	5
<b>I</b>	<b>Basic Principles and Processing of Silicon Solar Cells</b>	<b>7</b>
<b>2</b>	<b>Processing of an Industrial Solar Cell</b>	<b>9</b>
2.1	Introduction	9
2.2	Preparation of the Surfaces (Cleaning)	10
2.3	Texturing and Polishing	11
2.4	POCl <sub>3</sub> Diffusion	12
2.5	Antireflection Coating	12
2.5.1	Plasma Silicon Nitride Deposition	14
2.6	Thermal Oxidation	14
2.7	Screen-printing Metallization and Sintering of Contacts	15
2.8	Edge Isolation	15
2.9	Dielectric Ablations	15
2.9.1	Etching Paste	16
2.9.2	Some Etchants of Dielectrics	17
<b>3</b>	<b>Basic Principles of Solar Cells</b>	<b>19</b>
3.1	Characterization of Solar Cells	20
3.1.1	<i>I-V</i> -Characteristic	20
3.1.2	Spectral Response	21
3.1.3	Short-Circuit Current Density	23
3.1.4	A few Characterization Tools	24
3.2	Loss Mechanisms of Solar Cells	25
3.2.1	Series Resistance Losses	25
3.2.2	Recombination in Solar Cells	30
3.3	Light Absorption of the Silicon Material	33
3.4	The Two Diode Model	34
<b>4</b>	<b>Selective Emitter Solar Cells</b>	<b>37</b>
4.1	The Selective Emitter Concept	38
4.2	Experimental Part	38
4.3	Screen Printing Approach: Etching of Dielectric Barriers	40
4.3.1	Fiducial Alignment	40
4.3.2	Etching Paste and Alignment Approach	40
4.4	Solar Cell Results	42
4.4.1	<i>I-V</i> Characterization	42

4.4.2	Spectral Response Characterization . . . . .	42
4.5	Conclusions and Discussion . . . . .	43
<b>II</b>	<b>Aluminum-Silicon Contact Formation</b>	<b>45</b>
<b>5</b>	<b>Contact Formation, State of the Art</b>	<b>47</b>
5.1	The High-Low Junction as a Back Surface Field . . . . .	47
5.2	Effect of the BSF on $V_{OC}$ . . . . .	49
5.3	Gettering Properties of Al . . . . .	50
5.4	Fundamental Mechanisms of Al-Si Contact Formation . . . . .	51
5.5	Al-Si Lamellas . . . . .	55
5.6	Screen Printing and Drying of Aluminum Lines . . . . .	56
<b>6</b>	<b>Aluminum-Silicon Contact Formation through Narrow Dielectric Openings</b>	<b>59</b>
6.1	Introduction . . . . .	60
6.2	Preparation of the Surfaces . . . . .	61
6.3	Study 1: Local Al-Si Alloy Formation . . . . .	62
6.3.1	Experimental Design . . . . .	62
6.3.2	Impact of Al amount on Contact Formation . . . . .	63
6.3.3	Impact of Contact Width on Alloy Formation . . . . .	66
6.3.4	Cross-sectional SEM/EDX Analysis of the Alloy Junction . . . . .	67
6.3.5	On the Variation of the Contact Resistivity . . . . .	70
6.3.6	Experimental Evidence of the Influence of Al Amount on Mass Transport . . . . .	72
6.3.7	Conclusions . . . . .	72
6.4	Study 2: Diffusion of Silicon into Aluminum . . . . .	74
6.4.1	Experimental Design . . . . .	74
6.4.2	On the Spread of Si in Al and the Formation of Voids . . . . .	75
6.4.3	Discussion . . . . .	78
6.4.4	Model of Local Contact Formation . . . . .	79
6.4.5	Summary and Conclusions . . . . .	80
6.5	Study 3: Distribution of Silicon in Aluminum . . . . .	82
6.5.1	Experimental Design . . . . .	82
6.5.2	Influence of Contact Pattern on Contact Formation . . . . .	83
6.5.3	Distribution of Si in Al Paste . . . . .	86
6.5.4	Phenomenon of Lateral Solidification . . . . .	86
6.5.5	Summary and Conclusions . . . . .	88
6.6	Study 4: Effect of Gravity on the Microstructure of Al-Si Alloy . . . . .	89
6.6.1	Experimental Design . . . . .	89
6.6.2	Cross-sectional SEM Analysis . . . . .	90
6.6.3	Summary and Conclusions . . . . .	92
6.7	Understanding and Avoiding the Formation of Voids . . . . .	93
6.7.1	Formation of Voids with and without Back Surface Field . . . . .	93
6.7.2	How to Reduce the Void Formation for Rear Passivated Solar Cells . . . . .	94
6.7.3	Summary and Conclusions . . . . .	95

---

<b>III Analysis of Industrial Rear Passivated Solar Cells</b>	<b>97</b>
<b>7 Processing of Rear Passivated Solar Cells</b>	<b>99</b>
7.1 Introduction . . . . .	100
7.2 Material . . . . .	100
7.3 Inline Phosphorous Gettering on As-Cut mc-Si . . . . .	101
7.4 Surface Roughness of Polished mc-Si . . . . .	102
7.5 Reflectivity of Studied Si Surfaces . . . . .	104
7.6 Homogeneity of the Phosphorus Emitter Layer . . . . .	106
7.7 Silver Pad Metallization for Module Assembly . . . . .	107
7.8 Study 1: Single Side Polishing before POCl <sub>3</sub> Diffusion . . . . .	111
7.8.1 Introduction . . . . .	111
7.8.2 Preparation of the Samples . . . . .	111
7.8.3 I-V Results and Discussions . . . . .	113
7.8.4 Analysis of Dislocations in mc-Si . . . . .	116
7.8.5 Summary and Conclusions . . . . .	118
7.9 Study 2: Front Side Emitter Masking Approach . . . . .	119
7.9.1 Introduction . . . . .	119
7.9.2 Preparation of the Samples . . . . .	119
7.9.3 I-V Measurements and Discussions . . . . .	121
7.9.4 Characterization of Solar Cells through FF . . . . .	123
7.9.5 Spectral Response Characterization . . . . .	124
7.9.6 Summary and Conclusions . . . . .	126
7.10 High Efficiency Industrial Solar Cell with PECVD-Based Rear Surface Passivation . . . . .	127
7.10.1 Introduction . . . . .	127
7.10.2 Preparation of the Samples . . . . .	127
7.10.3 Results and Discussions . . . . .	128
7.10.4 Electroluminescence Analysis . . . . .	129
7.10.5 Summary and Conclusions . . . . .	130
<b>Thesis Summary and Outlook</b>	<b>131</b>
<b>Zusammenfassung (German Summary)</b>	<b>133</b>
<b>Bibliography</b>	<b>135</b>
<b>List of Figures</b>	<b>149</b>
<b>Lists of Acronyms and Symbols</b>	<b>151</b>
<b>List of Publications</b>	<b>155</b>
<b>Acknowledgments</b>	<b>157</b>
<b>Curriculum</b>	<b>159</b>



## INTRODUCTION

### 1.1 Abstract

Throughout the last century - the oil era - the normal climate fluctuations of planet Earth have been strongly affected by anthropogenic carbon dioxide emissions [1]. Convincing evidence has been given lately by several scientific studies on climate change by anthropogenic global warming [2,3]. The severe impact of this phenomenon on wild animals, plants and ecosystems has been extensively studied [4]. The projected impact on the environment as melting glaciers, decreasing drinking water supplies, sea-level rising, and extreme temperatures will not only affect nature but us - human beings [5], far less adaptable than nature. However, it will be the future generations that will have to deal with the consequences. Changes in the ecosystem may be irreversible, however, it is well-known that a complete change to renewable energies will strongly reduce the anthropogenic emission of greenhouse gases [9].

The potential of renewable energies (specially solar energy) to be used as a clean and powerful source of energy is striking (see for instance references [7,8]), and already many applications are found today working flawlessly. Renewable energies, however, still need to convince many governments to be the best and only alternative to the still most common energy sources as coal, oil, gas, and nuclear power.

Most of all countries in South America, with high potential for renewable energies, have not yet started to understand this point. Although it is well-known that self-sufficient countries avoid conflicts over resources [6], Chile, for example, depends on other countries to satisfy its need for energy with strong political problems. Its potential for renewable energy, however, is enormous, as in the north, the driest place on Earth, the Atacama desert, is found - one of the most

suitable regions on Earth for solar energy [10].

One of the most promising technologies to produce electricity from solar energy is the use of photovoltaics (PV) for power generation by silicon solar cell panels. Today many scientist are working on the PV field to improve the efficiency of state-of-the-art industrial silicon solar cells. Novel solar cell concepts should fulfil the compromise between high efficiency and low production costs, to make solar energy a competitive source of clean electricity. Thinner silicon solar cells with rear passivation will surely help to achieve this goal [11].

This chapter introduces the motivation of the present work based on the next generation industrial solar cell, with a rear passivation layer and local rear contact formation. By the end of the chapter, the state-of-the-art rear passivated solar cell is introduced, ending with an outline of the thesis.

## **1.2 Motivation: Contact Formation for Rear Passivated Solar Cells**

In advanced solar cell concepts, where the reduction of the silicon material thickness and the increase of cell efficiency necessitates the improvement of the rear surface design, the rear side incorporates a passivation layer that is interrupted by small-area local aluminum contacts. The potential of this cell structure is discussed in several publications [11–16].

The industry shows strong interest in these solar cell concepts with a passivated, locally contacted rear side, due to their higher efficiency on thinner wafers as a key requirement for the next generation of solar cells, in order to decrease the costs per power output. The use of thinner wafers means an important saving potential for silicon in the industry, since more wafers per ingot can be produced [17].

The main results presented in this thesis are based on the rear passivated solar cell concept. New experimental observations on the contact formation at the rear side of this device will be presented.

For this work, screen-printed aluminum pastes and *p*-type crystalline silicon surfaces were tested. The contact between aluminum and silicon is formed locally through the openings of a rear passivation layer (dielectric). The application of these physical observations gave rise to high efficiency rear passivated solar cells in laboratory. Since conventional processes can be used for fabrication, this solar

cell device presents a high potential for industrial application in the nearby future.

Important contributions to rear surface passivation techniques have come up recently. They have been motivated by the improvement of solar cell efficiency in industrial production [18–20]. The dielectrically coated rear surface enables an improvement of the internal light reflection compared to a fully covered aluminum area. Another advantage is the minimization of the rear surface recombination velocity by a reduced Al metallization. As a consequence, the open circuit voltage increases by reducing the recombination at the rear side. Another aspect is that a decrease of metallized area reduces the mechanical bow of the wafer due to the different thermal expansion coefficients of Si and Al-Si alloys [21]. The spectral response in the long wavelength is strongly enhanced for this type of solar cell device, resulting in a gain in short circuit current and therefore, in an increase of solar cell efficiency.

There are still open questions, however, regarding the understanding of the local Al-Si contact formation and its influence on the local back surface field formation for industrial screen printed aluminum pastes. The main experimental work presented in this thesis is based on the local contact formation between aluminum and silicon (see Chapter 6).

Blakers *et al.* [12] were the first to present a high efficiency rear side passivated solar cell. This device, called the passivated emitter and rear cell (PERC) showed an increase of the rear internal reflection up to 97 %. A SiO<sub>2</sub> barrier together with a locally alloyed Al/Si interface formed the rear structure. Although the result was not obtained on industrial large area silicon material, the *p*-type float zone wafer of 4 cm<sup>2</sup> size showed an impressive energy conversion efficiency of 22.8 %. With high quality bulk material an open circuit voltage of 696 mV was achieved. Due to the high rear internal reflectivity, the short circuit current was increased up to 40.3 mA/cm<sup>2</sup>, with a fill factor of 81.4 %.

Figure 1.1 shows a schematic model of the industrial PERC structure (after reference [14]). This solar cell has a passivated *n*<sup>+</sup>-layer (P-diffused emitter) at the front side and a dielectrically passivated *p*-type silicon layer with local contact openings (LCOs) at the rear. The interaction between Al and Si occurs locally, and, as a result, sharply delimited dark lines in the thick aluminum layer appear. Thus, the Al-Si alloy and the *p*<sup>+</sup>-doped Al layer (also known as back surface field, BSF) are formed in the LCOs at the back contact area. Contrary to that, state-of-the-art solar cells present a fully covered Al-BSF layer at the back, which gives the name of Al-BSF solar cells.

The analysis of several solar cell structures with rear passivation (for industrial application) is presented in the last chapter of this thesis (Chapter 7). During the

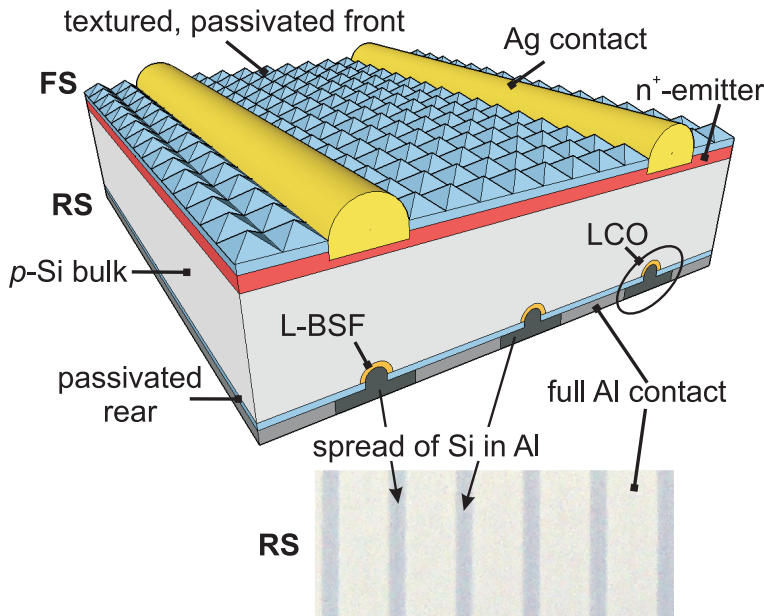


Figure 1.1: Solar cell structure of an industrial rear passivated solar cell (PERC structure), showing the textured and passivated front side emitter, with LCOs at the rear and local back surface field. The spread of Si inside Al is shown in an optical microscope picture, which will be discussed in Chapter 6.

processing of the PERC device, crucial questions appeared in the field of local contact formation between aluminum pastes and silicon surfaces. This thesis was motivated by the following questions (scientific analysis is presented in Chapter 6):

- What is the influence of the contact geometry of the rear side pattern (contact spacing, contact size, and contact opening) on the contact formation and mass transport, and what is the impact on solar cell level?
- What is the explanation for the formation of the observed sharply limited dark lines within the thick aluminum layer, and what is their relevance concerning the Al-Si interaction? How is the distribution of Si in the screen-printed Al?
- Is there an influence of the firing orientation of the cells during firing on the local Al-Si eutectic morphology?
- Why are voids formed after sintering of the contacts instead of Al-Si eutectic layers? Which effect influences the appearance of voids and how can they be minimized?

## 1.3 Outline of the Thesis

Three main parts and six chapters give this work its structure:

### **Part I, Basic Principles and Processing of Silicon Solar Cells**

This part is divided in three main chapters and gives an introduction to the processing and physics of silicon solar cells.

- **Chapter 2** introduces the processing of an industrial state-of-the-art silicon solar cell, showing the typical processes and their development. This classical device is compared with more advanced concepts as the selective emitter solar cell and the rear passivated solar cell. All these devices will be processed, characterized and analyzed in this thesis.
- **Chapter 3** introduces the basic principles and fundamental physical concepts of solar cell devices, as applied throughout this thesis. Basic definitions are clarified, giving an introduction into the loss mechanisms of solar cells that diminish the performance, mainly due to recombination centers and optical and electrical losses within the device.
- **Chapter 4** introduces an application of an innovative selective emitter concept, as a starting point into the understanding of solar cell processing.

### **Part II, Aluminum-Silicon Contact Formation**

This part is divided in two main chapters and contains the main work of this thesis: the understanding and optimization of the local contact formation between aluminum and silicon.

- **Chapter 5** presents a complete overview of the contact formation between screen printed aluminum pastes and silicon surfaces.
- **Chapter 6** presents the main result of this work on the local contact formation between the *p*-type crystalline silicon and screen printed aluminum pastes at the rear side, giving answers based on experimental observations and physical explanations for the questions introduced in the previous section.

### **Part III, Analysis of Industrial Rear Passivated Solar Cell Devices**

After the optimization of the contact formation between aluminum and silicon, high-efficiency solar cells were developed.

- **Chapter 7** shows different device concepts for rear passivated solar cells, analyzing the impact of each processing step. The findings about Al-Si contact formation as presented in previous chapter will be applied in the rear passivated devices presented here. Finally, high efficiency achievements are presented, showing the strong potential of the concepts developed throughout this thesis for industrial application.

In the end, the highlights of the thesis are summarized and the work is concluded with an outlook on further work.

## **Part I**

# **Basic Principles and Processing of Silicon Solar Cells**



# PROCESSING OF AN INDUSTRIAL SOLAR CELL

## Abstract

The process of a solar cell contains wet chemical steps, as cleaning and texturing, and high temperature steps, as phosphorous diffusion and firing of contacts. This chapter explores the preparation of surfaces and the fundamental experimental procedure for creating an industrial silicon solar cell.

## 2.1 Introduction

In this part the principal processing sequence for the development of a state of the art industrial silicon solar cell is discussed, as an introduction for the following work. In table 2.1 three solar cell processes are compared: a state of the art industrial solar cell (Al-BSF solar cell) as discussed in the present chapter, the selective emitter solar cell, studied in chapter 4, and the rear passivated solar cell, main focus of this thesis, which results are presented in chapter 7.

The process sequence of an industrial solar cell starts with the removal of the saw damage from the surface. Secondly, the surface is textured to increase light trapping. Next, the surface is cleaned and a phosphorous diffusion is performed to create the emitter. After removal of the phosphorous silicate glass from the surface and cleaning, the surface is passivated by an antireflection coating. Afterwards, the contacts are screen-printed on the front and rear and sintered. In the end, the edges are isolated and the solar cell is characterized. A few steps differentiate the industrial solar cell from the other two concepts. The rear passivated solar cell is

Table 2.1: Main process steps of the principal solar cells as processed in this thesis: state of the art silicon solar cell (Al-BSF) compared to the selective emitter (see chapter 4) and the rear passivated solar cell (see chapter 7)

Al-BSF solar cell	Selective Emitter	Rear passivated cell
	see chapter 4	see part III
Texture		
		Polishing
Cleaning		
	POCl <sub>3</sub> diffusion 1	
	Selective opening	
POCl <sub>3</sub> diffusion		
		Chemical edge isolation
PSG removal		
FS PECVD-SiN <sub>x</sub> deposition		
		Rear dielectric
Ag, Al metallization and sintering		
Laser edge isolation		

polished and passivated on the back, and the edges are chemically isolated. The selective emitter requires a two phosphorous diffusion process.

## 2.2 Preparation of the Surfaces (Cleaning)

Although in table 2.1 the texture is indicated as the first process, the cleaning is normally performed as the first step to remove the saw damage. A sequence of cleaning steps is shown in table 2.2 and is typically used on the surfaces before deposition or before high temperature processes. The sequence of cleaning typically used in this work to generate clean surfaces is well known and therefore we will concentrate in one important issue: within the cleaning process an important step is the piranha cleaning (also known as IMEC cleaning, after the institute where it was invented [22]). The piranha etching solution contains a mixture of sulfuric acid (H<sub>2</sub>SO<sub>4</sub>) and hydrogen peroxide (H<sub>2</sub>O<sub>2</sub>). It is used before a high-temperature step (as oxidation) to clean organic residues off silicon surfaces. This cleaning concept is a short two step oxidation and cleaning process. Firstly, organic contaminations are removed and a chemical oxide is grown on the surface. Secondly, the oxide layer is etched off to remove particles and metallic surface

Table 2.2: Cleaning process for Si surfaces used in this work before thermal step.

N°	Process	Chemicals involved	Details
1	Rinse	deionized H <sub>2</sub> O	1.5 MΩ
2	HCl	HCl (5 %)	5 min at RT
3	Rinse	deionized H <sub>2</sub> O	1.5 MΩ
4	HF	HF (2 %)	2 min at RT
5	Cascade rinse	deionized H <sub>2</sub> O	1.5 MΩ
6	piranha cleaning	H <sub>2</sub> O <sub>2</sub> :H <sub>2</sub> SO <sub>4</sub> 1:4	80 °C, 10 min
7	Cascade rinse	deionized H <sub>2</sub> O	1.5 MΩ
8	HF	HF (2 %)	2 min at RT
9	Cascade rinse	deionized H <sub>2</sub> O	1.5 MΩ
10	dry	oven with N <sub>2</sub> flux	110 °C, 15 min

contamination.

The oxide grows into the silicon and therefore a thin layer of the semiconductor is removed. After removing this thin oxide layer in the same piranha process, the remaining silicon surface is extremely clean. This cleaning step is extremely important to achieve clean surfaces before surface passivation [22]. Nevertheless, the cleaning process is much faster without the use of piranha etch. Often a reduced cleaning process (referred to as HCl-HF cleaning) is used for removing metal contamination until a hydrophobic surface is achieved (step N° 1-5).

## 2.3 Texturing and Polishing

The first main step in mc-Si solar cell processing is the isotropic acidic etching of the surface by hydrofluoric and nitric acid based solutions (HF-HNO<sub>3</sub>, where HF ~ 10 %, and HNO<sub>3</sub> ~ 45 %). This process removes simultaneously the saw damage on the Si surface and creates partial hemispherical structures as surface texturing [23]. The depth of the etched surface is approx. 4-5 μm on mc-Si material. Texturing is an efficient method to increase the optical absorption by randomizing the incident light through light trapping [24]. The reduction of the reflectivity of incident light increase solar cell efficiency.

Contrary to that, for Cz-Si material, the texturing is anisotropic, performed in alkaline solutions such as potassium hydroxide (KOH) or sodium hydroxide (NaOH) [25] mixed with iso-propyl-alcohol (IPA) which have etching rates depending on the crystallographic orientations. This leads to the formation of pyramidal structures on the silicon surface, because etching stops at the most dense <111> crystallographic plane [26]. The depth of the etched surface is approx. 8-11 μm on Cz-Si material.

Although in the process sequence of a standard industrial silicon solar cell the rear side is not polished, this approach has many applications for high-efficiency rear passivated solar cells. Important insights into its impact on the smoothness of the surface and influence on the bulk lifetime will be given in chapter 7. The polishing of the surface is isotropic and normally found in two chemical forms: the acidic polishing for mc-Si material is normally achieved by HF–HNO<sub>3</sub> concentrated etching solutions, and the alkaline polishing for Cz-Si substrates is performed by high concentrations of KOH or NaOH etching solutions.

## 2.4 POCl<sub>3</sub> Diffusion

The main step in the creation of a solar cell from a *p*-type silicon substrate is the diffusion of *n*-type dopants into the silicon bulk to generate the *p-n* junction. In this thesis *p*-type silicon substrates have been used and the formation of the *n*<sup>+</sup>-type emitter is performed by the diffusion of phosphorous atoms into *p*-Si in a tube furnace at temperatures above 800 °C. The doping profile of the emitter can be characterized by secondary ion mass spectroscopy (SIMS). It has been shown that a standard phosphorous emitter (sheet resistance of 66 Ω/□) presents a doping profile with a peak density of 1.6×10<sup>21</sup> cm<sup>-3</sup>, and a depth of approx. 0.27 μm into the silicon [27].

It is well known that, during the phosphorus oxychloride (POCl<sub>3</sub>) diffusion, a phosphorous silicate glass (PSG) grows on the silicon surface and a phosphorous diffused emitter forms underneath the glass [28] (for more details about the phosphorous diffusion processes in the photovoltaic see references [29, 30]). An application of the POCl<sub>3</sub> diffusion with in-situ thermal oxidation is given in chapter 4.

## 2.5 Antireflection Coating

Silicon is actually opaque within the visible range of the optical spectrum, and can be considered transparent in the near infrared spectra [31]. Because its surface is highly reflective, showing a high index of refraction ( $n_i$ ), antireflection coatings (ARC) are normally used to overcome this effect, reducing the reflection (R) of incident light. An ideal ARC for the front and for the rear surface of a solar cell is achieved when the total reflectivity at the front surface is zero (R = 0) and

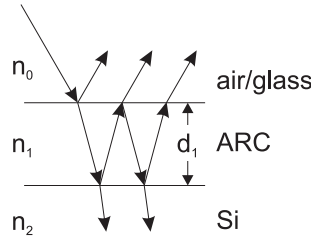


Figure 2.1: Principle of a quarter wavelength antireflection coating: incident light from air, through the ARC and into the Si interface.

at the rear surface is maximum ( $R = 1$ ) [24]\*. Hence, every incident photon is absorbed and generates a new electron-hole pair. The absorbance of the device is increased through dielectrics with index of refraction higher than 1 ( $n_i > 1$ ) [24]. The index of refraction is a function of the wavelength [32]. Nevertheless, for a silicon cell measured under air, the refractive index is normally approximate to  $n_{opt} \approx 3.8$  [33] (see Table 2.3). A work on this topic is found in reference [34]. Following the principle of a quarter wavelength ARC [33] (see Figure 2.1), the minimum for the reflection is found when

$$n_1 d_1 = \frac{\lambda_0}{4} \quad (2.1)$$

and reads (see Figure 2.1):

$$R_{min} = \left( \frac{n_1^2 - n_0 n_2}{n_1^2 + n_0 n_2} \right)^2 \quad (2.2)$$

This relation means that for one dielectric layer the zero reflectance is achieved, when the film thickness is equal to one quarter of the wavelength. Total absorption of light is found at zero reflection, when the square root of the index of silicon is equal to the index of ARC  $n_1 \approx 1.95$  (which approximates to the index of a silicon nitride film as shown in Table 2.3, and normally used in PV). It means that for silicon, the optimal dielectric layer might have an index of refraction of 1.95. Using equation 2.1 the optimal thickness for the ARC in order to have zero reflection at 600 nm (maximum of the solar spectrum) is:

$$d_1 = \frac{\lambda_0}{4n_1} \approx 76.95 \text{ nm} \quad (2.3)$$

\*Specially on mc-Si surfaces, a darker grain boundary implies a lower reflectivity region [26].

†The refractive index strongly depend on the wavelength. These values are normally determined by a wavelength of 632 nm, which represents a red laser diode as implemented in Ellipsometry. This

Table 2.3: Refractive indices of Si, SiN<sub>x</sub>, SiO<sub>2</sub> as used throughout this thesis.

	Surface/layer	Chemical name	Refractive index
$n_0$	Air		1.00
$n_1$	PECVD silicon nitride	SiN <sub>x</sub>	2.05
$n_1$	Thermally grown silicon dioxide	SiO <sub>2</sub>	1.46
$n_2$	Silicon	Si	3.80 <sup>†</sup>

### 2.5.1 Plasma Silicon Nitride Deposition

During the plasma enhanced chemical vapor deposition (PECVD) a reaction between silane (SiH<sub>4</sub>) and ammonia (NH<sub>3</sub>) occurs at high temperatures in a furnace, allowing the deposition of thin silicon nitride films. This method is regularly used in PV as an electrical field effect passivation and ARC. The reaction is given by:  $3 \text{SiH}_4 (\text{g}) + 4 \text{NH}_3 (\text{g}) \rightarrow \text{Si}_3\text{N}_4 (\text{s}) + 12 \text{H}_2 (\text{g})$  [31].

## 2.6 Thermal Oxidation

Thin silicon dioxide (SiO<sub>2</sub>) films, thermally grown into silicon surfaces as dielectric passivation layer, have been in use since the integrated circuits industry appeared in the early 60's [35]. It is used in this thesis to study SiO<sub>2</sub> /SiN<sub>x</sub> stacks for rear surface passivation of solar cells. The thermal formation of SiO<sub>2</sub> is performed in a clean quartz furnace at high temperatures (800 - 1200 °C). The oxide layer is grown in a dry atmosphere by pure oxygen as follows:



The growth of thin SiO<sub>2</sub> dielectric layer consumes only a few nanometers of the silicon surface with a thickness approximated to 45 % of the thickness of the SiO<sub>2</sub> layer grown<sup>‡</sup>. To achieve a good passivation by dielectric layers a highly clean surface is required. The growing rate of the oxide depends on the crystal orientation as shown elsewhere [35].

value is a good approximation in PV, because the minimum reflectivity of an ARC in a solar cell device is optimized for 600 nm.

<sup>‡</sup>*i.e.* in order to achieve 10 nm thermally grown SiO<sub>2</sub>, 4.5 nm of Si surface will be removed during the process.

## 2.7 Screen-printing Metallization and Sintering of Contacts

The metallization of solar cells in the industry is still mostly performed by means of a screen-printing technique. On the illuminated side silver pastes are used to perform the characteristic H-pattern design with three busbars for module assembly and fine lines. However, the continuous increase in the price of silver has shown that other materials, as copper paste, and new printing techniques are required for the future solar cells [36].

The rear surface is fully covered by aluminium pastes, and silver pads are incorporated for module assembly. The contact is formed during firing the samples in a lamp heated conveyor belt furnace. On the front, the glass content in liquid state fires through the ARC to contact the emitter [37]. On the rear, a fully covered Al-Si alloy is formed and the Si interface is highly- $p^+$ -doped by Al atoms, forming the well known back-surface-field (BSF, see part II). Therefore, state of the art solar cells are well-known as Al-BSF solar cells.

## 2.8 Edge Isolation

After the phosphorous diffusion, a  $n^+$ -doped layer fully covers the Si substrate (if no back-to-back process is used [38]). During the metallization, the alloying process between Al and Si overcompensates the shallow P-doped layer on the back (the emitter is few microns deep compared to the 10  $\mu\text{m}$  deep Al-Si eutectic layer). At this point, the front and rear form a short circuit through the edges of the substrate. The electrons in the emitter region can easily move through the emitter at the edges to the back, shunting the solar cell. Two types of edge isolation are normally used: laser edge isolation at the front (see for instance reference [39]) where laser lines that are a few microns deep separate the front side emitter from the rear (laser damage may reduce cell performance); and an inline chemical edge isolation which etches the back emitter layer completely before metallization (no damage of the front side is performed).

## 2.9 Dielectric Ablations

Dielectric layers can be used as barriers against thermal processes, as diffusion or thermal oxidation. Selectivity can be easily achieved by ablation of dielectrics. The ablation of dielectrics is performed in this work by etching pastes.

The pastes used are environmentally friendly and provide excellent screen printing behavior. Some etchants of dielectrics are also addressed in this section.

### 2.9.1 Etching Paste

The etching of the dielectric is performed using the screen-printable isishape SolarEtch<sup>TM</sup> etching pastes from Merck KGaA [40]. Two products are presented:

**The BRS Etching Paste:** Is a fluoride containing paste, designed to etch SiO<sub>2</sub> layers at room temperature. The pink color of the BRS paste makes it easy to differentiate from BES which is black. The etching rate of a thermal SiO<sub>2</sub> layer is typically 3-4 nm/s at room temperature. For the screen printing process, standard stainless steel screens of 250-280 mesh count and 20-25 μm wire diameter were used. The emulsion of the screens has a thickness of about 20-25 μm. The squeegee speed of the screen printing machine is 15 cm/s. For the best etching performance of this paste resulting in a continuously etched line through the dielectric layer, it is necessary to use a continuous process flow. To clean the screens from the paste they are rinsed in water, leaving a low organic and fluoride concentration in the volume of water used.

**The BES Etching Paste:** The BES etching paste is a HF and Chloride free paste, designed to etch SiN<sub>x</sub> or SiO<sub>2</sub> dielectric layers. It contains phosphoric acid, a useful etchant of dielectric films [41]. Almost all of the dielectric layers presented in the publications and throughout this thesis were selectively opened by screen printing this phosphorus containing etching paste. This paste requires higher temperatures than BRS. The activation of the etching properties is done by drying the wafers slowly (4 min.) in a 6 zones infrared conveyor belt furnace at 330 °C. The etching rate of a thermal SiO<sub>2</sub> layer is typically 1.5-2 nm/s, and 3-4 nm/s for PECVD SiN<sub>x</sub>, during the drying. Immediately after the drying step the wafers were placed in carriers and put into an ultrasonic bath for cleaning. The cleaning of the etching paste is completed after a few seconds in an ultrasonic bath with deionized water and 0.2 % potassium hydroxide (KOH), at 40 °C. For textured wafers the opening of dielectrics may be improved by increasing the KOH content in the deionized water in the bath. This paste will be used in the present work.

Some authors applied these etching techniques for selective emitter solar cell concepts, showing differences in the performance between these two commercial pastes (see reference [42]).

### 2.9.2 Some Etchants of Dielectrics

The etching of dielectrics is used in the processing of rear passivated solar cells, when dielectric layers are deposited as barriers against thermal processes. During the processing of solar cells in this thesis, three main etching processes were studied. The etching rate of as-cut Si < 100 > by 22 % NaOH was tested (this process is normally performed for polishing the surface) and the etching rate of SiN<sub>x</sub> by 2 % HF was studied. This is useful when SiN<sub>x</sub> is used as a barrier against a following thermal step, as thermal oxidation or diffusion. Al-si alloys were etched by HCl in order to analyze the shape of the alloy in the silicon material.

**KOH, NaOH Solutions:** In low concentrations with organic additives these alkaline solutions are used for anisotropic etching of silicon (texturing). In high concentrations, the etching process is similar to an isotropic etching (polishing).

**Hydrofluoric Acid (HF):** This acid is used for etching of dielectrics, such as SiO<sub>2</sub>- and SiN<sub>x</sub>-silicon layers.

**Hydrochloric Acid (HCl):** This acid is used for etching thick Al layers and Al-Si eutectics, not removing p<sup>+</sup>-doped Si surfaces.

The etching rate of both layers, SiN<sub>x</sub> etched by HF and Si etched by NaOH, was studied and is shown in Figure 2.2. The etching rate by 2 % HF solution of both layers, SiN<sub>x</sub> directly after deposition and SiN<sub>x</sub> after a thermal process, was measured [Figure 2.2(a)]. The SiN<sub>x</sub> treated by a thermal process is more difficult to remove. The etching rate of SiN<sub>x</sub> by 2 % HF is approx. 2.4 nm/min, and the etching rate of thermally treated SiN<sub>x</sub> (900 °C) by 2 % HF is approx. 0.4 nm/min. Figure 2.2(b) shows the etching rate of bare silicon by 22 % NaOH solution, with an etching rate of 2 nm/min.

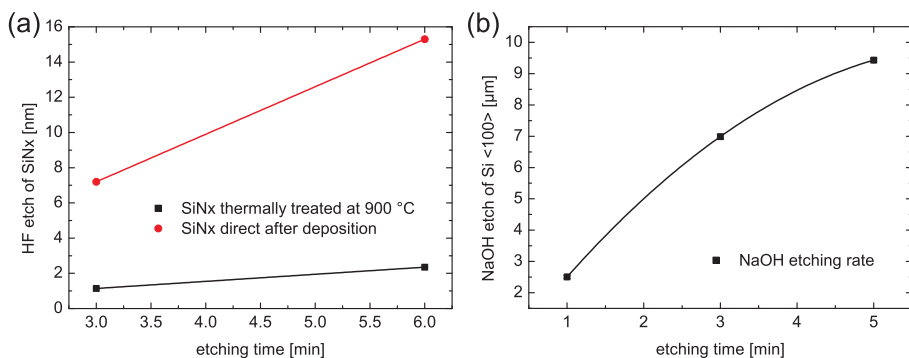


Figure 2.2: (a) Etching rate of SiN<sub>x</sub> by 2 % HF. (b) Etching rate of Si < 100 > by 22 % NaOH.



## BASIC PRINCIPLES OF SOLAR CELLS

### Abstract

The photovoltaic effect was discovered by A. E. Becquerel in 1839 [43]. G. W. Pickard invented the crystal detector in 1906 [44, 45] with strong radio receiving properties, using for the first time the semiconductor properties of silicon\*.

The first  $p$ - $n$  junction silicon light-sensitive electric device was invented by R. S. Ohl [46]. This was the first time that a photovoltaic effect in elementary material was found [44]. Ohl found segregation of impurities in a metallurgical silicon ingot. He found that boron and aluminum created gaps in the crystal structure of silicon, changing the conductivity of the material to  $p$ -type, and phosphorus contributed with excess of electrons, changing the conductivity of the material to  $n$ -type [44].

Today the three impurities found by Ohl are still widely used in the photovoltaics industry of crystalline silicon ( $c$ -Si) solar cells with different approaches: for creating emitters (phosphorus or boron diffusion, or sintering of screen-printing aluminum), for doping the bulk material (phosphorus or boron doping during crystallization), and for creating front surface field (FSF) or back surface fields (BSF).

This chapter explores the fundamental physical concepts of solar cells. The principal characteristics and characterization methods of solar cell devices will be presented and the basic definitions of loss mechanisms in solar cell are introduced.

---

\*Si is one of the most abundant elements on earth.

### 3.1 Characterization of Solar Cells

Industrial solar cells require high efficiency at low cost (high reproducibility, simple processes, good reliability). Nevertheless, there are some fundamental limits to the maximum power conversion efficiency of the solar cell. In this section, typical characterization methods are shown.

#### 3.1.1 *I-V*-Characteristic

##### Solar Cell Efficiency Limit

The solar cell efficiency ( $\eta$ ) is defined as the ratio of maximum output power ( $P_{mp}$ ) to a load to the incident solar power ( $P_{opt}$ ) on the cell (see equation 3.1). The bandgap of silicon is 1.12 eV, and therefore, only incident light with photon energy ( $h\nu$ ) equal or above the bandgap can be used for photogeneration of charge carriers within the solar cell (see section 3.3, light absorption of Si). The excess energy above the bandgap increases the device temperature by thermalization of the excited electrons. Thus, only the bandgap energy can be transferred into electrical energy. The solar cell efficiency is measurable in terrestrial applications at a temperature of 25 °C by considering the energy spectrum, which penetrates the atmosphere, as quantified by the Air Mass, AM1.5. Based on radiative recombination the detailed balance limit of solar cell efficiency has been first published by Shockley and Queisser [47] to be 30 %. Nevertheless, an extended model including Auger recombination, free carrier absorption, and radiative recombination has shown an efficiency limit of 29.8 % [48] under AM1.5, for c-Si solar cells.

$$\eta \equiv \frac{P_{mp}}{P_{light}} = \frac{J_{SC} V_{OC} FF}{P_{light}} \quad (3.1)$$

##### Open-Circuit Voltage Limit

The upper open-circuit voltage ( $V_{OC}$ ) limit achievable in a silicon solar cell device was shown to be 750 mV for an accessible silicon bulk material of 300  $\mu\text{m}$  thickness [49], measured with AM0 (space applications) at 25 °C. This value is much smaller than the band gap of Si ( $E_g = 1.12 \text{ V}$ ), because in heavily excited silicon normally quasi-Fermi levels are located within the bandgap, forming fundamental upper limits for photogenerated carriers which are trapped there until they recombine [49]. The  $V_{OC}$  can be obtained from the simplified first diode model by setting

the current in equation 3.19 to zero ( $I = 0$ ), obtaining:

$$V_{OC} = \frac{kT}{q} \ln \left( 1 + \frac{I_{SC}}{I_{01}} \right) \quad (3.2)$$

$V_{OC}$  strongly depends on the dark-saturation current  $I_0$ , which should be minimal (*i.e.* the recombination should be minimal for an optimal  $V_{OC}$  of the device).

### Fill Factor Limit

The fill factor (FF) characterizes the quality of the solar cell, giving the maximum output power point,  $P_{mp}$ , with the coordinates  $(V_{mp}, J_{mp})$  in the fourth quadrant of the  $I$ - $V$  characteristics of a solar cell under illumination. Generally, FF is given by the following equation:

$$FF \equiv \frac{J_{mp} V_{mp}}{J_{SC} V_{OC}} \cdot 100 \% \quad (3.3)$$

The FF achieves its maximum (FF = 100 %) when  $P_{mp} = J_{SC} * V_{OC}$ . It will be shown in this thesis that good solar cells can achieve 80 % FF. The higher its value, the higher the quality of the solar cell device. The FF, however, depends on many parameters and is therefore only expressed as an approximation in some defined ranges in terms of other cell parameters [50]. Several publications have shown empirical approximations for the FF of solar cells, showing for the ideal case (without losses) that FF is depending only on  $V_{OC}$  [50, 51]. Generally, the FF is mainly affected by series resistance and shunt resistance losses in the cell, and by the second diode (ideality factor 2) of the device.

### 3.1.2 Spectral Response

The solar spectrum on earth is approximated to the AM1.5 standard. The spectrum defines different photon wavelengths, with their respective photon energies, which produce photocurrent in the solar cell device from the absorbed incident light. The response of the solar cell device to the incident light is defined by the **spectral response** (SR). To characterize the spectral response of a solar cell and in order to determine the generated photocurrent, one measures the charge carriers collected in the solar cell device per flux of incident photons, known as the **quantum efficiency** (QE). Two forms of QE can be defined: for externally observed response, known as the external quantum efficiency (EQE), and for internal response, known as the internal quantum efficiency (IQE). In the ideal case, no recombination mechanisms, no absorption losses, and no reflection losses limit the device. In this case, QE is unity [52].

The ratio of generated charge to incident photons as observed externally, is given by:

$$EQE(\lambda) = \frac{I_{ph}/q}{P_{opt}/E_{ph}} = \frac{I_{ph}/q}{\Phi_{in}(\lambda)} \quad (3.4)$$

In equation 3.4, the ratio of the photocurrent  $I_{ph}$  to the incident photon power  $P_{opt}$  is known as the spectral response (SR), or responsivity [52] of the device, where  $I_{ph}$  gives the flow of electrons moving from the valence band to the conduction band and  $P_{opt}$  is the optical power [53]. Thus,  $I_{ph}$  should be maximized, by maximizing the absorption in the bulk<sup>†</sup>.

Representing the spectral response mathematically, one gets:

$$SR(\lambda) = \frac{I_{ph}}{P_{opt}} = \frac{q}{h\nu} EQE(\lambda) = \frac{q\lambda}{hc} EQE(\lambda) \quad (3.5)$$

In equation 3.5,  $q/h\nu = V_g^{-1}$ , with  $V_g$  defined by Shockley [47] as the voltage at which each incident photon with energy greater than the bandgap of Si ( $h\nu \geq E_g$ ), will produce one charge ( $q$ ). The SR is enhanced at specific wavelengths, through different processing steps in the device. For instance, the blue light response of the solar cell is enhanced by lowly doped emitters and high surface passivation qualities (see for instance the selective emitter concept in section 4.1). In the same way, the infrared response is enhanced by better rear passivation qualities and light trapping (see for instance the rear passivated solar cell in chapter 7). At the same time, the ratio of generated charge to incident photons as observed internally, is given by:

$$IQE(\lambda) = \frac{I_{ph}/q}{P_{opt}/E_{ph}[1 - R(\lambda)]} = \frac{EQE(\lambda)}{[1 - R(\lambda)]} \quad (3.6)$$

Thus, the internal quantum efficiency IQE is the ratio between absorbed photons and collected electrons [55]. In equation 3.6 the quantum efficiency considers the total reflectance ( $R$ ) which is the sum of the front reflectance of incident light, and the escape reflectance outside the device [56]<sup>‡</sup>.

The escape reflectance considers the internal reflection at the rear of the device, which is appreciable in the infrared spectral response of the device. Normally, the rear surface reflectivity is ignored in approximate modeling of solar cell devices [57]. Fischer showed that the effective diffusion length,  $L_{eff}$ , can be related to the internal quantum efficiency, IQE, and the absorption length  $\alpha^{-1}$  in

<sup>†</sup>It has to be mentioned that the photoelectric sensitivity is a result of the temperature effect on the distribution of the electrons in different levels [54].

<sup>‡</sup>The reflection is measured in the UV-Vis-NIR spectrometer.

the following simplified expression, for moderately absorbed light [55]:

$$L_{eff} = \alpha^{-1} \left( \frac{1}{IQE} - 1 \right)^{-1} \quad (3.7)$$

This expression for the effective diffusion length is often used as an important parameter to determine the short wavelength current collection and the current injection in the dark [55].

### 3.1.3 Short-Circuit Current Density

The short-circuit current density ( $J_{SC}$ ) depends on the device structure, quality of the bulk material, and operating conditions. Its value is given by the convolution of the external quantum efficiency, EQE, and the number of penetrated photons,  $\Phi_{in}$ , along the light spectrum:

$$J_{SC} = q \int EQE(\lambda) \Phi_{in}(\lambda) d\lambda \quad (3.8)$$

$J_{SC}$  is strongly limited by optical and recombination losses. It will be shown later that the reduction of the reflectivity of bare silicon by deposition of an antireflection coating (ARC) increases the trapping of light in the device and thus enhances  $J_{SC}$ . Also the absorption is enhanced by reducing shadowing losses of metal contacts at the front of the solar cell, as in the case of the interdigitated back contact solar cell (IBC) [58].

As shown by the absorption coefficient of intrinsic silicon, long light wavelengths need a minimum material thickness or a good light trapping at the rear in order to be effectively coupled into the cell and to generate charge carriers in the bulk<sup>§</sup>. These requirements are fulfilled by the dielectrically coated rear surface of thin Si solar cells, as studied throughout this thesis.

Electron-hole pairs generated far away from the  $p$ - $n$ -junction present high probability of recombination at bulk defects or at the surfaces, reducing  $J_{SC}$ . The rear surface passivation quality plays an important role in the electric and optical performance of the solar cell. This thesis shows that the rear dielectric coating improves  $J_{SC}$  due to the higher internal reflectivity of the coating compared to a fully covered Al back surface field (BSF). Also better passivation qualities than the Al-BSF are demonstrated by means of the rear dielectric coating to reduce the surface recombination velocity.

---

<sup>§</sup>A light wavelength of 1000 nm has a penetration depth of 100  $\mu$ m in the bulk material.

### 3.1.4 A few Characterization Tools

#### Scanning Electron Microscopy

In this thesis the Al-Si alloy junction is characterized by scanning electron microscopy (SEM) and energy dispersive X-ray spectrometry (EDS/EDX). The cross-sectional analysis is performed after laser cutting of the samples. High-quality SEM micrographs can be achieved with the respective selection of parameters and no extra cleaning step. The parameters to be used are as follows: acceleration voltage 10 kV, specimen current 780 pA, scanning speed 5.4  $\mu\text{s}/\text{pxl}$ , and electron beam focused to 660 nm in diameter. Counts at the  $\text{SiK}\alpha$  line were taken for 300 s, with a line scan width of 10  $\mu\text{m}$ . Highly doped regions are visible to the eye (*i.e.*  $p^+$ -doped areas by Al), because the emission intensity from doped structures is logarithmically proportional to the active dopant concentration [59]. The EDS/EDX analysis is hence a strong characterizing technique, which turns imaging into a quantitative analysis tool [59].

#### Light Beam Induced Current and Electroluminescence

The light beam induced current (LBIC) is a topographical measurement technique usually applied to detect losses within the solar cell. This method is also called mapping technique, due to the point to point scan across the wafer surface. It combines the high spatial resolution of a probe beam with electrical signals from the recombination of excess electron-hole pairs [60, 61]. This method gives a detailed understanding of parameters that may be responsible for the reduction of the solar cell efficiency. The efficiency of a multicrystalline (mc) silicon solar cell is well known to be limited by defects where strong recombination places are sited for minority carriers, normally localized within dislocations. LBIC makes the areas with low minority carrier lifetime visible. The mapping method is a strong technique, nevertheless one of the large disadvantages is the rather long time taken to cover a large surface mapping<sup>¶</sup>. A laser beam scans along the surface, reading out the current on each measured point. The different light wavelengths of the laser allow to analyze different layers within the solar cell. For instance, at 400 nm the emitter surface is dominating the cell performance, at 800 nm the bulk is characterized; and above 900 nm the rear surface of the device is visible for analysis.

The measurements presented in this work were performed by a Semilab WT-

---

<sup>¶</sup>For example a  $156 \times 156 \text{ cm}^2$  cell with a LBIC resolution of 125  $\mu\text{m}$  needs up to 16 h to be fully inspected by 4 laser wavelengths.

2000 system. The measuring method presents a spot size of 100  $\mu\text{m}$  with four variable light sources. The LBIC method is performed on sintered solar cells with contacts. Also the reflection is measurable for each four light wavelengths, allowing to calculate the IQE response. Bulk and rear recombination properties of the solar cell are indirectly determined as  $L_{eff}$ , which is obtained from the LBIC method. The  $L_{eff}$  and IQE results allow to characterize the performance of the finished solar cell, indicating the quality of the cell process. Through the LBIC method it is also possible to determine the IQE response from the EQE and R data.

The Electroluminescence (EL) analysis is based on an optical phenomenon which makes a semiconductor to emit light by passing a current through the material rather than by the absorption of photons [62]. Its mechanism is the opposite of generation, here the injected carriers recombine within the bulk emitting light. This approach allows to recognize the regions within the solar cell where losses in recombination and series resistance are present. It is a strong tool for the analysis of dislocations within mc-Si material which are visible as dark regions on the EL-picture.

## 3.2 Loss Mechanisms of Solar Cells

The power conversion efficiency of the solar cell is limited by loss mechanisms, predominantly by series resistance losses and recombination mechanisms. Both mechanisms are described in the present section.

### 3.2.1 Series Resistance Losses

The series resistance losses,  $R_S$  [ $\Omega\text{cm}^2$ ] can be dominant for the reduced solar cell performance by limiting the output power of the solar cell device. The total  $R_S$  is given by all parasitic ohmic losses as found throughout the solar device, which increase the resistance of the current transport, as shown in Figure 3.1 [63]. Its value is given by:

$$R_S = \sum_{i=1}^6 R_i \quad (3.9)$$

where  $R_i$  represents each component of resistance.  $R_1$  is the contact resistance between the fully covered Al rear layer and the  $p$ -Si bulk. Due to the high series resistance of the bulk material and the large covered area, its value has a non-measurable influence on the total current-voltage characteristic and is generally

negligible [64].  $R_2$  is given by the doping of the bulk material.  $R_3$ , one of the main contributors to  $R_S$ , is the sheet resistance of the emitter and depends on the emitter profile characteristics (*i.e.* doping concentration, thickness).  $R_4$  is given by the contact resistivity.  $R_5$  and  $R_6$  represent the resistance of the silver finger grid contacts and busbars, and their values depend on many factors as the paste properties (glass and silver composition) and deposition method (firing profile and geometry).

High series resistance mostly affects the FF of the solar cell. The maximum is reached when  $R_S \rightarrow 0$  (ideal case), and decreases with increasing series resistance.  $J_{SC}$  is also affected by  $R_S$ , decreasing its value more than  $8 \text{ mA/cm}^2$  when  $R_S$  increases to values up to  $20 \text{ }\Omega\text{cm}^2$  [65].  $R_S$  values of standard industrial solar cells are in the range of  $0.5\text{-}1 \text{ }\Omega\text{cm}^2$ .

### Shunt Resistance

The shunt resistance losses are caused by short-circuits in solar cell devices. The shunt resistance, also called parallel resistance ( $R_P$ ), is measured in  $\Omega\text{cm}^2$ . The most affected variable is the FF of the solar cell which achieves its maximum when  $R_P \rightarrow \infty$ , and decreases with decreasing shunt resistance. The open-circuit voltage is also affected, reducing its value by more than  $300 \text{ mV}$  with  $R_P$  values as low as  $10 \text{ }\Omega\text{cm}^2$  [65]. Thus, for good solar cell performance,  $R_P$  needs to be maximized (values in the range of  $10^4 \text{ }\Omega\text{cm}^2$  are required).

### Bulk Resistivity

The conductivity,  $\sigma$ , of a semiconductor with electrons and holes as charge carriers, is represented by the sum of the product of the carrier concentrations ( $n$ ,

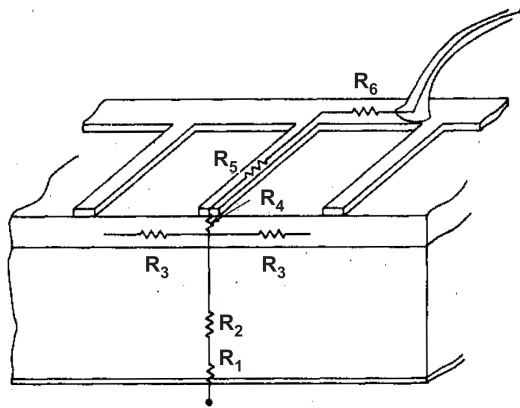


Figure 3.1: Different contributions to total series resistance loss in a solar cell device, after reference [63].

$p$ ) with their mobilities ( $\mu_n, \mu_p$ ), and is given by:

$$\sigma = q(\mu_n n + \mu_p p) = \frac{1}{\rho} \quad (3.10)$$

Its value increases by several orders of magnitude when the doping concentration in the bulk material is increased, and under illumination due to the increase of free net charge carriers [52].  $\rho$  [ $\Omega\text{-cm}$ ] is the resistivity of the material. The mobility of charge carriers is variable and depends on the diffusion coefficient in presence of a concentration gradient of defects [52, 66]<sup>||</sup>, and can therefore also affect the material resistivity.

### Ohmic Contact

Contact losses are supposed to only faintly disturb the device performance. Therefore, in order to transport the photocurrent out of the semiconductor with minimal losses, a negligible metal-semiconductor contact resistance, which shows ohmic behavior, is required [64, 67]. Ohmic contacts obey the fundamental requirements of Ohm's law within a large voltage range [64].

Ohmic contacts are achieved by high doping concentrations of the silicon and, according to the Schottky theory (see reference [68]), by low barrier heights or small barrier widths to the metal. In a solar cell device this is an important topic since two metal-semiconductor junctions are found in direct contact to the cell structure: at the front, crystalline silver particles contact the emitter, and at the rear, an aluminum-silicon (Al-Si) eutectic is found. Therefore the most practical technique in photovoltaics to achieve high performance contacts is to deposit the metal onto a highly doped semiconductor, as already shown by Cabrera *et al.* [69].

Low-resistance ohmic contacts at the rear side of industrial solar cell structures are a result of the interdiffusion between Al and Si, which takes place at the local contact interface [70]. However, the interaction between Al and Si (their interdiffusion), is not homogeneously distributed at the interface over the contact area [71]. This phenomenon will be discussed in more details in chapter 6.

The total contact resistance,  $R_C$ , can be obtained by dividing the contact resistivity value,  $\rho_c$ , by the contact area  $A$ . It has the unit Ohm ( $\Omega$ ) and is given by the following equation [52]:

$$R_C = \frac{\rho_c}{A} \quad (3.11)$$

---

<sup>||</sup>The mobility is proportional to the diffusivity,  $D$ , divided by the thermal voltage,  $kT/q$  (Einstein relationships).

### Contact Resistivity

As defined by Schroder [72], the specific contact resistance,  $\rho_c$ , is a theoretical quantity which refers to the metal-semiconductor interface only. It is defined as the reciprocal of the derivative of current density with respect to voltage (see equation 3.12). It has the unit  $\text{m}\Omega\text{cm}^2$ , and characterizes the contact independent of its area [63]\*\*.

$$\rho_c \equiv \left( \frac{dJ}{dV} \right)_{V=0}^{-1} \quad (3.12)$$

The solution of equation 3.12 is approximated by physical regimes, depending on doping and temperature, known as: thermionic emission (TE) for lowly doped bulk material, thermionic field/emission (TFE) for intermediate range, and tunneling for higher doping concentrations. Due to these effects this parameter is actually not measurable [72].

For solar cells, this parameter is approximately determined by the Transmission Line Model (TLM, see next section). It is important to mention that the TLM method has been widely used for measuring the contact resistance of Ag lines alloyed on homogeneously  $n^+$ -doped emitter layer (sheet resistance of the emitter constant). Thus, there exists no generalization of the TLM method for measuring Al contact, where the sheet resistance is not constant due to the presence of the highly  $p^+$ -doped layer (local BSF) underneath the Al lines. Nevertheless, results will be shown for the contact resistivity by TLM approach of aluminum lines on a dielectric layer and forming an ohmic contact to a  $p$ -type Si polished surface, assuming that the entire contact length contributes to current transfer [63].

For solar cell devices the interpretation of  $\rho_c$  is of strong importance to understand the performance of real contacts. It is very useful when comparing contacts of different sizes, to give information about the quality of the metal-semiconductor contact. Berger [73] and later also Schroder and Meier [63] have given useful definitions and explanations of many methods to determine the contact resistivity. They have shown significant measurement techniques for contact resistivity of Al-Si contacts depending on surface doping concentration. Also a spatial variation of the contact resistivity was presented and explained by taking into account the inhomogeneity of the contacts. A variation of the contact resistivity was found from the middle to the edges of the contact area. This is also valid for the investigation presented in this thesis: it will be shown that the contact resistivity depends on the homogeneity of the Al-Si alloy formation.

---

\*\*The contact resistance is normalized by the area.

### Transmission Line Model

One method to determine the contact resistivity and the sheet resistance of the semiconductor beneath the contact from the geometry of planar contacts, is called the Transmission Line Model (TLM). For deep details about the measuring method, examples and results, see for instance reference [63, 73, 74].

According to Schroder [63], the current transfer from semiconductor to metal takes place on the transfer length,  $L_T$ . It is clear from the equation 3.13 that  $L_T$  decreases with increasing sheet resistance ( $R_{SH}$ ) of the diffused layer, normally the phosphorous emitter. The two extremes are: (a) when  $\rho_c$  is too low, the current transfer will be located near the edge of the metal [63] ( $L_T$  is small); and (b) when  $\rho_c$  is high or  $R_{SH}$  low ( $L_T$  is large, but not larger than the contact width). Nevertheless, it will be shown in this thesis that real contacts present uniformities on the metal-semiconductor interface, where the effective area may vary from the actual area [63].

$$L_T = \sqrt{(\rho_c / R_{SH})} \quad (3.13)$$

### Sheet Resistance

Thin layers as the phosphorus-diffused emitter on the top of the solar cell, are characterized by their sheet resistance  $R_{SH}$  [ $\Omega/\square$ ]. Its value is normally characterized by the four-point-probe method that has been used since the 50's [75]. Generally, the sheet resistance can be obtained by integrating the emitter profile of the phosphorous diffused layer. For a non-uniformly doped layer of thickness  $W$ , its value is given by:

$$R_{SH} = \frac{1}{q \int_x^W \frac{1}{\rho(x)} dx} \quad (3.14)$$

Equation 3.14 shows that the sheet resistance is actually determined by the resistivity profile of the diffused layer, moving along the  $x$  coordinate from the surface (at  $x = 0$ ) into the thin layer, and can be characterized by removing thin layers one by one and measuring the resistivity of the bulk,  $\rho$  [72]. This measuring technique is based on the electrochemical capacitance-voltage (ECV) measurement, which allows the determination of the doping concentration peak close to the surface of the thin doped layer. The higher the concentration  $N_A$  of phosphorus (P) dopant atoms is, the lower will be the sheet resistance,  $R_{SH}$ , of the P-diffused emitter.

### 3.2.2 Recombination in Solar Cells

Generally, the recombination process of charge carriers is defined as the reverse process of their generation. The thermal-equilibrium condition of a semiconductor (in the dark) can be disturbed by illuminating the device, increasing the charge carrier concentration by *generation* of electron-hole pairs [35]. After generation, the carriers tend to return to their original state of equilibrium through the event of *recombination*. Thus, the two mechanisms to disturb the equilibrium-condition are [52]: the recombination process of the electron-hole pairs (undesirable) and the thermal generation through photon illumination (required). Both mechanisms must fulfill the principle of conservation of energy<sup>††</sup>.

In solar cells the recombination leads to an undesirable reduction of solar cell efficiency due to the losses of generated carriers. The generation increases by optimizing the absorption of photons from the incident light on the solar cell device, increasing  $\eta$ . The event of generation is the most important process in a solar cell, for converting the incident sunlight into electrical energy.

In semiconductors there are three fundamental recombination possibilities [35, 76], which are the band-to-band radiative recombination, the band-to-band Auger recombination (non-phononic mechanism) and the recombination through defect levels or traps (phononic mechanism) (see Figure 3.2).

The last two events dominate in Si solar cells.

#### Band-to-band Radiative Recombination

The radiative recombination is the reverse of the absorption and occurs when an electron jump from the conduction band,  $E_C$ , into the valence band,  $E_V$ , and this event is therefore faster in a direct-bandgap ( $E_g$ ) semiconductors than in an indirect one. Direct-bandgap semiconductors (as GaAs) have the minimum of  $E_C$  and the maximum of  $E_V$  at the same wave vector,  $k$  [66]. An electron with the necessary energy to jump from the valence band into the conduction band becomes free to move in the crystal. By the transition of the electron to the conduction band, a hole is created, which is as well free to move in the valence band (generation, see reference [66]). An electron, however, can also lose energy and fall back into the valence band, recombining with a free hole (see reference [66]). The energy by this recombination event is released in the form of a photon. Hence, this is a 3-particle process [35]. Their energy is near to the visible range and therefore this process is exploited in devices such as light-emitting

---

<sup>††</sup>The energy of an electron in transition is conserved by emitting a photon (radiative recombination) or by transferring the energy to another electron or hole, exciting its state to a higher level instead of emitting light (Auger recombination) [35, 52].

diodes (LEDs). Due to the indirect bandgap in most group IV-semiconductors (Si, Ge), the radiative recombination is unlikely to occur and is normally negligible.

### Auger Recombination

The Auger recombination is defined as band-to-band recombination. In the band-to-band Auger process, an electron at  $E_C$  falls back to the  $E_V$  by transferring its original energy to an electron in  $E_C$ , which is excited to a higher level in the Brillouin zone. The separation of the wave vector,  $k$ , in indirect-semiconductors assist the occurrence of an Auger event with minimal activation energy. The Auger mechanism dominates the recombination in heavily doped silicon or when silicon is in high-injection levels [57]. The Auger recombination is the direct recombination between an electron and a hole and, in solar cells, occurs when holes are injected into the heavily doped  $n^+$ -region (emitter) [52].  $\eta$  is affected by the minority carrier lifetime in the heavily doped regions [76]. Good quality bulk materials are predominantly affected by Auger recombination [33, 76]. Furthermore, the quantum efficiency and the emitter saturation current of highly doped emitter layers are affected at low injection conditions [77].

This recombination process is quantified via the Auger coefficients [78].

### Recombination Through Defect Levels, Shockley-Read-Hall

Impurities, incorporated in the bulk material during crystal growth, doping, processing, and so forth, can act as recombination centers located within the bandgap [66]. The resulting Shockley-Read-Hall (SRH) [80, 81] recombination process is the predominant recombination process in Si bulk devices [57]. Electrons within non-pure materials and in transition between bands are affected by the energy

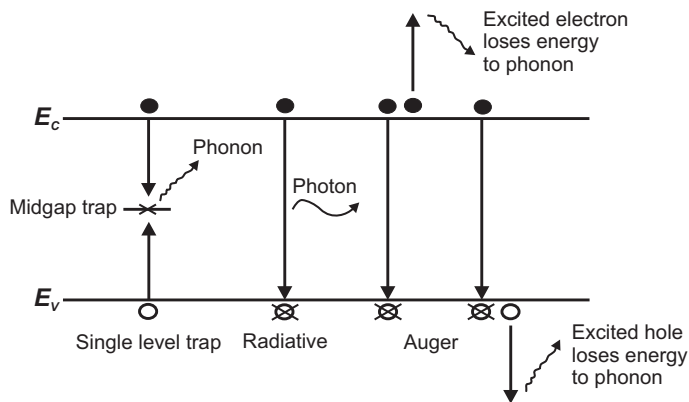


Figure 3.2: Recombination in semiconductors as discussed in the present section (after reference [79]).

states created within the band gap (impurity in the lattice).

### Excess Carrier Lifetime

Lifetime can be understood as the average time between the generation event of a free carrier and its recombination. It depends on many parameters as the temperature, carrier concentration, energy gap, and others. It was defined by Beattie and Landsberg [82] as the ratio of the non-equilibrium number of electron-hole pairs ( $N$ ) to the total recombination rate ( $R$ ). When neglecting the effect of defect traps, the lifetime is obtained by:

$$\tau \equiv \frac{N}{R} \quad (3.15)$$

The total bulk recombination rate is the sum of the individual rates of each recombination event [35]. Thus, the total bulk carrier lifetime is given by:

$$\frac{1}{\tau_b} = \frac{1}{\tau_{radiative}} + \frac{1}{\tau_{Auger}} + \frac{1}{\tau_{defect}} \quad (3.16)$$

As shown by Equation 3.16, the total bulk carrier lifetime is limited via several recombination processes, which occur in the semiconductor at different doping concentrations. The lifetime decreases with increasing dopant concentration: at high doping concentrations ( $N_A > 2 \times 10^{18} \text{ cm}^{-3}$  or  $N_D > 6 \times 10^{18} \text{ cm}^{-3}$ ) lifetime is Auger-limited and decreases quadratically with increasing dopant concentration [78]. In moderately and low doped regions, recombination via defect levels dominates [76], where lifetime is SRH-limited and decreases quadratically with increasing temperature [78].

### Diffusion Length

The mean distance travelled by a charge carrier, immediately after its generation and until annihilation, is given by the square root of the lifetime  $\tau$ , as:

$$L = \sqrt{D\tau} \quad (3.17)$$

In equation 3.17,  $D$  is the diffusivity depending on the temperature, doping concentration, and mobility [83]. Thus, the diffusion length ( $L$ ) is a function of temperature and lifetime. Equation 3.17 is normally used to calculate the diffusion length of charge carriers in the semiconductor bulk. Both the bulk diffusion length and the bulk lifetime are limited by recombination.

When  $L \ll W$ , the dark saturation current,  $I_0$ , which summarizes recombination events in the solar cell, is independent of the rear surface passivation qualities. In the desirable case,  $L \gg W$ , the charge carriers come in contact with

the high- $p^+$ -doped layer at the back of the device, being repelled back into the bulk, reducing the recombination at the rear surface.

### Surface Recombination Velocity

The surface recombination velocity characterizes the surface quality of the device. It depends on the properties of the surface states, on the injection level and on the doping [35]. Rear surface passivation will enhance the spectral response of the solar cell at long wavelengths ( $\lambda$ ) and increase  $J_{SC}$  due to the reduction of the rear surface recombination velocity ( $S_{eff}$ ). Passivating layers as thermal oxide [35] and aluminum oxide  $Al_2O_3$  deposition (created by atomic layer deposition [84]) have shown low surface recombination rates (70 and 80 cm/s, respectively), compared to fully covered Al-BSF (450 cm/s) as recently published by Gatz *et al.* [85].

### 3.3 Light Absorption of the Silicon Material

The photons with an energy equal or above the band gap ( $h\nu > E_g$ ) are absorbed in the Si bulk and generate electron-hole pairs. This process is the inverse radiative recombination event. The photons with an energy lower than the bandgap ( $h\nu < E_g$ ) do not electrically affect the Si material, due to its transparency to their wavelengths.

The absorption coefficient,  $\alpha$  [ $cm^{-1}$ ], measures the distance a wave of light travels into the material [66]. In the case of ion-implanted particles, the absorption coefficient measures the distance a wave of light travels into the material before it is completely absorbed.  $\alpha$  and the absorption depth for Si at RT are determined by  $\lambda$ , as shown in Figure 3.3, and is defined by equation 3.18 (see reference [86]).  $\alpha$  varies with the temperature, therefore here only the equilibrium conditions at RT are considered.  $\alpha$  is related to the extinction coefficient,  $k$ , and  $\lambda$  by the following formula:

$$\alpha = \frac{4\pi k}{\lambda} \quad (3.18)$$

Formula 3.18 represents the strong dependence of  $\alpha$  on  $\lambda$ , as also shown in Figure 3.3. Photons of short  $\lambda$  are captured within a few microns from the surface of impact. Photons with higher  $\lambda$  are absorbed deeper in the cell. For optical properties of the rear side surface, long  $\lambda$  should be taken into account.

As shown in Figure 3.3, above  $\lambda = 1000$  nm the absorption depth for incident photons is approximately  $150 \mu m$ . Thus, at this wavelength, the characterization and understanding of the optical properties of the rear side of the solar cell are possible. The analysis of the spectral response of the rear passivated solar cell

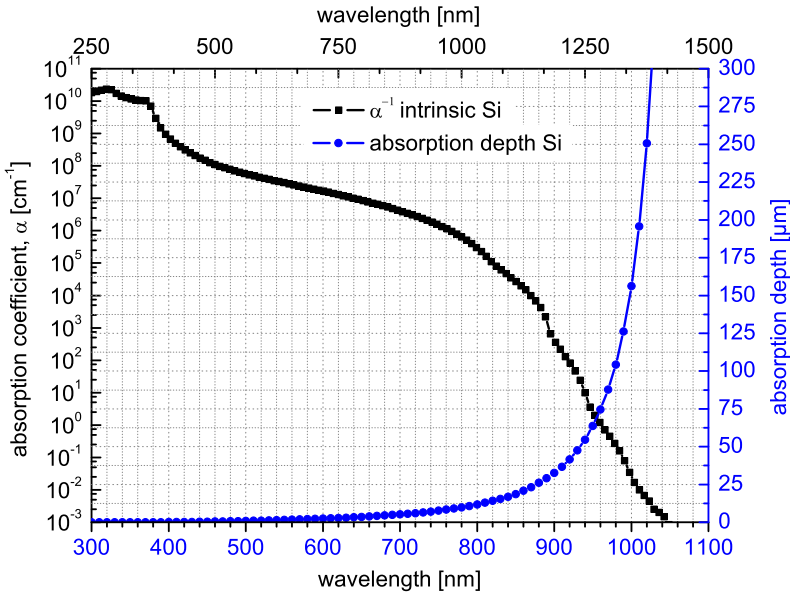


Figure 3.3: Absorption coefficient of intrinsic Si and penetration depth in Si for incident photon wavelengths.

throughout this thesis will be done at long  $\lambda$ .

### 3.4 The Two Diode Model

The two diode model is generally used for characterizing the output current generated by a solar cell. It accounts for parasitic series ( $R_S$ ) and shunt resistance ( $R_P$ ) losses, as well as for recombination losses. It is given by the following expression:

$$I = I_{ph} - I_{01} \left( e^{q \frac{V + IR_S}{kT}} - 1 \right) - I_{02} \left( e^{q \frac{V + IR_S}{2kT}} - 1 \right) - \frac{V + IR_S}{R_P} \quad (3.19)$$

When the device is illuminated, the incident photons generate the photocurrent within the device,  $I_{ph}$  [52].  $I_{01}$  is the dark saturation current due to recombination in the quasi-neutral regions (first ideal diode, ideality factor 1), and  $I_{02}$  is the dark saturation current due to recombination in the space-charge region (second diode, ideality factor 2). The dark saturation currents are of paramount importance in the characterization of losses in solar cells.

The most important losses in solar cells are determined by the first (ideality

factor 1) and second term (ideality factor 2) in the two diode model. The first term influences the reduction of  $V_{OC}$  and the second term the reduction of both, FF and  $V_{OC}$ . In short, the most important losses are: recombination in the depletion region, low front surface and rear surface passivation, low quality of the bulk material, low blue response due to bad emitter qualities, low infrared response due to bad rear side surface qualities (normally determined by the first diode, thus, by  $I_{01}$ ), losses in series resistance, shunts in the  $p-n$  junction, and spiking of metal contacts (normally determined by the second diode, thus, by  $I_{02}$ ).



## SELECTIVE EMITTER SOLAR CELLS

### Abstract

The first solar cell device studied in this thesis is the well known selective emitter concept. Different processes to reduce the front surface recombination velocity, to minimize the contact resistance, and to improve the blue spectral response of the solar cell were recently developed and presented in the literature. For example: single deep diffusion [87, 88], double diffusion process with mask [89], selectively printing of a doping paste, auto doping of the surface or selective application of diffusion barriers [42].

For selective emitters highly  $n^+$ -doped regions are required beneath the Ag fingers at the front side. As the highly phosphorus doped regions deliver a low cell response in the blue region of the spectrum, these areas must be as small as possible and should be located below the Ag metallic contact fingers. Between the fingers a shallow doped emitter is required which can be well passivated to keep the surface recombination as low as possible and to obtain a high  $V_{OC}$  accordingly. A novel process for the formation of a selective emitter is presented by introducing a thermally grown  $\text{SiO}_2$  barrier, immediately grown after the shallow  $\text{POCl}_3$  diffusion in the same process tube. The diffusion process leads to the formation of both a thick PSG and an oxidized emitter underneath. The oxide is used as a barrier for the second diffusion after selective opening of the finger contact areas, by screen printing and drying of a  $\text{SiO}_2$  etching paste.

## 4.1 The Selective Emitter Concept

An innovative process for the formation of a selective emitter is presented, by using an advanced phosphorus glass as a barrier layer against a subsequent second  $\text{POCl}_3$  diffusion. The advanced barrier glass was achieved by the formation of a standard phosphorus glass treated with additional thermal oxidation immediately after deposition in the same process tube. The resistant layer is used as a barrier for the second diffusion after selective opening of the finger contact areas by screen printing of a  $\text{SiO}_2$  etching paste. The process was applied for multicrystalline Elkem solar grade silicon (SoG-Si) wafers (ESS) as well as for references from standard electronic-grade silicon (EG-Si) feedstock. The achieved cell parameters were compared with cell results from a homogeneous emitter process. The efficiency decreases due to the relatively high shadowing loss of the selective emitter solar cells and material limitations. Nevertheless, the  $V_{OC}$  was increased by up to 9 mV, and the short wavelength spectral response was increased slightly with this selective emitter. The aim of this work was to combine the  $\text{SiO}_2$  barrier with the shallow  $\text{POCl}_3$  diffusion in one process step and the optimization of the screen printing process for selective emitter solar cells.

## 4.2 Experimental Part

The experiments were carried out on solar grade silicon feedstock provided by Elkem Solar\*. Crystallization and wafering of the  $p$ -type boron doped multicrystalline wafers, with an area of  $156 \times 156 \text{ mm}^2$ , a thickness of  $200 \mu\text{m}$  and a resistivity of about  $1 \Omega\text{cm}$  was done by Q-Cells†.

For the selective emitter the following process sequence was applied (as shown in the flow diagram in Figure 4.1). First of all, small holes ( $\varnothing 80\text{-}100 \mu\text{m}$ ) were drilled by laser at two different edges of the wafer, to enable the optical alignment of the screen printing cameras based on these two fiducial marks. This method uses artificial vision to find the fiducial points on the wafer, without the need of imprecise alignment on the substrate edges. The laser holes were drilled before the isotropic texturing to avoid any laser damage on the wafer surface.

Isotropic texturing of the multicrystalline wafers was carried out by  $\text{HF-HNO}_3$  acid solution‡ to remove the laser damage and saw damage on the surface of the

---

\*<http://www.elkem.no>

†<http://www.q-cells.com/>

‡*i.e.* Rena approach.

as-cut wafers, and to minimize the reflection of the incident light on the front side (to enhance light trapping).

The main focus of this work is the formation of a  $90\text{-}100\ \Omega/\square$  shallow emitter by  $\text{POCl}_3$  diffusion with a successive in situ thermal oxidation, to achieve a barrier for the following second phosphorus diffusion. The in situ thermal oxidation is achieved by increasing the oxygen flux during the first diffusion without changing the temperature profile of the diffusion recipe. Before the second phosphorus diffusion, the oxide layer was selectively opened with the front grid design by screen printing the BES etching paste (see section 2.9.1). For this process, fine etching lines were screen printed to selectively open the glass layer. As the emitter should only be contacted on the heavily doped area to achieve a good ohmic contact [90], exact alignment was necessary for each printing step, opening and metallization. The screen alignment process is the most important step in successfully making selective emitter solar cells. To achieve a fit with a tolerance fewer than  $10\text{-}20\ \mu\text{m}$ , the screen printer needs to be precisely calibrated.

The second phosphorus diffusion resulted in an emitter sheet resistivity of

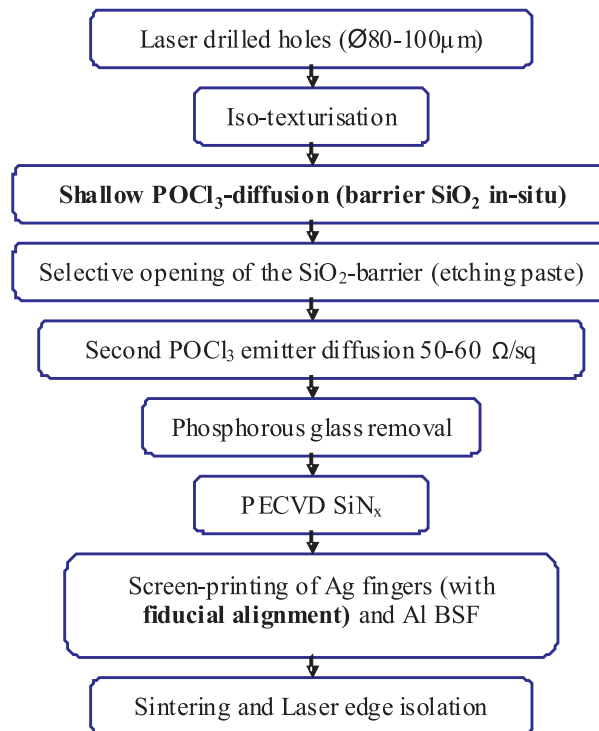


Figure 4.1: Flow diagram sequence of the selective emitter process, with an in situ  $\text{SiO}_2$  barrier growth after the first shallow  $\text{POCl}_3$  diffusion.

60-65  $\Omega/\square$  in the openings (below the Ag contact fingers), and still 90-100  $\Omega/\square$  between the fingers, below the passivated area<sup>§</sup>. Thus, the in-situ created oxide layer acts well as a barrier for the second diffusion. Afterwards, the PSG was removed by HF-dip to enable the passivation of the solar cell. The passivation is carried out by the deposition of a PECVD  $\text{SiN}_x$  layer on the front side (this coating aims to be also an antireflection layer for the incident light).

The metallic contacts were made by a screen printing process adjusted with the help of laser drilled holes as fiducial marks on the edges of the wafer. On the front the same grid was used for the etching paste, as for the Ag fingers. On the rear the contact was formed by a full area of screen printed aluminum to form the BSF layer. Before the sintering of the contacts the inks were dried. The contacts were sintered by an infrared furnace. Later on, the front and the rear side were isolated by laser grooving, obtaining a high shunt resistance. The solar cells were characterized by  $I$ - $V$  measurement.

## 4.3 Screen Printing Approach: Etching of Dielectric Barriers

### 4.3.1 Fiducial Alignment

For the optical alignment it was found that fiducial marks (e.g. as a via made by laser drilling) lead to a more accurate alignment between the screen and the substrate than the alignment at the edges of the wafer.

These fiducial marks enabled an accurate optical detection by the screen printer cameras due to the high contrast between the substrate and the back light coming through the via. For the fiducial alignment two points were required at the edges of the wafer (illustrated in Figure 4.2). For the Baccini screen printer used in this experiments point 1 was on the upper center part of the wafer with coordinates in mm  $(x, y) = (0, 78)$  and point 2 was on the lower right edge of the wafer with coordinates in mm  $(x, y) = (78, -78)$ .

### 4.3.2 Etching Paste and Alignment Approach

To open the oxide layer a front grid of 150  $\mu\text{m}$  fine lines was screen printed by using the BES etching paste of Merck. After 1 to 2 min cleaning time some wafers still showed problems with the removal of the etching paste because of the

---

<sup>§</sup>It has been shown elsewhere that a lightly doped passivated emitter ensures good collection properties and low emitter dark saturation currents [91]

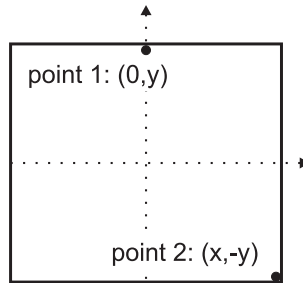


Figure 4.2: Two points were required to achieve the optical fiducial alignment for the screen printer. The points were  $80\ \mu\text{m}$  in diameter laser drilled via for the optical alignment.

surface texture (as shown in Figure 4.3). To verify this effect, a parallel experiment was performed on non-textured Cz-Si wafers resulting in an etching time of only few seconds.

To solve the problem on textured samples mentioned above the cleaning time was increased and the drying temperature was optimized, until the etching paste could be completely removed. Figure 4.3 shows two optical microscope pictures of the local removal of the  $\text{SiO}_2$  barrier layer achieved on a textured mc-Si surface, and the precise result of the alignment between the etched regions and the Ag grids. The measured line width after etching is about  $230\ \mu\text{m}$  for the textured surface. The alignment achieved is precise and reproducible for a screen printing process of selective emitter solar cells.

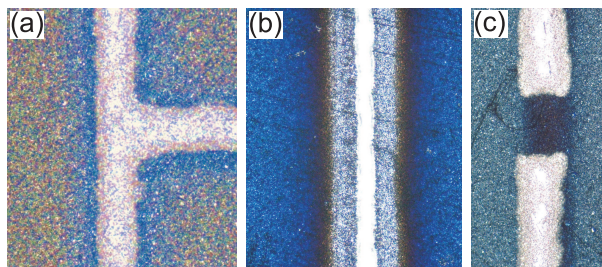


Figure 4.3: (a) Optical micrograph showing the precise dielectric opening and alignment, achieved by optical fiducial alignment of the screen printer. The fine etched line was  $50\ \mu\text{m}$  bigger in width on each side side than the screen ( $130\ \mu\text{m}$ ). (b) Broader etching line as a test to show the precise fiducial alignment. (c) Partly removed etching paste after several seconds in the ultrasonic bath. The removal had to be optimized due to the isotropic textured surface condition.

Table 4.1:  $I$ - $V$  measurement results of the homogeneous and the selective emitter for the ESS and reference material.

<b>ESS 117</b>	$J_{SC}$ [mA/cm <sup>2</sup> ] avg. / best	$V_{OC}$ [mV] avg. / best	FF [%] avg. / best	$\eta$ [%] avg. / best
homog. emitter	32.4 / 32.5	614.9 / 616.0	77.6 / 78.7	15.4 / 15.7
selec. emitter	32.5 / 32.5	623.5 / 623.7	77.5 / 77.6	15.7 / 15.7
<b>Reference</b>				
homog. emitter	32.9 / 33.0	604.6 / 605.8	77.3 / 77.7	15.4 / 15.5
selec. emitter	33.0 / 33.1	609.1 / 612.2	76.3 / 76.3	15.3 / 15.5

## 4.4 Solar Cell Results

### 4.4.1 $I$ - $V$ Characterization

The results of the  $I$ - $V$  measurement are shown in Table 4.1. The selective (selec.) emitter is compared to the homogeneous (homog.) emitter on the Elkem Solar Silicon (ESS) and to reference wafers.

It has been shown in previous work [92], that the ESS material is stable against high temperature processing. As shown in the  $I$ - $V$  results, the ESS wafers read efficiencies of  $\eta=15,7$  % for both processes, the homogeneous and the selective emitter. The reference efficiencies were lower for both emitters. The  $V_{OC}$  is clearly enhanced (as shown in Figure 4.4(b)) by about 9 mV (615  $\rightarrow$  624 mV) for ESS and about 5 mV (604  $\rightarrow$  609 mV) for the reference material due to the selective emitter. Due to a higher spectral response, the  $J_{SC}$  was expected to be higher with selective emitters than for Al-BSF solar cells. However, expectations were not matched, due to a higher number of Ag fingers and the respective high shadowing losses.

### 4.4.2 Spectral Response Characterization

The external quantum efficiency (EQE) measurements of the selective emitter solar cells and the homogeneous emitter cells were compared, as shown in Figure 4.4(a). An improvement of the blue response for both selective emitter solar cells compared to the reference Al-BSF solar cell was shown. The best result was achieved on the ESS material.

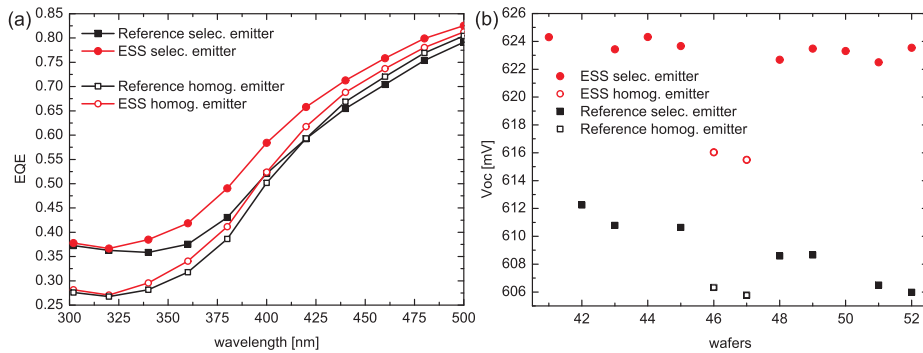


Figure 4.4: (a) EQE of the selective and the homogeneous emitter solar cells for the ESS and reference materials. (b) Improvement in  $V_{OC}$  for both solar cell groups and comparison for both materials.

## 4.5 Conclusions and Discussion

An innovative selective emitter process was investigated with the use of a modified phosphorus glass, which acts as a barrier against the second phosphorus diffusion. It was shown that the shallow  $\text{POCl}_3$  diffusion combined with the in situ  $\text{SiO}_2$  barrier against the subsequent  $\text{POCl}_3$  diffusion works. The cell process involves two different phosphorus diffusions, however, there is no need for an additional process step to create a diffusion barrier layer.

A reliable and reproducible optical alignment process between substrate and screen was achieved, by using two fiducial points. The selective opening of the phosphorus glass by etching paste worked perfectly. Previous investigations have confirmed that Elkem Solar Silicon material is stable against high temperature processes such as thermal oxidation [92]. Although the efficiency decreases due to the relatively high shadowing loss, the  $V_{OC}$  was increased by 9 mV in average for the ESS cells on SoG-Si and about 5 mV for the reference cells on EG-Si.

The spectral response is slightly enhanced in the blue wavelength range for the selective emitter cells as compared to the homogeneous emitter cells. Further investigations are required, in order to optimize the selectivity of the solar cell emitter.



## **Part II**

# **Aluminum-Silicon Contact Formation**



## CONTACT FORMATION, STATE OF THE ART

### Abstract

The main results presented in this thesis deal with the local contact formation between Al metal pastes and Si semiconductor materials. This chapter gives an overview of the contact formation models between Al and Si for standard and rear passivated Si solar cells. In the end, the important applications of an Al layer in photovoltaics must be clarified.

### 5.1 The High-Low Junction as a Back Surface Field

Aluminum layers on the back of Si solar cells have been in use since the early 70's. The back contact was achieved without the need of the phosphorus back layer removal and a the incorporation of Al produced thin electric field (high-low junction), highly increasing the open circuit voltages. This electric field was named the back surface field (BSF, already introduced in this thesis) by Mandelkorn *et al.* [93]. Actually, this electric field effect at the back of solar cells was first treated by the double layer model of Wolf [94] in his study about the drift fields in photovoltaics solar energy converter cells. Nevertheless, Wolf's theory ignored the influence of the BSF on the increased  $V_{OC}$ . The BSF electric properties enhance the majority carrier density of the  $p$ -type Si bulk as shown in Figure 5.1, where on the top a schematic model explains the influence of the BSF effect on the charge carriers. In the middle, the schematic energy band diagram of  $n^+ - p - p^+$  (Al-BSF)

junction solar cell is shown (schematic after references [52, 95]). At the bottom the collection probability of the solar cell with and without BSF is presented (see also the work of del Alamo *et al.*, reference [96]).

As shown at the top of Figure 5.1, the rear side of the Al-BSF cell consists of a heavily doped surface ( $p^+$ ), between the semiconductor and the rear metal contact. The BSF (with a thickness  $W_{BSF}$ ) injects holes at the end of the  $p$ -bulk, increasing their density at the back, reducing the effective surface recombination velocity,  $S_{eff}$ . Due to the potential energy  $q\psi_p$ , the minority carriers (electrons) are driven back to the front, increasing their density in the more lightly doped region: the bulk. This approach gives characteristics of a cell made from lower resistivity Si [98]. Thus, the effective bulk concentration is enhanced. At the same time, the field effect present in the  $n^+ - p$  junction injects electrons at the front junction. Both fields, at the back surface and at the front junction, are barriers for the carriers, holes coming to the front and electrons moving to the back, respectively. Therefore, these electric fields reduce the recombination rate at the

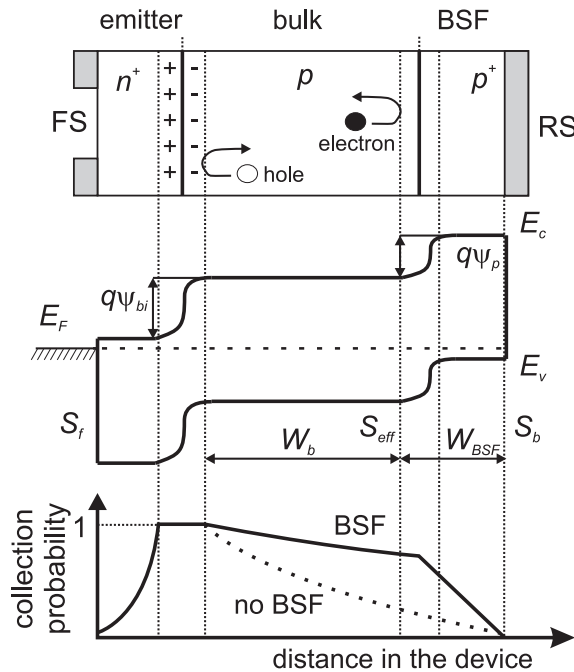


Figure 5.1: Top: model of the Al-BSF cell taken from reference [97] which explains the influence of the BSF effect on the charge carriers. Middle: schematic energy band diagram of  $n^+ - p - p^+$  (Al-BSF) junction solar cell, first presented by Mandelkorn *et al.* [93].  $S_f$ ,  $S_b$  and  $S_{eff}$  represent the front, the rear and the effective surface recombination velocity, respectively.  $W_{BSF}$  and  $W_b$  represent the thickness of the BSF and bulk, respectively. Bottom: collection probability of the solar cell with and without BSF.

surfaces.

This process has been shown many times to increase the  $V_{OC}$  of a  $p$ -type Si solar cell under illumination [99], due to the increase in majority carrier concentration at the front of the bulk [97]. The solar cell gains in  $V_{OC}$  and also in  $J_{SC}$  due to the improvement of the spectral response at low photon energies, the minimization of the diode recombination current, and the extra electric field at the back (BSF).

Mandelkorn [98] also showed a critical thickness for the bulk,  $W_b$ . An optimal distance exists from the front junction to the thin electric field region at the back, in order to use the wished influence of the BSF on the carrier lifetime. An interesting concept was also presented, showing that the beneficial properties of the BSF start to decrease and vanishes the cell qualities ( $V_{OC}$  decreases), if the minority carrier diffusion length,  $L_B$ , is reduced to values fewer than the 40 % of the cell thickness,  $W$ . It has been experimentally shown, however, that the material thickness of extremely good BSF solar cells hardly influences the  $V_{OC}$  [100] (see the next section for the demonstration of these results by simulation). Hence, there is a  $V_{OC}$  limit for Al-BSF solar cells, where the fully covered electric field at the rear no longer improves the efficiency, limited by the thickness of the cell.

## 5.2 Effect of the BSF on $V_{OC}$

To further understand the effect of BSF on the solar cell performance, one dimensional numerical simulations have been performed using the PC1D software performed by Basore (see reference [101]). In order to understand the effect of a high-low junction at the rear of the solar cell, the  $V_{OC}$  has been calculated for the Al-BSF solar cell structure ( $n^+ - p - p^+$ ) and compared to the junction structure ( $n^+ - p$ ) for several bulk impurity concentrations and cell thicknesses.

For the simulations, the front surface recombination velocity,  $S_f$ , is chosen to be  $1 \times 10^5$  cm/s and the rear surface recombination velocity,  $S_b$ , is chosen to be  $1 \times 10^7$  cm/s, for both devices  $n^+ - p$  and  $n^+ - p - p^+$  structure, which are typical values for metal covered c-Si surfaces [95] (see Fig. 5.1). The doping concentration at the front side (FS) emitter and at the rear side (RS) BSF are usually fitted by the well known complementary error function (erfc) and Gaussian function, both profiles are extremely important in diffusion theory [102]. The doping concentration and junction depth are chosen to be at the FS:  $N_D = 2 \times 10^{20}$  cm $^{-3}$ ,  $x_j = 0.39$   $\mu$ m and at the RS:  $N_A = 1 \times 10^{19}$  cm $^{-3}$ ,  $x_j = 6.8$   $\mu$ m, respectively.

$S_{eff}$  is strongly influenced by the thickness of the BSF,  $W_{BSF}$ , as already shown

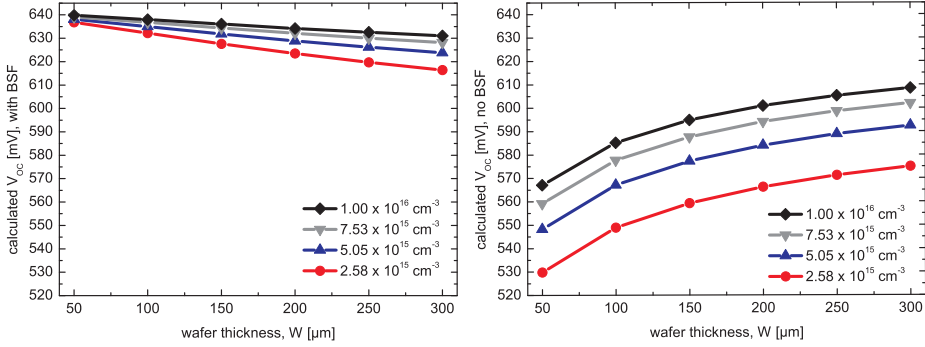


Figure 5.2: PC1D numerical simulations of the BSF effect and thickness influence on  $V_{OC}$ , for several bulk doping concentrations. For a good BSF solar cell  $V_{OC}$  slightly depends on the wafer thickness. The huge difference in  $V_{OC}$  between the  $n^+p$  and  $n^+p-p^+$  solar cells present for low doped materials strongly decreases with the wafer thickness.

by Lölgen [95]. For a standard  $n^+p-p^+$  structure,  $W_{BSF}$  is approximately  $5\ \mu\text{m}$  deep (at standard firing conditions and using industrial Al pastes), reducing the  $S_{eff}$  to approximately  $300\ \text{cm/s}$ .

Figure 5.2 summarizes the results of the simulations. The simulation was performed under AM1.5 illumination and at  $25^\circ\text{C}$ . The results for  $V_{OC}$  are comparable with the Al-BSF solar cell results found in literature [103–105, 107, 108]. As already shown elsewhere [111], the  $V_{OC}$  of a good BSF solar cell slightly depends on the wafer thickness, and decreases with the thickness for lightly doped base materials. The positive effect of the BSF shows a limit, where the  $V_{OC}$  reaches a maximum for Al-BSF solar cell structures of  $640\ \text{mV}$ . When the maximum  $V_{OC}$  is achieved the thickness of a solar cell can be ignored [112].  $\Delta V_{OC}$  (with BSF minus without BSF) decreases with increasing base thickness. The improvement of the  $V_{OC}$  by the  $p-p^+$  junction at the rear of the cell (taken from reference [111]) is given by equation 5.1.

$$\Delta V_{OC} = V_{OC}(n^+pp^+) - V_{OC}(n^+p) \simeq \frac{kT}{q} \ln \left[ \frac{D_n}{N_A W} \int_{W-x_{jb}}^W \frac{N_A}{D_n} dx \right] \quad (5.1)$$

### 5.3 Gettering Properties of Al

Alloying the thick Al layer after the phosphorus diffusion has an important application: the  $n^+$ -phosphorus doped rear surface gets positively doped due to the overcompensation of phosphorus by Al during the alloying process. Also the beneficial effects of the gettering of impurities at the back of the solar cell by firing

Al has been shown elsewhere [108, 109].

## 5.4 Fundamental Mechanisms of Al-Si Contact Formation

The alloy formation between the Al metal and the Si semiconductor is achieved by an interdiffusion between Si and Al atoms at the interface (contact area). The most important issue in the formation of the alloy is the recrystallization from the Al-Si melt of a highly  $p^+$ -doped region, growing epitaxially into the Si bulk.

The thermodynamic behavior that occurs at the Al-Si interface at equilibrium, is described by the phase diagram as illustrated in Figure 5.3. Many authors until now (see references [21, 110]) have explained the contact formation between screen-printed Al pastes and Si based on the phase diagram which applies only for conditions close to equilibrium during the alloying process. This state is difficult to achieve during the fast temperature ramp-up and cooling in industrial processing of solar cells. As an introduction into this topic, I will suppose that the thermodynamic conditions of equilibrium are fulfilled during the whole alloying process between Al and Si, and that it can be described by the simple binary phase diagram, as shown in Figure 5.3 (after Murray and McAlister, see reference [113]).

The borders of different states of matter are separated by specific lines. The triple point where three different phases coexist at equilibrium is called the eutectic point\*. The different lines found in the phase diagram are the liquidus line, showing the temperature limit above which the Al-Si system is stable in the liquid state, and the solidus line below which the Al-Si system is stable in its solid state.  $\alpha$  and  $\beta$  represent the solid solubility of Si into Al and Al into Si, respectively [113]. Thus, the composition of the eutectic formation is described within a range of alloying temperatures determined by the solid and liquid state of matter. Therefore, an analysis of the solidification is accessible. Figure 5.3 shows also the enlargement of important regions within the Al-Si alloying process (after reference [113], see also references [114, 115]): Si-rich solidus ( $\beta$ -Si, top right), Al-rich solidus and solvus ( $\alpha$ -Al, bottom left), and Al-liquidus (L+ $\alpha$ -Al, bottom right).

Two regions are found in the phase diagram. Firstly, Si contents lower than 1.65 %, where the solubility of Si in Al achieves its maximum at the eutectic temperature (577 °C) and decreases with the temperature [114]. In this alloy Si precipitates in the  $\alpha$ -Al solid solution [114]. Secondly, Si contents higher than 1.65 %, where the two-phase alloys solidify at the eutectic temperature, showing a lamellar structure (eutectic alloy,  $c(\text{Si}) = 12.6 \%$  [114]). For hypereutectic

---

\*From the Greek "to melt well".

concentrations of Si in the Al-Si melt ( $c(\text{Si}) > 12.6\%$  [114]), Al presents a solid solubility in Si decreasing with the temperature. During epitaxial growth of Si, a  $p^+$ -doped region is formed, due to the concentration of Al atoms in the Al-Si melt and the solid solubility of Al in Si during recrystallization. For hypoeutectic concentrations ( $c(\text{Si}): 1.65\text{-}12.60\%$  [114]) the solubility of Al in Si is negligible, thus we do not expect to find a  $p^+$ -doped region or BSF.

Figure 5.4 shows the contact formation models between Al and Si for: (a), a rear passivated solar cells, where the contact formation takes place in the narrow dielectric windows, where the Al-Si alloy is formed (the contact area is much smaller than the area of the Al layer); and (b), a  $p$ -type standard solar cell, where Al is fully covering the Si surface (the contact area is the same than the area of the Al layer).

In the following paragraphs the rear contact formation for both types of solar cells is described. The alloying is performed (after drying the paste) by firing the wafers in a lamp heated conveyor belt furnace. The firing parameters are

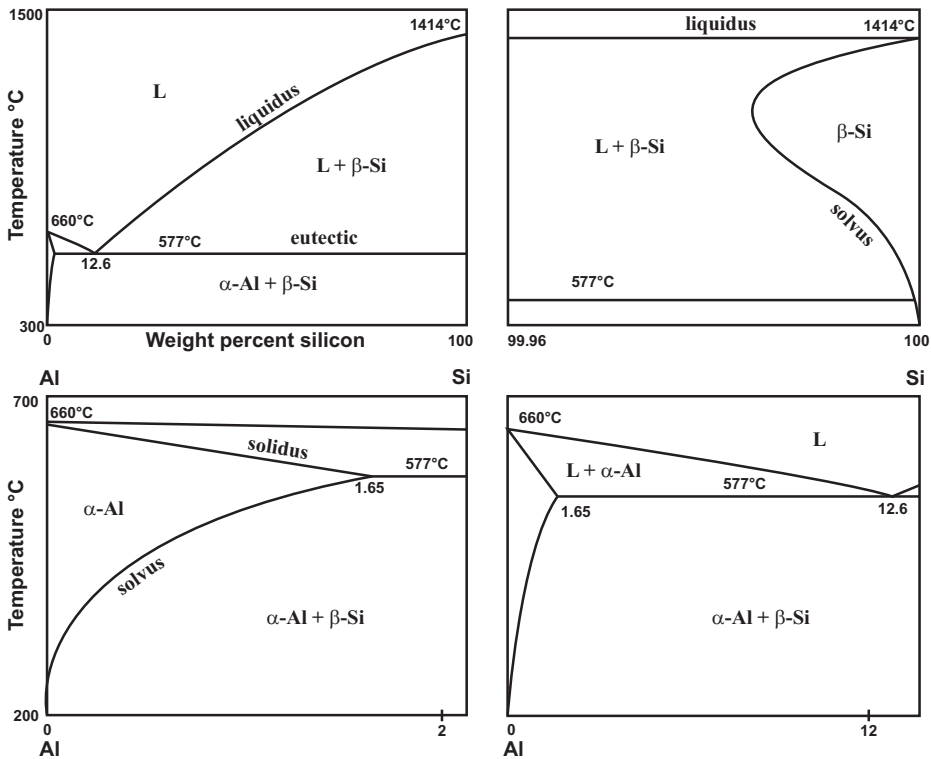


Figure 5.3: Top left: Al-Si phase diagram. Top right: Si-rich solidus ( $\beta$ -Si). Bottom left: Al-rich solidus and solvus ( $\alpha$ -Al). Bottom right: Al-liquidus ( $L + \alpha$ -Al). After reference [113]. See also [114].

set well above the melting temperature of Al, 660 °C [113]. The schematic presented in Figure 5.4 (from 1 to 5) and the phase diagram presented (assuming thermodynamic equilibrium) in Figure 5.3, the Al-Si interaction can be understood as follows:

1. During heating, the solid solubility of Si into Al starts at approx. 300 °C and increases, reaching its maximum at the eutectic temperature ( $T_{eut} = 577$  °C).
2. The solid Al particles change to liquid state above the melting point of Al ( $T_{melt} = 660.3$  °C) and, due to its high melting point, Si ( $T_{melt} = 1414$  °C) is dissolved by Al during the alloying process and an interdiffusion is present at the interface. Thus, an Al-Si melt at the interface forms which starts to penetrate into the Si bulk. Two important issues must be mentioned here: due to the oxide layer forming around Al grains/particulates [ $Al_2O_3$ , see Figure 5.4(c)] the paste matrix keeps its form during the whole sintering [21, 116], and the Al-Si melt starts to appear locally in the Si surface (showed by [21, 116], and within this thesis).
3. By increasing the heating temperature further, the composition of the melt can be determined depending on the temperature, following the liquidus line in the phase diagram. In photovoltaics peak temperatures up to 850 °C are used for sintering the contacts in the device. At this peak temperature and at equilibrium, the concentration of Si in the Al-Si melt is about 30 % and Al is found in liquid state.

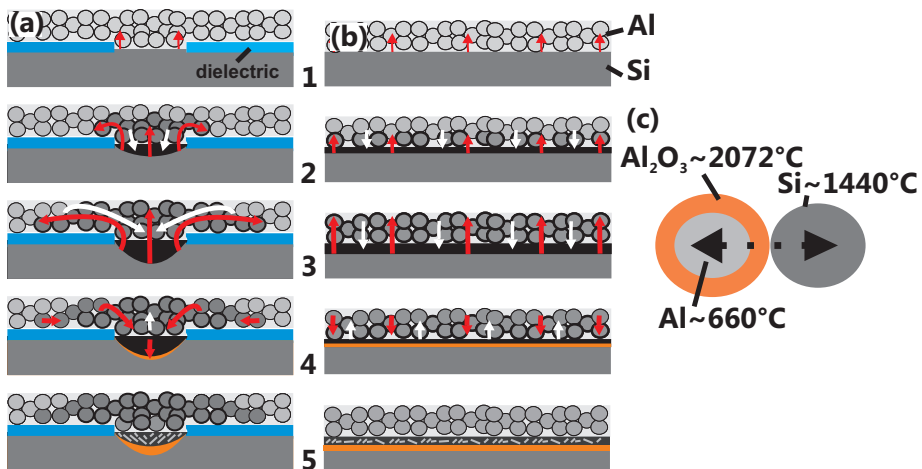


Figure 5.4: Model of contact formation between Al and Si for: (a) Rear passivated solar cell, where the interaction between Al and Si is found through dielectric openings and the contact area is much smaller than the area of the Al layer. (b) Standard fully covered Al-BSF solar cell, where the contact area is the same than the area of the Al layer; (c) Schematic of the interaction between Al and Si, through an Al oxide ( $Al_2O_3$ ) shell which covers the Al paste.

The main difference between the two contact formation models, as presented in Figure 5.4(a) and (b), is as follows: if the contact area is much smaller than the area of the Al layer [case (a)], the liquid Al volume near to the interface is saturated faster by Si than the liquid Al lying on the dielectric layer (away from the interface). Thus, the diffusion of Si into Al at this temperatures occurs laterally from the interface into the Al along the wide and unsaturated paste amount.

4. The solidification process between the metal and the semiconductor can be understood when following the liquidus solidus phase boundary line during cooling. The concentration of Si in the Al-Si melt decreases as the firing temperature decreases, following the liquidus line in the phase diagram. This means that the concentration of Si is rejected from the Al-Si melt to grow epitaxially at the interface Si(S)/Al-Si(L), where S and L stand for solid and liquid, respectively. At the same time solid solubility of Al in Si is present, doping the immediately adjacent solid Si surface, and forming the  $p^+$ -doped region (BSF). Thus, the BSF is formed by both, epitaxially recrystallization of Si from the Al-Si melt, which is highly doped by Al atoms, and by incorporation of Al atoms in the Si lattice. In the contact formation case (a), the BSF is formed locally underneath the alloy, limited by the dielectric opening. Another important issue is that Si is able to diffuse from the Al-Si melt at the interface back into the Si bulk, in contrast to the dissolved Si in the Al matrix away from the contact area, that is practically unable to diffuse back the distance to the interface and remains as precipitates in the Al layer [117]. Kircher [70] found a small reduction of the peak concentration of Si in Al near to the contact area, and he explained this as Si diffusing back from the Al layer and regrowing on the Si surface. This phenomenon has been also found in this thesis (see section 6.4).

5. Below the eutectic temperature the whole liquid solidifies and only solid solubility of the elements is present (see phase diagram). The alloy structure depends on the temperature and is formed by different layers with their respective concentrations.

Figure 5.5 shows the SEM analysis of the alloying junction between a fully covered Al thick layer and the Si bulk, as already presented in Figure 5.4. For case (a) the contact area between Al and Si is limited by the etched windows in the dielectric layer. For case (b) the contact area is the same as the area of the Al layer. The different layers (measured by SEM, EDS/EDX) formed after the sintering and alloying of Al on  $p$ -type Si are: the thick Al layer in porous state, formed by Al spherical particles, Si, Al oxide ( $Al_2O_3$ ), and other lower concentrated species; the Al-Si alloy formation (formed by an eutectic layer Al-12.6 wt. %Si [114] and a lamellar structure formed by Al-rich solid); and the BSF (Si-rich solid).

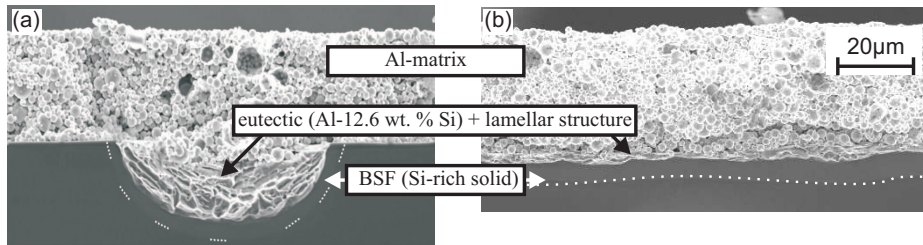


Figure 5.5: SEM micrographs of the Al-Si alloying junction. The three layers formed after solidification are the Al matrix, the eutectic alloy and lamellar structures (Al-rich solid) and the BSF (Si-rich solid). (a) The contact area is limited by etched windows in the dielectric, as on PERC solar cells. (b) The contact area is the same than the Al paste, as on standard Al-BSF solar cells.

The fraction of Si as recrystallized can be related to the temperature during cooling. Due to the small percentage of Al in the solid phase, the formation of the BSF can be understood from the low solid solubility of Al in Si as presented by the solidus line (phase boundary line) as shown by the phase diagram.

After recrystallization a SEM analysis of the cross-sectional microstructure gives information about the alloying process and the thermodynamic process that occurred at the Al-Si interface<sup>†</sup>.

For SEM analysis HCl (HCl:H<sub>2</sub>O 1:1 [118]) was used to remove the Al-matrix and the Al-Si eutectic layer, due to the fact that HCl only dissolves Al and Al-rich layers. The etching stops at the Si-rich layer of the BSF.

## 5.5 Al-Si Lamellas

A lamellar structure is found on the Si surface due to the alloy formation between Al and Si (see for instance reference [55]). Figure 5.6 shows the surface below the Al matrix after removing the sintered Al paste on the Si surface mechanically. During recrystallization of Al-Si melt characteristic lamellar structures are formed in the interface. Thus, Figure 5.6 shows that the contact formation between Al to Si indeed occurred. Below the lamellar structure a high  $p^+$ -doped region is found (BSF). Due to a too fast cooling (*i.e.* not having a thermodynamic equilibrium step, as presented by the phase diagram), the recrystallization of Al and Si can be inhomogeneous, because the alloying process starts locally on the surface [116].

<sup>†</sup>The history is written in the microstructure', Prof. Donald Sadoway, Introduction to Solid State Chemistry, MIT, USA.

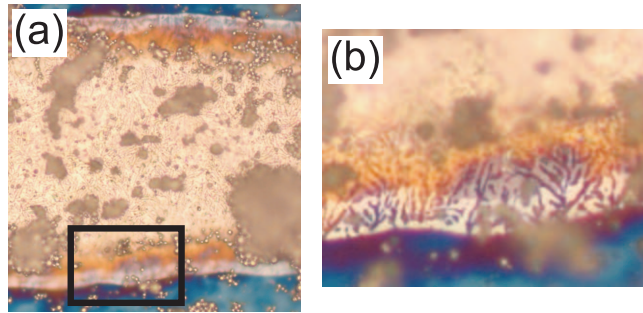


Figure 5.6: The lamellar structure is found after mechanical removal of the Al matrix. (a) Removed Al finger alloyed on SiN<sub>x</sub> layer. (b) Part marked by the rectangle on (a), showing the Al-Si lamellar structure.

## 5.6 Screen Printing and Drying of Aluminum Lines

An amount of Al paste of 7 to 8 mg/cm<sup>2</sup> is normally deposited fully covering the rear of standard solar cells. At the beginning of this work, the adhesion of Al fingers was analyzed for screen printed Al pastes on Si polished surfaces. It was found that the Al paste printed in form of thin lines is susceptible to peeling off from the Si surface after normal drying and firing conditions. Therefore, an optimization of drying and sintering temperatures was performed.

Figure 5.7 shows the adhesion problem of fine Al lines, (a), and the optimal adhesion after the performed drying parameters optimization, (b). After drying the sample in a four zones paternoster (vertically stacked) furnace, at a standard drying profile of 130/150/180/200 °C and a delay time of 10 s<sup>‡</sup>, the Al paste losses amount to 1.6 mg/cm<sup>2</sup>. This loss of weight represents the content of solvents within the paste.

The adhesion after firing was improved by keeping the firing profile of the conveyor belt furnace constant and drying the wafers at different drying profiles. This experiment showed that, for the standard Al paste printed as thin fingers, the drying profile has an essential influence on the remaining amount of solvents within the Al matrix. It has been shown, that lower drying temperatures and shorter delay time improved the adhesion of fingers after firing. This is due to the small amount of Al paste below the heat lamps in the drying furnace. On samples with small amount of Al mass, as screen printed Al fingers, non-optimal drying

<sup>‡</sup>The delay time of the drying furnace differs from the complete drying time of the samples inside the furnace, and corresponds to the time that one pallet stops for the load or unload of wafers until it moves to the next position. The furnace contains 60 pallets. The minimum delay time is about 7 s for one pallet to move to the next position. With a drying time of 10 s, the total time that one wafer is dried in the furnace is represented by  $60 * (7 + 10) \text{ s} = 17 \text{ min}$ .

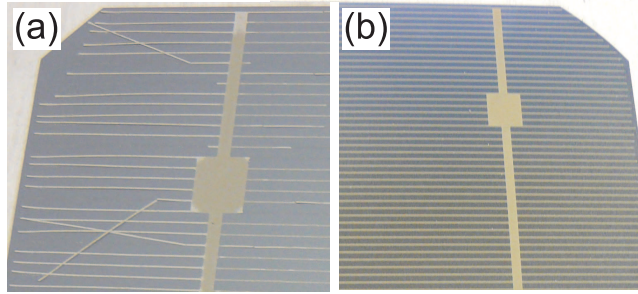


Figure 5.7: (a) Polished Cz-Si wafer showing peeling off of the Al fingers. (b) Same material dried under different conditions showing optimal adhesion after firing.

parameters, as drying temperatures too high and delay time too short, will speed up drying of the paste, leaving a hard coating on the surface of the Al finger, and therefore keeping the solvents in the paste.

It is the author's opinion that, during the drying and firing of the Al fingers then the gases produced due to the evaporation of the solvents trapped below this hard coating of glass, increases the probability of peeling off during firing.

The observations presented here may be also dependent on the paste amount and surface roughness. Firing too slowly leads to a phenomenon known as blistering in the Al matrix. Another phenomenon related to cooling too slow or to high temperatures is the undesired bowing of thin wafers due to the different thermal expansion coefficient between Al and Si, and the influence of temperature on the diffusion of Si in Al-Si melt. This topic will be discussed in the following chapters.



## ALUMINUM-SILICON CONTACT FORMATION THROUGH NARROW DIELECTRIC OPENINGS

### Abstract

The study of the local contact formation between the *p*-type Si bulk and screen printed Al pastes motivated the presented work. Although the contact formation by screen printing is the most frequently used technique in a solar cell line production today, there is still room for investigation regarding effective formation of local contacts between Al and Si. Because the solar cell structure studied in this thesis presents a laterally structured, electronically passivated rear side, the interaction between metal and semiconductor occurs locally through openings in the rear side passivation layer (see chapter 1). In the following chapter, further insight into the contact formation and alloying between Al and Si is given. It is found that the geometry of the rear side pattern of rear passivated solar cells can influence not only series resistance losses within the solar cell, but also the process of contact formation itself. SEM and EDS/EDX analysis of the Al-Si alloy geometry is performed, leading to new insight into the understanding of its influence on contact formation. The impact of the Si diffusion in Al on the contact formation is investigated, which strongly depends on the firing temperature, but less on the contact size (the spread of Si in the Al matrix was optically measured). Inhomogeneous eutectic formations were found for wider contact areas due to the lateral diffusion of Si in Al. It is found, that an increase in the contact spacing enhances the formation of voids instead of an Al-Si eutectic layer. An explanation

is given for the void formations found in the Al-Si alloying junctions, based on the Kirkendall effect, and on the distribution of Si in the Al matrix. In this work, two types of voids were defined: firstly, voids formed during the heating (without back-surface-field), and secondly, voids formed during the cooling (with back-surface-field). The influence of gravity on the microstructure of Al-Si alloy is studied, showing crucial trends for partially avoid the formation of voids. The analysis presented in this chapter is applicable to industrial production of rear passivated solar cells and Al-Si alloying processes.

## 6.1 Introduction

The optimization of the local contacts between screen printed Al pastes and Si is crucial for the performance of solar cells and still requires deeper understanding of the interaction between metal and semiconductor. Indeed, a compromise between the contact area and contact spacing is an essential issue when reducing series resistance losses [119–121]. Also an inadequate heat treatment may cause high series resistance losses, due to inadequate pinhole contacting [122]. Furthermore, the local formation of a high-quality  $p^+$ -doped layer (local BSF) to improve the cell performance [123–125], is still a challenge.

A high quality local BSF has to be homogeneously formed in the pre-defined contact area, with a recrystallized layer depth of usually 4-5  $\mu\text{m}$ , in order to minimize the surface recombination velocity [95]. Parameters as an optimal sintering temperature [126], optimal contact geometry, oxidation of the Si surfaces, homogeneity of the metal layer [85], and Si precipitates in the Al film grain boundary [116] are responsible for a well formed local BSF.

As shown by Beaucarne *et al.* [127], the formation of localized contacts from screen printed Al pastes largely depends on the contact geometry. It has been demonstrated, that up to 60  $\mu\text{m}$  deep pyramidally shaped spikes of Al-Si alloy form below point like openings of 30  $\mu\text{m}$  diameter. The dissolution of Si into Al has been found preferentially along the  $\langle 100 \rangle$  plane [128]. Recently, interesting work has been published about local Al point and line contacts on the rear side passivation of solar cells. The contact formation has been studied for applications on laser firing of rear contacts [11, 121, 129]. The contact spacing has also an influence on the increase of the solar cell efficiency [130]. Differences in surface concentration were found, due to Al inclusions beneath the Si surface of islands and line networks, remaining at the surface even after removal of the Al layer in HCl [131].

This chapter addresses several insights into a deeper understanding of local contact formation during sintering of screen printed Al pastes with  $p$ -type Si substrates, for solar cell application. It is divided into four sections. Firstly, section 6.3 studies the geometry of the Al-Si alloy formation and analyzes the impact of both Al amount and contact width on contact formation and series resistance losses. Secondly, section 6.4 provides a deeper understanding on the contact formation based on the diffusion of Si in the Al matrix and the formation of voids is analyzed. Afterwards, section 6.5 shows the influence of the contact pattern on the local BSF and void formation. Section 6.6 addresses the effect of gravity on the microstructure of Al-Si alloys. And finally, in section 6.7, two types of voids are defined and crucial trends are given in order to avoid the formation of voids instead of an eutectic layer. The structure of the rear passivated solar cell has been introduced in chapter 1.

## 6.2 Preparation of the Surfaces

For the analysis of the Al-Si interaction the Si surface is polished before screen printing and alloying the Al paste with the semiconductor, to diminish the influence of the textured surface (saw damage and texturing of the surface is removed). The process continues with the HCl-HF cleaning of the surface, removing the metal impurities until a hydrophobic surface is achieved. For the study on the local chemical interaction between Al and Si, the contact area must be controlled. Since the Al paste used does not fire through a dielectric layer, the samples are fully covered with a dielectric insulation layer deposited by the PECVD method.

The contact area is limited by the selective openings in this layer. The local contact openings (LCOs) are achieved by screen printing the BES etching paste (more details about the etching process of dielectric layers are found in section 2.9.1). Hence, the alloying of the Al paste to the Si bulk is prevented by the presence of the dielectric barrier everywhere except at the LCOs.

Afterwards, the surface is covered with a screen printed Al layer\*. The alloy is formed after drying and sintering the samples following a standard firing furnace profile, varying in special cases the peak firing temperature.

---

\*Some experiments were performed using thin Al lines and others using fully covered thick Al layers.

### 6.3 Study 1: Local Al-Si Alloy Formation, Contact Resistance and Mass Transport

#### Abstract

The microstructure of the rear contact formation for  $p$ -type Si industrial rear passivated solar cells is analyzed. The Al-Si alloy formation under local contacts and its impact on the contact resistivity is analyzed. It is found that the contact resistivity of fine screen printed Al lines alloyed on narrow  $p$ -type Si areas (lines) decreases by reducing the contact area, while the contact resistance remains constant. At the solar cell level, the reduction of the contact resistivity decreases the FF losses. SEM and EDS/EDX analysis of the Al-Si alloy formation is performed, in order to understand its influence on the contact resistivity.

#### 6.3.1 Experimental Design

The contact of the screen printed Al lines to the substrate is achieved via fine etching lines through the rear passivation layer (dielectric barrier) covering about 9 % of the rear surface (see Figure 6.1). The width of the contact opening and Al line are varied independently for contact optimization. The geometry of the opening lines is limited to less than 200  $\mu\text{m}$  width, otherwise the solar cell will suffer from too much losses (less dielectric passivated area and more metallized area). On the other hand, dielectric openings of typically fewer than 50  $\mu\text{m}$  are hard to realize using commonly used laser or screen printing technology. On these local contact openings, Al lines with variable widths are screen printed in order to analyze the impact of the contact geometry on the Al-Si alloy formation

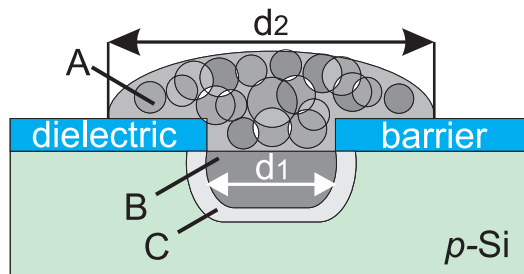


Figure 6.1: Cross sectional model of the alloyed junction structure of screen printed Al lines on dielectric openings, not to scale.  $d_1$ : dielectric opening width (width of LCO).  $d_2$ : Al line width. Note that  $d_2 \gg d_1$ . The layers that define the alloying junction are: A: Al matrix, B: Al-Si alloy, C: local BSF.

and the contact resistance. This analysis should lead to the optimal Al line width (optimal amount of Al) and optimal contact size (dielectric openings) for the best rear passivated  $p$ -type solar cell performance.

Figure 6.1 presents the cross sectional schematic model of the alloyed junction between Al lines and Si in local contact openings.  $p$ -type polished Cz-Si and mc-Si wafers with a size of 156x156 mm<sup>2</sup> and resistivity of 5 and 1.5  $\Omega$  cm, respectively, are selected for this study. The fully covering screen printed Al layer, normally found at the rear of standard solar cell devices, is replaced by screen printed Al lines, in order to understand the impact of the applied Al paste amount on the formation of the Al-Si alloy, and therefore on the contact resistivity.

In Figure 6.1,  $d_1$  represents the width of the LCO, where Al and Si are in direct contact, and  $d_2$  represents the width of the screen printed Al line. The real values for the LCO widths,  $d_1$ , measured by optical microscopy analysis, are 30 to 45  $\mu$ m broader due to the spreading of the etching paste during the drying. The Al lines are deposited exactly centered on the dielectric barrier openings by a screen printing process based on optical alignment at the edges of the wafer.

For each width of the contact opening, different Al line widths are printed. The Al lines are wider than the dielectric opening widths ( $d_2 \gg d_1$ ); thus, the width of the overlapped Al material on each side of the dielectric openings  $[(d_2 - d_1)/2]$  is bigger than the thickness of the Al layer itself. After firing the samples are cut by laser and analyzed in cross-section by SEM, EDS/EDX.

The following experiments aim to find the minimum contact size and screen printed Al line width, in order to achieve good contact formation (homogeneously formed Al-Si alloys and therefore homogeneous local BSF) and a reduced absolute contact resistance. For reasons of simplicity, the thickness of the Al matrix and the sintering time are kept constant. Different sintering temperatures, however, are tested.

### 6.3.2 Impact of Al amount on Contact Formation

The Cz-Si material is used in this part.  $d_1$  (dielectric opening width) was chosen to be 100  $\mu$ m and  $d_2$  (Al finger width) was varied from 200 to 900  $\mu$ m and screen printed on  $d_1$ . For  $d_1 = 200$   $\mu$ m the same is performed with screen printed Al line widths from 300 to 900  $\mu$ m. Figure 6.2(a) presents the TLM measurement results for the contact resistance ( $R_C$ ) and line resistance ( $L_R$ ). It is important to mention that the TLM method has been widely used for measuring the contact resistance of Ag lines alloyed on homogeneously  $n^+$ -doped emitter layers (constant sheet resistance of the emitter). Thus, there is no generalization of the TLM method

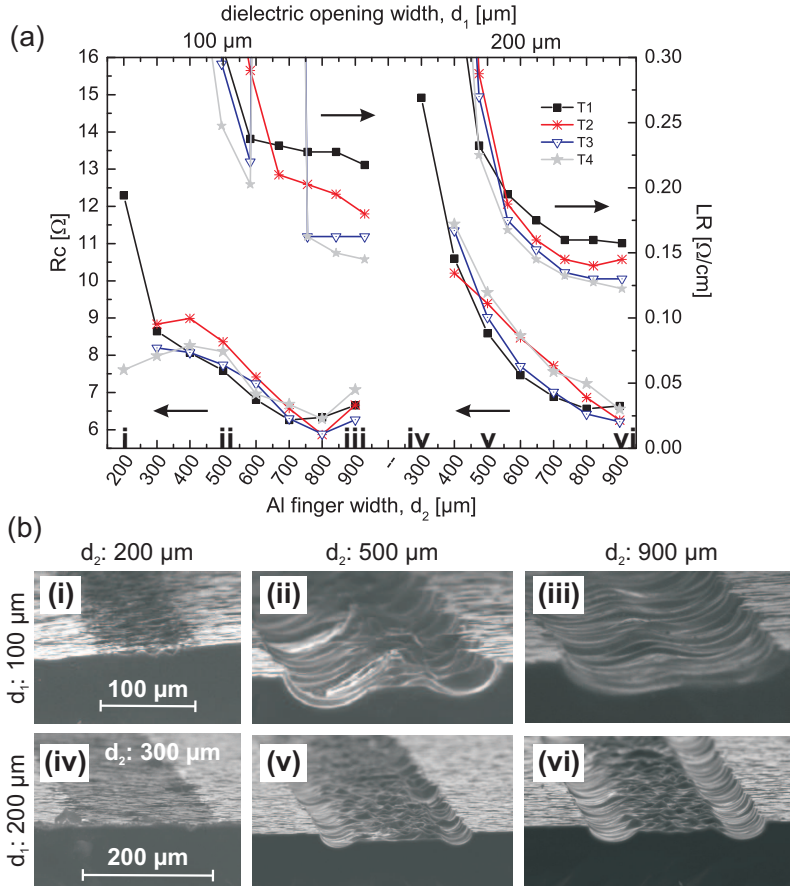


Figure 6.2: (a) TLM result of the contact and line resistance for different Al line widths alloyed on two dielectric openings. Y-axis left: total contact resistance  $R_c$ , decreasing for increased Al line width,  $d_2$ . Y-axis right: line resistance  $L_R$ , decreasing for increased Al line width. X-axis top: dielectric opening,  $d_1$ . X-axis bottom: Al line widths,  $d_2$ . (b) SEM cross sectional micrographs of the contact shape (after HCl etching of the Al matrix and Al-Si eutectic layer) of six samples measured in Figure 6.2 (a). Three Al line widths,  $d_2$ , were analyzed for each contact size,  $d_1$ .

for measuring Al contacts, where the sheet resistance is not constant due to the presence of the highly  $p^+$ -doped layer (local BSF) underneath the Al lines.

Many configurations are shown in order to analyze the impact of the contact geometry on the contact resistance losses. On the left y-axis, the total contact resistance  $R_c$  is plotted, decreasing for increased Al line width,  $d_2$ . On the right y-axis, the line resistance  $L_R$  is shown, decreasing also with  $d_2$ . On the top x-axis, the width of the LCOs is shown ( $d_1 = 100$  and  $200 \mu\text{m}$ ). And finally, on the bottom x-axis, the Al line widths,  $d_2$ , are shown for each contact opening width. The same

experiment is repeated for four different peak firing temperatures, where T2 is the peak firing temperature recommended by the paste developer ( $T_1 < T_2 < T_3 < T_4$ ).

The results suggest a strong dependence of the contact and line resistance on the Al line width, as well as a small dependence on the peak firing temperature and on the opening widths. Similar results were found on mc-Si and will be discussed later. From the theory we expected that  $R_C$  should be linearly dependent on the contact area,  $d_1$ , but independent on the Al amount,  $d_2$  (supposing very low and constant resistivity of Al [63]). Our measurements, however, are in contradiction to the expected results. To analyze this difference SEM analysis on cross-sectional Al-Si micrographs are performed. One optimum can already be found for an Al line width  $d_2 = 800 \mu\text{m}$ , where  $R_C$  reaches its minimum at  $6 \Omega$  and  $L_R$  reaches its minimum at  $0.15 \Omega/\text{cm}$ .

Figure 6.2(b) shows the cross sectional SEM analysis of the Al-Si contact interface, for a choice of samples from Figure 6.2(a). After etching the Al matrix and the Al-Si eutectic layer by the HCl etching method, the shape of the contact interface became visible. Six configurations are shown, from (i) to (vi): For  $d_1 = 100 \mu\text{m}$  the shape of the alloy is shown for Al lines of (i) 200, (ii) 500, and (iii)  $900 \mu\text{m}$  width. For  $d_1 = 200 \mu\text{m}$  barrier opening, the shape of the alloy is shown for Al lines of (iv) 300, (v) 500, and (vi)  $900 \mu\text{m}$  width. From the SEM micrographs is evident that the penetration of the alloy into the Si material is strongly increased by providing a larger amount of Al, showing the strong influence of the overlapping of Al on each side of the opening on the contact formation. Remarkable is the case (vi) ( $d_1 = 200 \mu\text{m}$ ), where a strong planar surface (plateau) is present between the contact opening edges. Case (i) and (iv) in Fig. 6.2 (overlap of Al on each side of the interface:  $50 \mu\text{m}$ ) show no alloy formation and no local BSF, but rather a few local alloy spikes. This shows that the amount of Al, which is found locally in some points on the Si surface, is extremely important for contact formation. Actually Kircher [70] suggested that the diffusion of Si into Al starts locally at some favourable weak spots and diffuses further into the Al, by reducing the driving force for diffusion to occur at other places.

From the experimental point of view, there is a minimum for the Al line width,  $d_2$ , required to obtain a strongly formed Al-Si alloy (and local BSF). As shown in Figure 6.2(b), on  $d_1 = 100 \mu\text{m}$ ,  $500 \mu\text{m}$  Al line width is required, in order to have a better contact formation (homogeneously formed alloy and deeper BSF). Thus, the first conclusion is that the Al amount limits the interdiffusion between Al and Si. For small Al line widths ( $d_2 < = 500 \mu\text{m}$ ) an appreciable increase of the contact resistance is visible due to the low amount of Al overlap, and therefore, non-optimal Al-Si contact formation.

The measured total contact resistance,  $R_C$ , is influenced by the contact size and geometry of the Al-Si alloying junction:  $R_C$  varies with the Al line width,  $d_2$ , but is rather constant for different  $d_1$  values. We expect that  $R_C$  should be constant when  $d_1 = 100 \mu\text{m}$  and  $d_2$  is larger than  $700 \mu\text{m}$ .

In the following section, the minimal possible contact opening width for contact formation will be studied.

### 6.3.3 Impact of Contact Width on Alloy Formation

Similar experiments have been performed in order to determine the impact of Al contact width on alloy formation. The contact area has been varied for Al line widths,  $d_2$ , in the range of  $600$  to  $900 \mu\text{m}$ , showing similar results for mc-Si material. For simplicity, we will analyze the contact resistivity and contact formation for  $d_2 = 700 \mu\text{m}$  (*i.e.* Al line width is kept constant).

For the analysis on mc-Si material, we concentrate on the absolute contact resistance ( $R_C$ ) and contact resistivity ( $\rho_c$ ), due to the important impact of both factors on the understanding of series resistance losses in the solar cell<sup>†</sup>.

Figure 6.3 presents the TLM measurement results for the absolute contact resistance  $R_C$  and the calculated contact resistivity  $\rho_c$  of a  $700 \mu\text{m}$  Al line width,  $d_2$ , alloyed on four different LCO widths ( $d_1$ :  $80$  to  $170 \mu\text{m}$ ).  $R_C$  is the measured value

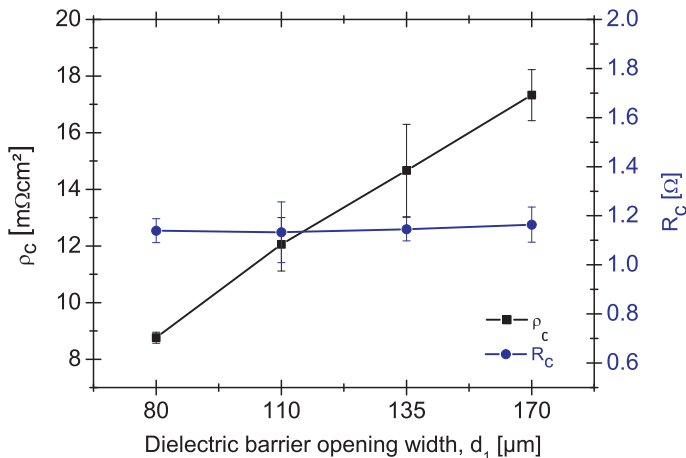


Figure 6.3: Y-axis on the left: Contact resistivity  $\rho_c$  [ $\text{m}\Omega\text{cm}^2$ ] of a  $700 \mu\text{m}$  Al line width,  $d_2$ , alloyed on four different dielectric barrier opening widths,  $d_1$ . The error bars represent the variation of  $\rho_c$  for different firing conditions. Y-axis on the right: Total contact resistance  $R_C$  not increasing for broader openings.

<sup>†</sup>As treated in chapter 3,  $\rho_c$  is a strong evaluator of ohmic contacts.

in the experiment and  $\rho_c$  is calculated from  $R_c$  after the TLM method [63, 67, 132]. The error bars show the variation of  $\rho_c$  for the different firing conditions. No variation was measured for the total contact resistance  $R_c$ . The results show a dependence of the contact resistivity on the dielectric barrier openings, but less on the firing temperature. From the TLM method this would be the case if the transmission length,  $L_T$ , is small and the current transfer is only located at the edges of the contact.

The contact resistivity depends on the doping and temperature [63, 67, 132]. Thus, our measurements are in contradiction to the expected results. Melczarsky *et al.* [133] found a variation in the contact resistance of screen-printed Ag lines, and discussed the findings as a result of the inefficiency of the TLM method. They explained this variation by means of SEM analysis on etched samples. They found that the variation in the contact resistance is due to the fact that the contact is more strongly applied over the outer boundaries. Finetti *et al.* [134] as well as Kircher [70] explained that the diffusion of Si into Al starts locally at some favourable weak spots at the interface. It means that Si can diffuse and enter into Al, by reducing the driving force for diffusion to occur at other places [70].

#### 6.3.4 Cross-sectional SEM/EDX Analysis of the Alloy Junction

To gain an understanding of our results and based on the literature mentioned above, part of the extended SEM analysis performed in cross-sectional micrographs is illustrated in Figure 6.4 (the interdiffusion between Al and Si will be discussed further in section 6.4). As already presented in the previous chapter, during the alloying process of Al on Si, the solid Al particles change to liquid state above the melting point of Al, starting to alloy locally on the Si surface. The reduction of the dielectric barrier opening width causes a higher flow of Al material into the Si wafer, as shown in Figure 6.4(a). Since the applied Al-paste does not fire through the dielectric barrier, the offered Al material overlap alongside the dielectric opening may be strongly attracted into the Si substrate (similar results were observed by other authors, see reference [128]).

Consequently, the liquid Al-Si lake penetrates into the openings, increasing the penetration depth in the c-Si substrate with temperature. This explains why, after cooling of the material, a strong Al-Si alloy formation is found in the bulk and below the contacts, compared to a fully covered Al back surface for standard solar cells processing. This strong Al-Si alloy formation is present below narrow dielectric opening areas for Al line widths wider than 500  $\mu\text{m}$ , and 25  $\mu\text{m}$  thickness.

Figure 6.3 shows an increase of the contact resistivity of approx. 8 to

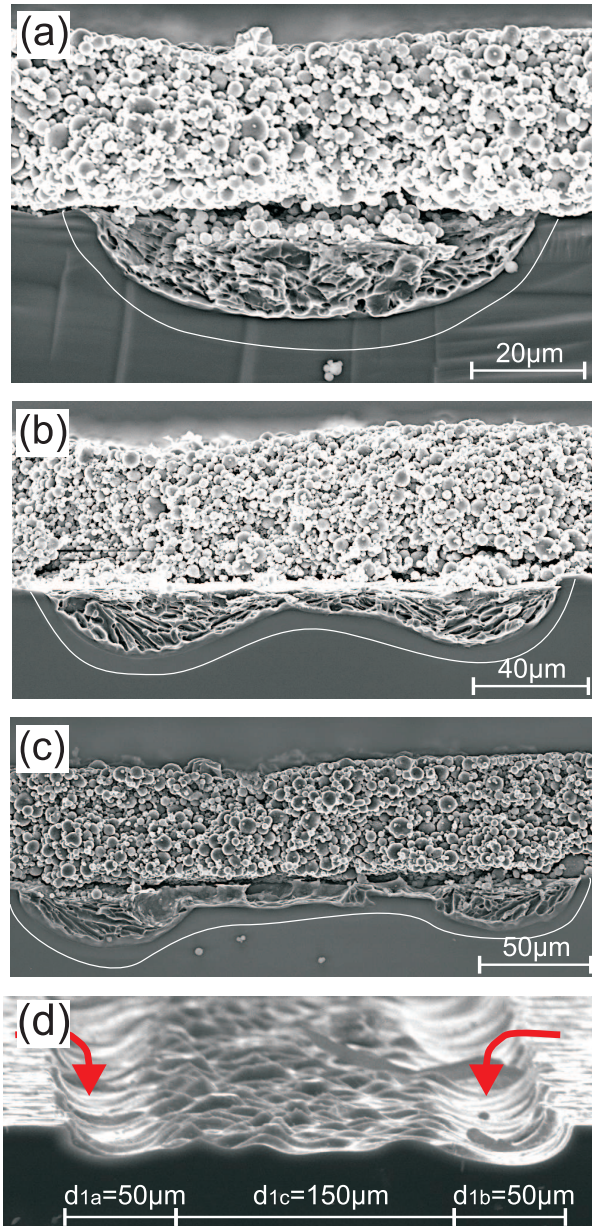


Figure 6.4: Cross-sectional SEM micrographs of Al-Si alloying junction for different contact areas. The local BSF (up to 10 μm deep) is marked and formed few μm underneath the dielectric barrier. (a), (b), (c) represent a 700 μm Al line width printed on 80, 170 and 250 μm dielectric barrier openings, respectively. (d) view of (c) after complete removal of the Al-Si alloy and Al matrix, using HCl.

16 m $\Omega$ cm<sup>2</sup>, after increasing the dielectric barrier opening widths,  $d_1$ , from 80 to 170  $\mu$ m, respectively. As a direct consequence of this result, the cross-section of the alloyed junction structure presented differences in the geometry of the alloy, as shown in Figure 6.4(a) and (b), respectively. Since the same screen printed Al mass, the same Si material and firing conditions were used for this experiment, the reduction of the contact resistivity may be caused by the geometry of the Al-Si alloy formation. In conclusion, by increasing the ratio of the printed Al line width to the dielectric barrier opening width, the alloying of Al into the Si material is increased (penetrates deeper into Si), and the contact resistivity is reduced.

For a narrow dielectric opening, a homogeneous Al-Si alloy and local BSF are deeply formed in the barrier opening. The local BSF layer is found 5 to 8  $\mu$ m deep below the eutectic form, and extends underneath the dielectric layer. For a wider dielectric opening, with the same firing and Al finger geometry, the alloy presents an inhomogeneous geometry formed by two strong alloy formations at the edges and a planar surface in between. By further increasing the dielectric barrier opening width, the Al-Si alloy starts to separate into two identical forms at the open edges. After etching away the Al matrix and Al-Si alloy of Figure 6.4(c) by HCl, the shape of the alloy formation in the Si substrate is found, as shown in Figure 6.4(d). Two strong Al-Si alloy formations are deeply formed at the edges of the dielectric barrier opening, and depend on the offered material overlap of Al-paste alongside the dielectric opening. The width of these two Al-Si alloy formations remains constant ( $d_{1a} = d_{1b} \approx 50 \mu$ m) and does not change for wider dielectric openings (if the overlap of Al lying on the dielectric remains). Between these two formations a planar surface appears and its width varies proportional to the dielectric opening width ( $d_{1c}$ ).

This shallow alloyed area (Figure 6.4(c), middle part) is normally found at the rear of a standard solar cell process after the alloying of a fully covered Al surface on the Si substrate (eutectic layer, 10  $\mu$ m deep<sup>‡</sup>).

As presented by the arrows in Figure 6.4(d), the Al-Si alloy appears after cooling and recrystallization of the Al-Si in liquid phase. The thickness of the Al line mass (20  $\mu$ m for Al lines wider than 500  $\mu$ m), overlapped on the left and on the right of the dielectric opening, is responsible for the width ( $d_{1a}$ ,  $d_{1b}$ ) of the homogeneous Al-Si alloy formation.

Therefore, if the dielectric barrier opening formed by etching paste is wider than the optimum need for a lower contact resistivity ( $d_1 \geq 100 \mu$ m), two deeply

---

<sup>‡</sup>For Al-BSF cells, the area of the thick Al layer is equal to the Si area, showing a higher vertical Al-Si interdiffusion, than a horizontal one. Due to the large Al-Si interface the melt saturates faster than in the case of LCOs, where only a narrow Si area interacts with the fully covered Al layer. This is considered in the following studies.

alloyed regions appear at the edges ( $d_{1a} + d_{1b} \approx 100 \mu\text{m}$ ) of the dielectric opening, separated by the shallow alloyed surface ( $d_{1c}$ ) in between. Comparing this analysis with the contact resistance results, the planar surface is useless in the development of solar cells with rear fine Al lines as contacts, because it contributes to a high contact resistivity. Thus, we can assume an infinite contact resistivity for the planar surface ( $\rho_{d_{1c}} \rightarrow \infty$ ). If this variable planar surface is removed from each opening presented in Figure 6.4, the contact resistivity of the screen printed Al lines on  $p$ -type Si areas should be constant. We can assume again that the contact resistivity of the effective contact area  $\rho_{c,local} = d_{1a} + d_{1b}$  is constant. It is assumed that the contact resistivity should remain constant for the same Al mass alloyed on narrower contact areas than presented in this work. The maximum for the contact size found here, is not the absolute maximum, and narrower openings than  $50 \mu\text{m}$  may have also applications in industrial solar cells. However, the Al spiking may be an issue when high Al amounts are screen-printed.

### 6.3.5 On the Variation of the Contact Resistivity

A mathematical approach to understand the variation of the contact resistivity as presented in Fig. 6.3 is as follows. If the contact resistivity depends on the contact area,  $\rho_c$  is a function of  $d_1$ , one gets:

$$\rho_c^{-1} = \frac{1}{d_1} \left( \frac{d_{1a} + d_{1b}}{\rho_{c,local}} + \frac{d_{1c}}{\infty} \right) \quad (6.1)$$

Thus,  $\rho_c$  increases with increasing  $d_1$ , as shown in the present work.

As illustrated in Figure 6.5(a) an effective contact surface should be taken into consideration for the TLM calculations. Figures 6.5(b) and (c) show the shape of the alloy formation (two alloy indentations separated by a plateau) after HCl etching. The real contact surface is not two times the radius  $r$  of the circle (interface Al matrix/Al-Si eutectic), but two times  $l_1$  (direct contact of Al-Si eutectic to Si bulk). The two alloy forms found at the edges of broader openings present similar geometry (Figure 6.5(c), red lines). The direct surface of contact ( $2l_1$ ) remains constant and does not change for wider dielectric openings. Just the inhomogeneous and planar surface in between (Figure 6.5(c), black dashed line) is changing and its width varies proportional to the dielectric opening width. The two separated Al-Si alloy indentations appear at the edges of dielectric openings broader than  $80\text{-}100 \mu\text{m}$ . From the Figure one sees that

$$l_1 > r \quad (6.2)$$

Experimentally we have found that,

$$l_1 \approx 1.3r \quad (6.3)$$

During the TLM measurement, the surface  $2r$  should be replaced by  $2l_1$  for the calculation of the contact resistivity, where  $2l_1$  is the surface of contact for the Al-Si alloy to the  $p$ -type Si bulk. Now the real contact surface for a narrow opening of  $80 \mu\text{m}$  ( $r = 40 \mu\text{m}$ ) is:

$$2l_1 = 2(1.3r) = 104 \mu\text{m} \quad (6.4)$$

Assuming that the entire contact length  $2l_1$  contributes to current transfer [63], one gets:

$$\rho_{c,local} = R_c A_c = 1.1[\Omega]1[\text{cm}]2l_1[\mu\text{m}] = 11.4 \text{ m}\Omega\text{cm}^2 \quad (6.5)$$

with a sample width of 1 cm. The contact resistivity of a  $700 \mu\text{m}$  Al line contacted on an  $80 \mu\text{m}$  dielectric barrier opening is hence  $11 \text{ m}\Omega\text{cm}^2$ , where the effective

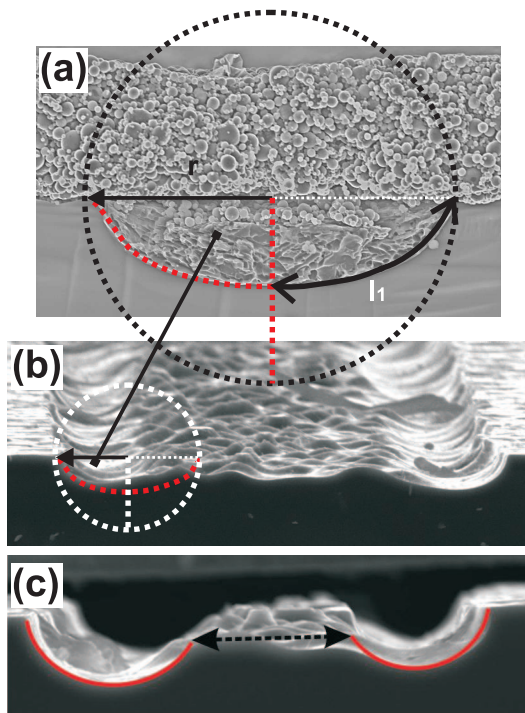


Figure 6.5: (a) Model to calculate the real contact surface  $2l_1$ . (b) For broader openings a plateau appears between the two deep indentations at the edges. Its width increases with the dielectric opening width. (c) Direct contact surface (red). Inhomogeneous surface of contact (black), increasing the contact resistivity.

contact surface is  $104\ \mu\text{m}$  of width. This value is independent of the contact area ( $\rho_{d1c} \rightarrow \infty$ ).

Our analysis compared with the contact resistance result leads to the conclusion that the planar surface (dotted line in Figure 6.5(c)) does not contribute to the reduction of the contact resistance. If we just take the effective contact surface  $2l_1$  into consideration, and remove the variable planar surface from the calculations, the contact resistivity of screen printed Al lines on  $p$ -type Si areas should be constant. Additionally, we assume that the contact resistivity remains constant when the same Al amount is printed on even narrower contact openings than the ones presented in this work.

### 6.3.6 Experimental Evidence of the Influence of Al Amount on Mass Transport

Additional experiments were performed, in order to corroborate the fact that the Al-Si alloy formation depends on the ratio of printed Al line width to the dielectric barrier opening width. A wide Al line (width  $d_2$ ) was screen printed on a narrow dielectric opening width  $d_1$ , with intentional misalignment for the screen printing process, as shown in Figure 6.6(a). More Al-paste is present overlapping the right side of the opening than to left. A stronger Al-Si alloy formation is found at the edge on the right side, where more Al mass has penetrated during the firing process, proving that the formation of the Al-Si alloy is improved by higher ratios of printed Al line width to dielectric barrier opening width.

Figure 6.6(b), summarizes the experiments performed. In the top, the optimal structure for a rear passivated solar cell device with screen-printed Al lines on  $p$ -type Si material is presented ( $50$  to  $80\ \mu\text{m}$  dielectric opening width,  $700\ \mu\text{m}$  Al line width). The higher the ratio  $d_2/d_1$  (Al line width to dielectric barrier opening width), the deeper the Al-Si alloy formation and the lower the contact resistivity. Middle: wider opening areas lead to a planar surface between two Al-Si alloy formations, generating a high contact resistivity, as already shown by the TLM results. Bottom: the Al-Si alloy formation depends strongly on the Al mass overlapped on the dielectric.

### 6.3.7 Conclusions

The following dependencies of the contact resistivity have been shown: First, by increasing the ratio of the printed Al line width to the contact opening width, the alloying of Al into the Si material is increased. The contact resistivity is reduced

by increasing this ratio. Second, identical Al-Si alloy formations with equal width appear at each of the two edges of the contact opening, if the opening is wider than  $100\ \mu\text{m}$ , and if the Al lines are wider than  $500\ \mu\text{m}$  (and their thickness is about  $20\ \mu\text{m}$ ). When the opening width is increased further, a planar surface is formed between these two Al-Si alloy formations (similar to that of standard solar cells with fully covered Al rear surface), which may increase the contact resistivity. To obtain a low contact resistivity for the design of the back contacts of the rear passivated solar cell I conclude that small contact areas are required. As a consequence, less surface needs to be metallized and the non-contacted area with low recombination under the passivation layer is maximized.

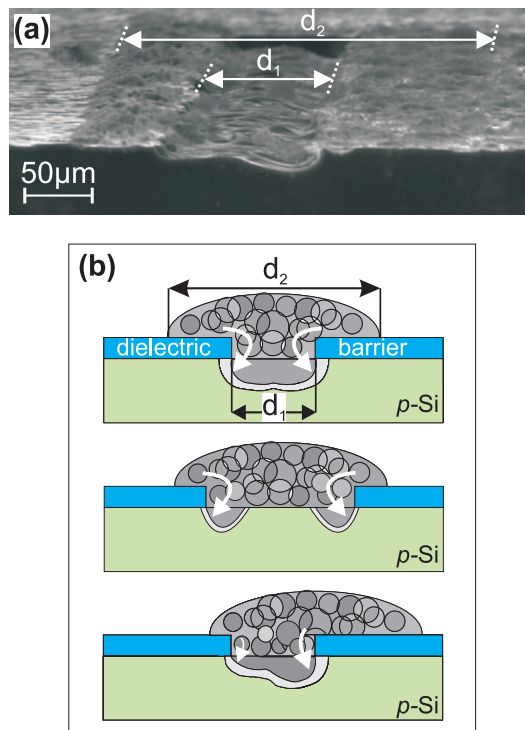


Figure 6.6: (a) Cross-sectional SEM micrographs after HCl etching of the Al matrix and Al-Si alloy for a sample printed without alignment. (b) Schematic cross-section of the experiments done for this article, not to scale ( $d_2 \gg d_1$ ): Top: Al-Si alloy homogeneous formed for narrow dielectric barrier openings; Middle: two alloys formed at the opening edges for wider contact areas and the same Al mass; Bottom: the Al-Si alloy depends on the ratio: Al-line width to dielectric barrier opening width.

## 6.4 Study 2: Diffusion of Silicon into Screen-Printed Aluminum Paste

### Abstract

In this section, the lateral spread of Si in the screen-printed Al layer applied in this study is found to increase by  $(1.50 \pm 0.06) \mu\text{m}/^\circ\text{C}$  when increasing the peak firing temperature within an industrially applicable range, and an explanation is given. Therefore, the total spread limit of diffused Si in Al becomes predictable and independent of the contact area size. However, it is found to be dependent on the firing temperature (it was determined by SEM and optical microscopy analysis). The geometry of the rear side pattern can influence not only series resistance losses within the solar cell, but the process of contact formation itself. Based on the interdiffusion of both elements, an explanation for the formation of cavities (voids) instead of eutectic layers is confirmed. Cooling too fast also leads to void formation instead of an eutectic layer.

### 6.4.1 Experimental Design

In the previous section, it has been shown that a wide overlap of Al on each side of the local contact opening is essential for a well-formed local BSF and the minimization of the contact resistivity. Thereby, the design of the rear side pattern can influence the series resistance and the process of contact formation. In this section the interaction during the alloy between Si and Al, based on the diffusion process of Si in the Al matrix is studied.

Figure 6.7(a) shows a cross-sectional schematic model of the rear passivated solar cell with a fully covered Al rear side, as already presented in chapter 4.

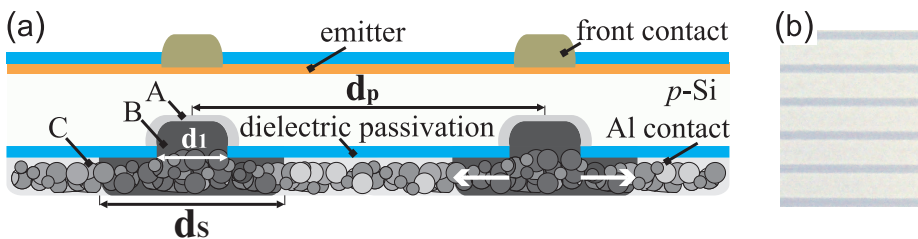


Figure 6.7: (a) Rear passivated solar cell in cross section (front side simplified).  $d_1$ : width of LCO.  $d_s$ : spread limit of Si in Al.  $d_p$ : contact spacing. A: local BSF. B: eutectic layer. C: Al layer. (b) Section of the rear side of a solar cell, where dark-gray lines are visible (not to scale).

Three variables describe the rear side structure: the width of the LCOs,  $d_1$ ; the maximum spread limit of diffused Si in Al layer,  $d_s$ ; and the contact spacing,  $d_p$ . Hence,  $(d_s - d_1)/2$  represents the spread of Si in Al on each side of the LCO (away from the contact area). As presented by the cross-sectional model of Figure 6.7(a), the contact area between Si and Al is restricted to the LCO,  $d_1$ . An Al layer fully covers the rear surface. The local BSF forms in the LCOs at the rear of the device structure due to local Al-Si interaction. The microscope image of Figure 6.7(b) shows a section of the rear side of a processed solar cell with the same rear structure as shown in Figure 6.7(a). The dark-gray regions (within  $d_s$ ), which are visible after firing in the Al layer, do not represent the local BSF formation because they are wider than the LCOs ( $d_s > d_1$ ). The understanding of this phenomenon motivated the development of the present study. These regions show different contrast due to the difference of composition within the Al matrix.

Polished *p*-type Cz-Si wafers with  $1.5 \pm 0.5 \Omega\text{cm}$  resistivity were used for this study. A broad range of  $d_1$  was chosen between 100-500  $\mu\text{m}$  in steps of 50  $\mu\text{m}$  (the real values are  $\approx 20 \mu\text{m}$  broader due to the spreading of the etching paste). A state-of-the-art 20-30  $\mu\text{m}$  thick Al contact was screen-printed, fully covering the rear passivation layer and the opening lines. The alloy was formed after sintering the samples using a standard firing furnace profile. Three peak firing temperatures were applied: 750, 850, and 950  $^\circ\text{C}$ . The widths of the sharply limited visible dark-gray regions ( $d_s$ ) were measured by optical microscopy.

#### 6.4.2 On the Spread of Si in Al and the Formation of Voids

The three layers forming the alloy junction (A, local BSF; B, eutectic; C, Al matrix. See Figure 6.7(a)) were characterized by SEM and EDS/EDX. For rear passivated solar cells, we redefine the Al layer in two regions, depending on the distribution and concentration of Si in Al: (1) the visible dark-gray region (within  $d_s$ ) and (2) the rest of the Al layer formed by solid particles of the Al paste.

The regions of interest in the Al matrix were analyzed by optical microscopy. Figure 6.8 shows on the *y*-axis the width of the dark-gray regions (spread limit of Si in Al,  $d_s$ ), vs. the peak firing temperature, for different LCO widths,  $d_1$ . For a LCO of 500  $\mu\text{m}$ , the error bars show the small standard deviation of the optical microscopy analysis. For three  $d_1$  values, a linear fit is illustrated as a guide for the eye. The same linear dependency on the peak firing temperature is remarkable for all data. The slope of the line is  $(3 \pm 0.12) \mu\text{m}/^\circ\text{C}$  which means, that on each side of the LCO the spread of Si increases by  $(1.50 \pm 0.06) \mu\text{m}/^\circ\text{C}$ . Additionally, the lateral spread limit of Si from the edge of the LCO,  $[d_s - d_1]/2$ , is determined

as follows:  $(75 \pm 9) \mu\text{m}$  at  $750^\circ\text{C}$ ,  $(225 \pm 30) \mu\text{m}$  at  $850^\circ\text{C}$ , and  $(375 \pm 90) \mu\text{m}$  at  $950^\circ\text{C}$ . These results show that for a certain firing temperature the spread limit of Si in the Al layer is constant and independent of the width of the LCO. Therefore, the maximum spread limit of diffused Si in Al is predictable.

To gain an understanding of the distribution of Si in the Al layer a further analysis is required. A line scan was performed by EDX in the Al-Si alloying structure for two samples fired at the high temperature of  $950^\circ\text{C}$ . The SEM cross-sectional micrographs and the EDS/EDX results are shown in Figure 6.9 for two samples fired at the same peak temperature and using the same amount of Al paste. The difference lies in the LCO of (a)  $80 \mu\text{m}$  and (c)  $125 \mu\text{m}$ , respectively. Although the formation of voids was randomly present for all device structures, for the purpose of discussion a sample with alloy formation at the Al-Si interface was chosen for  $d_1 = 80 \mu\text{m}$  [Fig. 6.9(a)] and a sample with a void was chosen for  $d_1 = 125 \mu\text{m}$  [Fig. 6.9(b)].

The Si content was measured from the center of the LCO,  $200 \mu\text{m}$  to the left and right. Although the results of this method are influenced by structural inhomogeneities of the Al layer [135], we see that the Si concentration in the Al decreases with increasing distance from the center of the interface (center of LCO), as already published elsewhere [136, 137] [see Figure 6.9(b)]. The

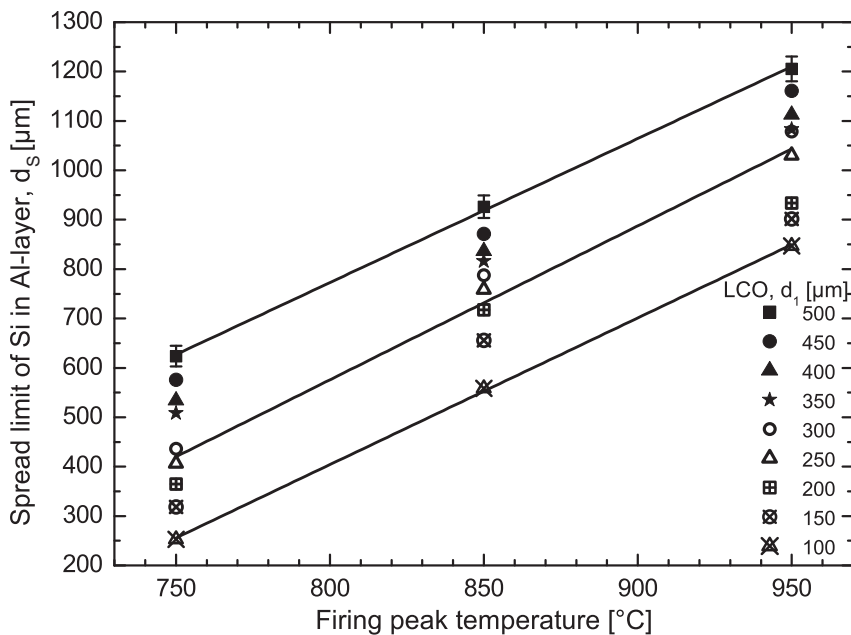


Figure 6.8: Temperature linear dependency of the spread limit of Si in the screen-printed Al layer. Error bars shown for  $d_1 = 500 \mu\text{m}$ .

exponential decrease with the length for the concentration of Si in Al is evident due to the Fick's law of diffusion [102]

Figure 6.9(a) shows an eutectic layer formed below the Al layer for  $d_1 \approx 80 \mu\text{m}$ . Its Si concentration, as presented in Figure 6.9(b), follows a Gaussian fit [137] centered at the LCO, decreasing to the left and right to the measured spread limit of  $375 \mu\text{m}$ . From the Gaussian fit, the maximum concentration is represented by 27 counts, and the concentration at the respective spread limit  $d_S$  is represented by 3 counts approximately. For a high peak firing temperature of  $950^\circ\text{C}$  a Si concentration of  $C[(d_S - d_1)/2]/C_0 \approx 11\%$  (hypoeutectic [114]) is still present in the Al layer at the spread limit of Si,  $375 \mu\text{m}$  from the LCO. The local BSF forms homogeneously below the contacts, up to  $8 \mu\text{m}$  deep. Thus, the concentration of Si in the Al layer is inhomogeneously distributed for this type of structures at the rear of solar cells.

Figure 6.9(c) shows no eutectic layer formed below the contacts, but instead shows a void. For this sample, the Al was deposited on a broader contact opening ( $d_1 \approx 125 \mu\text{m}$ ) and fired at the same high peak firing temperature of  $950^\circ\text{C}$  (fast cooling). In contrast to other authors [138], a homogeneous local BSF forms below the void. The Si composition in the Al layer, for the sample with a void, is shown in Fig. 6.9(d). It is described as an irregular form with a higher concentration at

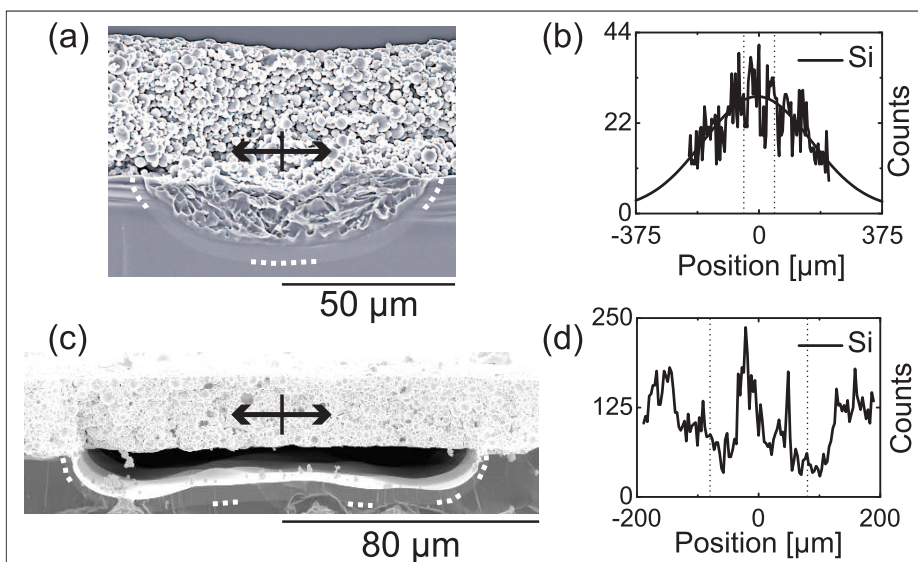


Figure 6.9: SEM/EDX analysis. (a)  $80 \mu\text{m}$  LCO, eutectic and local BSF formed. (b) EDX analysis of (a) and Gaussian fit, following the Si concentration to the spread limit at  $375 \mu\text{m}$ . (c)  $125 \mu\text{m}$  LCO, void and BSF formed. (d) EDX analysis of (c). The dotted lines in (a), (c) delimit the BSF; in (b), (d) the region presented by the SEM figures.

the center of the opening and two maxima located more than 150  $\mu\text{m}$  away from the center of the opening, to the left and right.

### 6.4.3 Discussion

Similar conclusions as presented in this chapter were drawn by Kircher [70], and by McCaldin and Sankur [137] for the diffusion of Si on evaporated Al thin layer (20 times thinner than a screen-printed layer). They also found a reduction of the Si concentration in the thin Al layer adjacent to the dielectric opening (similar to the two maxima for the concentration of Si as shown in Fig. 6.9(d)). They explained this phenomenon to be related to the Si diffusing back during cooling and regrowing epitaxially on the Si surface, during a relatively slow cooling.

The liquid Al wets the Si surface in the dielectric openings, and then Si dissolves in the Al layer. It is well known that the depth of penetration of Al-Si melt into the Si wafer is a function of the temperature and of the spherical diameter of the Al particles [139]. However, the penetration of the liquid Al-Si also depends on the diffusion of Si in Al. Thus, for a large initial concentration of Si in Al, the penetration of the melt will be reduced [140].

In our case for a peak firing temperature of 950  $^{\circ}\text{C}$ , the depth of penetration is 20  $\mu\text{m}$ , as illustrated in Figure 6.9(a), (c). Due to the higher solubility of Si in Al than that of Al in Si [137, 141], a higher volume of Si atoms diffuse into the Al than Al atoms into the Si. If the peak firing temperature is high, the diffusion is enhanced and Si spreads faster into the Al layer. At the interface, the Al in direct contact with the Si bulk saturates first, as the Si diffusion proceeds from the edges of the interface in both lateral directions into the liquid Al (not yet saturated by Si). After a few seconds, a large amount of Si atoms is found in the Al layer, more than 370  $\mu\text{m}$  from the contact area. In the case of a standard solar cell where the effective contact area of Si is equal to the area of the deposited Al contact, the interdiffusion achieves an equilibrium at the peak temperature where no more Si diffusion into Al is present (saturation). Thus, following the Al-Si phase diagram, the concentration of Si in the melt is constant at the peak temperature. By cooling the sample, the composition of Si in the liquid-phase has to decrease following the liquid curve of the binary system [113] (segregation).

However, this may not be the case in our experiment, where a large Al contact lying on dielectric barrier is forming contact only with a narrow Si surface. In this case, if no saturation of Al by Si is present, then Si keeps diffusing into Al for a few seconds at the peak temperature. As shown by some authors, a high elastic stress field may occur in the melt during the alloying [142] between two

elements with different diffusivities (this is the case between Al and Si: Si has higher diffusivity in Al, than Al in Si [141]). The high generation of vacancies during interdiffusion of two elements with different diffusivities may coalesce in the melt, causing the nucleation and formation of Kirkendall [143] voids [142] (cavities between two elements in direct contact).

As shown in Figure 6.9(c), a local BSF is formed below the void which represents the epitaxial growth of Si on the bulk surface during cooling. Thus, this result explains that the void forms during the cooling of a hypereutectic melt, during the epitaxially recrystallization of Si at the interface.

Immediately after the formation of the void (during cooling), only the edges of the LCO are still in direct contact with the Al layer. Thus, at this point there is almost no contact surface between Al and Si for the segregation of the diffused Si. By reaching the eutectic temperature, the whole remaining liquid solidifies and the Si is trapped in the Al matrix, thus, a high concentration of Si is present in Al, away from the surface of contact [shown by the two maxima of Figure 6.9(d)].

If the interaction between Al and Si takes place only within  $d_S$ , where a visible dark-gray region is sharply delimited, the spread of Si in the Al layer is diffusion-limited. Thereby, an exponential decrease with the distance from the center of the interface is evident due to the Fick's law of diffusion [102].

Since the diffusion of Si in the liquid Al proceeds laterally within the Al layer, a determined amount of Al ( $d_2 > 500 \mu\text{m}$ , see section 6.3) should overlap each side of the dielectric opening to achieve an optimal metal-semiconductor interaction. This overlap of Al on narrow dielectric openings is evident due to the reduction of the contact resistivity and the homogeneous formation of the local BSF. We suggest that the maximum spread limit of diffused Si,  $d_S$ , should be considered during the optimization of the Al metallization in order to achieve an optimal contact and full local BSF formation. Thus, the effective Al mass interaction with Si during the alloying is determined by  $d_S$ . However it has been shown here that an amount too large of unsaturated Al may enhance the formation of voids instead of Al-Si alloy layers. Thus, another parameter to analyze the local contact formation between Al and Si is the contact spacing,  $d_p$ , which may be related to  $d_S$ . Another application of the Al overlap may be found on interdigitated back contact *n*-type Si solar cells to obtain high-quality screen-printed Al-alloyed emitters.

#### 6.4.4 Model of Local Contact Formation

Figure 6.10 aims to explain the contact formation when the contact area is reduced (variation of dielectric opening width). A Si wafer [Si(S)] is coated by a

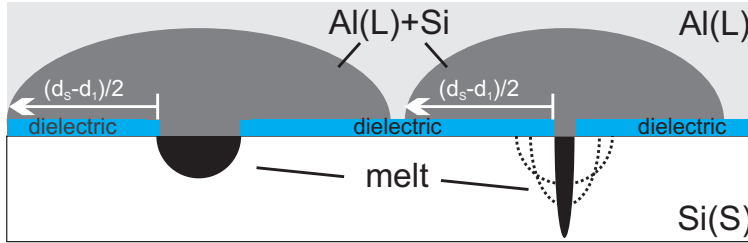


Figure 6.10: Schematic model in cross-section of the alloying process between Al and Si, when the contact area is reduced. During this reduction, the spread of Si in Al remains constant and its value depends on the firing temperature (diffusivity of Si into Al during firing). The volume of liquid Al with dissolved Si atoms from the interface is represented by a dark gray color. This color represents the characteristic zebra pattern found at the rear side of PERC solar cells. The reduction of the contact area influences the depth of penetration of the melt into the Si bulk. Contact areas which are too narrow may induce Al spiking.

dielectric layer (blue), which is fully covered by an Al paste (gray). Two contact areas are obtained in the dielectric barrier by a wide and a narrow laser line. The contact areas are well separated from each other. The figure shows the alloying process for both isolated systems. The dissolution of Si in liquid Al [Al(L)] is limited by the temperature and the spread in the Al matrix, determined by  $(d_s - d_i)/2$ , is known from the present work to remain constant for the same firing profile, not varying with the contact area. When assuming the same firing parameters and cooling rate, the mass transfer and interdiffusion between Al and Si must remain the same for both systems (for the same temperature, the same volume of Si atoms are dissolved into the Al). Therefore, it can be assumed that a decrease of the contact area must vary the depth of penetration of the melt into the Si bulk. In other words, the Al volume is responsible for dissolution of Si atoms during alloying and both, the contact area and firing temperature, are responsible for the depth of penetration of the melt in the bulk material. Our model may thus explain the formation of Al spiking at the interface.

#### 6.4.5 Summary and Conclusions

In conclusion, further understanding of the local contact formation between screen-printed Al paste and narrow Si contact areas has been provided. The spread of Si in a screen printed Al layer increases by  $(1.5 \pm 0.06) \mu\text{m}/^\circ\text{C}$  when increasing the peak firing temperature in a range of 750-950 °C. This lateral spread limit of Si, on each side of the dielectric opening, does not depend on the contact area size but on the firing temperature, and is measured as 75, 225,

and 375  $\mu\text{m}$  for 750, 850, and 950  $^{\circ}\text{C}$ , respectively. Thus, the optimum width of the Al contact may be determined by the maximum spread limit of diffused Si in an Al layer. The impact of this result on the contact spacing will be analyzed in the next section. It is not clear yet whether the contact spacing should be smaller or larger than the maximum spread limit of diffused Si in Al. Additionally, an explanation is given for the voids formed instead of Al-Si eutectic layers, based on the difference of diffusivities between Al and Si, and it has been mentioned that the voids may be formed during cooling.

## 6.5 Study 3: Distribution of Silicon in Aluminum and the Influence of Contact Pattern on Contact Formation

### Abstract

In this section the influence of the geometry of the rear pattern (contact size and contact spacing) on the Al-Si interaction in the local contact openings is studied. In the previous section, it has been demonstrated that Si diffuses into the Al through narrow dielectric barrier openings and spreads laterally to a determined limit given by the firing temperature. The purpose of this section is to show that the contact spacing can affect the tendency of formation of voids below the Al-Si contacts instead of an eutectic layer. When decreasing the contact spacing and therefore the overlap of Al on each side of the local opening, the melt saturates faster and the formation of a high-quality local BSF is increased, also minimizing the presence of voids. This physical observation can enhance the design of the rear pattern for rear passivated solar cells and give further understanding of the Al-Si interaction during the firing process. The minimum contact spacing allowed for an optimal rear side pattern may be based on the interdiffusion between liquid Al and Si, during the sintering process.

### 6.5.1 Experimental Design

The local contact formation between Al and Si is strongly influenced by the distribution of Si in the Al matrix. It has been shown in literature, that rear passivated solar cells fired with non-optimal parameters suffer from large losses in FF compared to reference Al-BSF solar cells, using industrial screen-printing Al pastes [18, 85]. The formation of voids during the sintering between screen-printing Al pastes and Si may be the answer for those FF losses.

The influence of the contact spacing on the formation of eutectic layer and local BSF was analyzed. Contact spacings,  $d_p$ , were chosen from 0.1 to 2 mm, keeping the opening size,  $d_1$ , constant at 70  $\mu\text{m}$  [following the model presented in Figure 6.7(a)]. The variation of  $d_p$  is achieved by laser ablating lines in the dielectric layer. The samples are fully covered by Al in order to analyze the diffusion of Si in the Al matrix. Different peak firing temperatures are used for contact sintering. Both, the thickness of the Al matrix and the alloying time are kept constant. Their influence on the contact formation is not studied here, but it may be interesting for further work and understanding.

### 6.5.2 Influence of Contact Pattern on Contact Formation

SEM analysis was performed to measure the geometry of the formed eutectic, the depth of the local BSF and the presence of voids. The analysis is shown in Figure 6.11 and summarized in Table 6.1. The contact formation is strongly influenced by the contact spacing. As presented in the example, for a contact spacing of 0.1 mm ( $d_p < d_s$ ), a thin eutectic layer is found, mainly due to the limited vertical Si diffusion in the Al matrix, and the BSF is deeply formed [Figure 6.11(a), (d), Figure 6.12(b)]. For small contact spacing a homogeneous Si distribution in hypereutectic composition is found in the Al matrix as normally presented in fully covered Al-BSF [Figure 6.11(d)]. For contact spacing larger than the spread of Si in Al ( $d_p > d_s$ ), the dark-gray regions separate, and the presence of voids increases, enhancing their penetration depth in the Si. Above a contact spacing of 700  $\mu\text{m}$  the presence of voids is strongly increased (no local BSF formed).

It has been suggested already in the previous study, that the explanation for void formations in locally contacted rear passivated solar cells, may be found in the Si diffusion in Al, which is increased by larger contact spacing and high peak firing temperatures. It has been also mentioned that the void formation may be related to the Kirkendall effect [143]. This effect occurs during the interaction of two materials with different diffusion rates within each other which are in contact

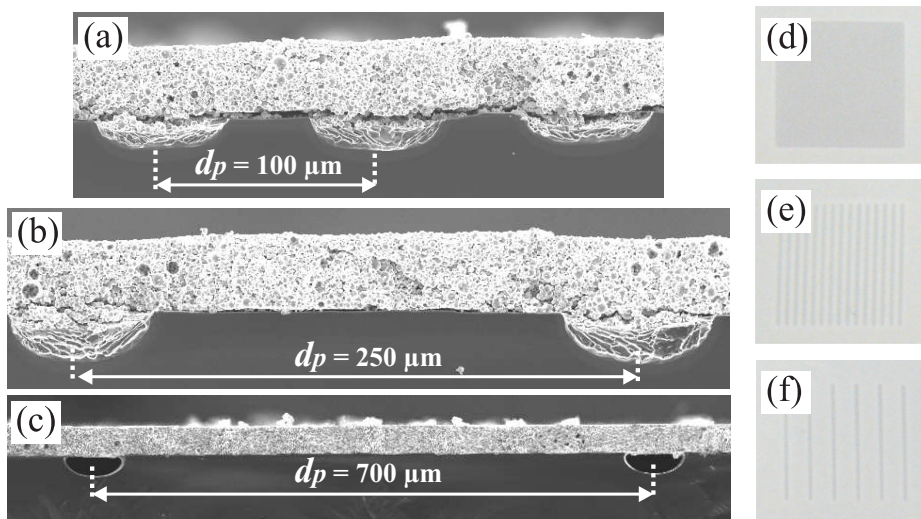


Figure 6.11: (a)-(c) SEM micrographs of samples with different contact spacings  $d_p$ , 100  $\mu\text{m}$ , 250  $\mu\text{m}$ , and 700  $\mu\text{m}$  respectively. (d)-(f) Real pictures of the Al matrix after firing for (a)-(c), respectively, showing the dark-gray regions in Al,  $d_s$ , formed by the spread limit of Si in Al.

across an interface, such as solid Si and liquid Al during contact sintering.

Figure 6.12(b) shows a SEM micrograph of the Al-Si alloyed junction for a LCO of approximately  $70\ \mu\text{m}$ . The well-known three layers formed due to the interaction of Al and Si are presented (Al-matrix, eutectic layer, local BSF). Generally, the Al-matrix has a thickness of about  $20\ \mu\text{m}$ , the eutectic is found to be  $15\ \mu\text{m}$  deep in the Si bulk and approximately  $(70 \pm 5)\ \mu\text{m}$  wide, depending on the dielectric ablation, and the thickness of the local BSF is up to  $7\ \mu\text{m}$  for standard to high temperature firing conditions. The depth of the voids for large contact spacings is approximately a factor of two larger than the depth of the eutectic layer [see Figure 6.12]. This leads us to another conclusion, that voids appear instead of eutectic layers due to the high overlap of melted Al during the sintering process. By increased contact spacing there is no limiting factor for the diffusion of Si in the Al matrix, except the sintering temperature. This phenomenon will be discussed in section 6.7.

Another important conclusion is that the thickness of the local BSF decreases when increasing the contact spacing and that no local BSF was found below the

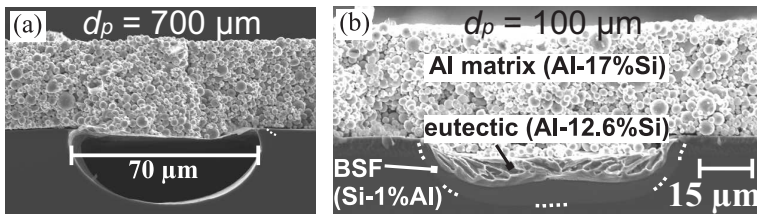


Figure 6.12: SEM analysis for the same Wafer, *i.e.* for the same firing temperature. (a) Void formed by  $d_p \geq 700\ \mu\text{m}$ ; (b) local BSF up to  $7\ \mu\text{m}$  for  $d_p = 100\ \mu\text{m}$ .

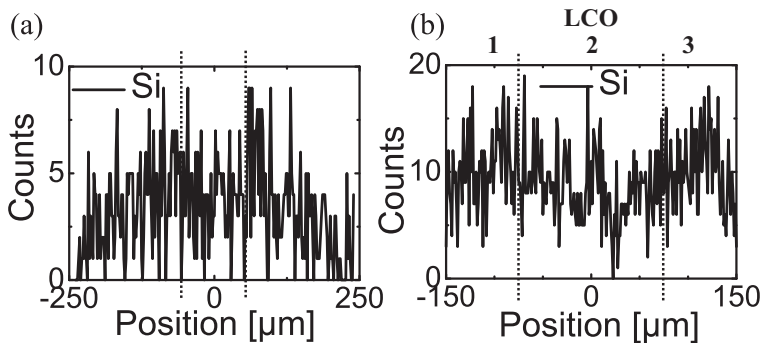


Figure 6.13: EDX line analysis of the Si content in the Al matrix for the samples presented in Fig. 6.12 (the dotted lines delimit the region presented by the SEM figures). (a) EDX scan for  $d_p \geq 700\ \mu\text{m}$  [Figure 4(a)] where a void is formed; (b) EDX scan for  $d_p = 100\ \mu\text{m}$  [Figure 4(b)] extending over 3 LCO with eutectic layer homogeneously formed.

Table 6.1: Analysis of the eutectic geometry, presence of voids and local BSF depth (all results  $\pm 0.5 \mu\text{m}$ ).

$d_p$ [mm]	Eutectic or void depth/length [ $\mu\text{m}$ ]	local BSF [ $\mu\text{m}$ ]	Voids [%]	Figure
0.10	13.60 /67.7	5.7 - 7.0	8	6.11(a), 6.12(b)
0.25	23.15 /70.0	4.5 - 4.7	25	6.11(b)
0.50	23.30 /69.3	2.8 - 3.5	50	-
0.70	23.40 /80.2	4.1 - 4.5	87	6.11(c), 6.12(a)
1.00	27.70 /72.3	-	100	-
2.00	25.40 /75.7	-	100	-

voids for increased contact spacing. Two types of voids were found: voids with and without local BSF (see section 6.7 for the analysis). This may be due to the reduced Si concentration in Al for large spacings. As illustrated in Figure 6.13, an EDS/EDX analysis was performed along the Al matrix (same procedure as shown in the last study), in order to follow the distribution of Si within the Al matrix. A line scan width of  $10 \mu\text{m}$  was used. From the center of the LCO the analysis is performed to the left and right, counting for 300 s. The Si composition decreases exponentially with the length as described by the Fick's law of diffusion [137, 141].

The presence of Si on each side of the LCOs in the Al matrix is demonstrated by the EDS/EDX analysis of Figure 6.13. For small contact spacing ( $d_p$ ) the uncovered Si surfaces are close to each other, and therefore the low overlap of Al mass on each side of the LCOs saturates faster (low distances for the diffusion of Si in Al). This is shown by the almost constant Si concentration in Figure 6.13(b), which shows the result of an EDX line scan extending over 3 LCOs. Thus, the Si concentration in the Al matrix is constant and the eutectic layers are homogeneously formed. For a large contact spacing the growth of voids is increased. For this sample the Si concentration presents two maxima on each side of the opening [Figure 6.13(a)]. Due to the presence of the void during cooling, the contact area is located at the edges of the LCO, where a thin and narrow alloy is found with a respective small BSF formation.

The concentration of Si in the Al matrix is inhomogeneously distributed and much lower than for shorter contact spacings. If the distance of the LCOs is too large, no saturation of melted Al by Si occurs. For large contact spacing, the concentration of Si in the Al matrix may be too low to form an eutectic layer. A deeper explanation is found in the last section of this chapter.

### 6.5.3 Distribution of Si in Al Paste

The atomic concentration in the alloy junction for both samples with and without void formation was measured in two regions: a large volume (large V) covering the overlap of Al and a small volume (small V) directly above the interface, as shown in Figure 6.14. More Si content in volume was found above the void than above the eutectic layer in both regions. For the sample with eutectic layer formed lower Si is found in the matrix due to the Si which recrystallized from the melt to form the BSF and the Si content within the eutectic (approx. 16 at. %). In the case of the void formation, Si must solidify in the Al matrix, and during cooling it is rejected from the Al (diffuses back [70, 137]) and solidifies directly above the void underneath the Al matrix (therefore the content of Si is approx. 18 at. %). Thus, an important conclusion can be drawn here: the volume of Al-Si melt present in the void during the alloying is distributed in the Al matrix, due to mass transport of the melt into the liquid Al, and therefore this Al-Si volume does not contribute to eutectic formation. This process of mass transport may occur before cooling starts.

### 6.5.4 Phenomenon of Lateral Solidification

The cross-sectional sample presented in Figure 6.15 shows two void formations for a sample with large contact spacings. The distribution of Si in Al is also shown. As shown before, the concentration of Si decreases with the length and we can assume that in the center of the Al matrix only Al is present (red box: content of Si = 0 at. %, neglecting impurities).

At the peak temperature the Al mass is found in liquid state and the diffusion of

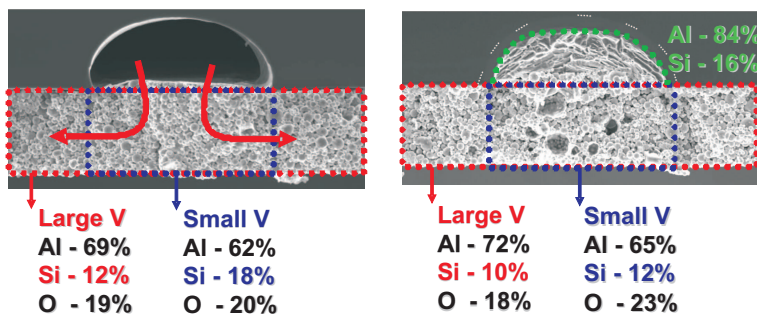


Figure 6.14: EDX volume analysis of the cross-section of the Si distribution in the Al matrix for a sample with a void formation and an eutectic layer. The volume of the Al-Si melt contained in the void during the alloying is distributed in the Al matrix.

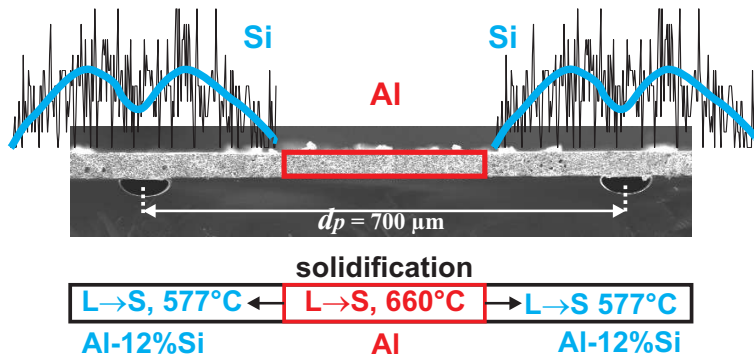


Figure 6.15: Hypothesis of lateral solidification within the Al matrix for large contact spacings.

Si into Al is limited by the contact spacing (contact spacing too large: no saturation is found at this point). When cooling, Si concentration decreases as following the liquidus curve in the phase diagram to solidify the Al matrix in liquid state [116]. The interesting thing here is that Al solidifies at 660 °C, but a mixture of Al and Si will solidify at the eutectic temperature, 577 °C. Thus, the region presented by the red box in the middle part of the Al matrix starts to solidify first and its solidification will continue laterally from the middle in both directions - left and right - to the interface layer. Between 660 and 577 °C lateral solidification within the Al matrix is present to the left and to the right in direction of the contact area.

$$V_{Al(solid)} < V_{Al(liquid)} \quad (6.6)$$

$$\rho_{Al(solid)} > \rho_{Al(liquid)} (\Delta\rho_{rel} \approx 12 \%) \quad (6.7)$$

It is well-known that the volume of a solid is smaller than that of a liquid and a contraction may occur within the Al matrix. The density of Al in solid state is 12 % relatively higher than the density of liquid Al. Thus, the liquid Al content must be attracted to the red box in order to solidify and Si must be rejected to diffuse back to the interface. At the same time, Si from the Al-Si melt at the interface must diffuse back into the bulk forming the BSF. If this phenomenon is happening during cooling, it is still not clear if this hypothesis may also explain the formation of voids at the interface. Nevertheless, lateral solidification may have an impact on the conductivity within the Al matrix due to the contraction of the layer during cooling.

### 6.5.5 Summary and Conclusions

In conclusion, we have shown that the geometry of the rear pattern for rear passivated, locally contacted solar cells influences not only series resistance losses, but also the process of local contact formation between Al and Si. The formation of a high quality BSF is extremely dependent on the Si diffusion in Al and on the overlap of Al on each side of the dielectric opening. The early saturation of the Al-Si melt for small contact spacings may allow the formation of a deep  $p^+$ -doped layer. A unlimited diffusion of Si atoms in Al may explain void formation instead of eutectic layers. The Si diffusion in Al is limited not only by the firing temperature, but also by the contact spacing, determined by the amount of Al mass overlap on each side of the dielectric openings. The Al-Si volume in liquid state present in void during the alloying was found distributed in the Al matrix. This Al-Si volume transported from void to the Al matrix does not contribute to eutectic formation, explaining the process of mass transport and void formation. Furthermore, we believe that the enhanced Si diffusion in the Al matrix could be reduced by introducing Si in the Al paste before the sintering.

## 6.6 Study 4: Effect of Gravity on the Microstructure of Al-Si Alloy

### Abstract

The following section presents a study on the influence of the gravity field orientation on the microstructure of Al-Si forming alloy. Due to the fundamental differences between Al and Si (*i.e.* diffusivity), void formations are often found at the back of rear-passivated solar cells instead of an eutectic layer. It is shown that the voids may partially be avoided by sintering the samples with the solid/liquid interface oriented opposite to the direction of the gravity field. A local BSF is found underneath the voids using this approach. This phenomenon strongly applies to rear-passivated solar cells, which exhibited strong fill factor losses.

### 6.6.1 Experimental Design

Recently, several studies have been focused on the formation of voids in alloys [144, 145]. A strong impact of voids on the electrical and thermal conductivity

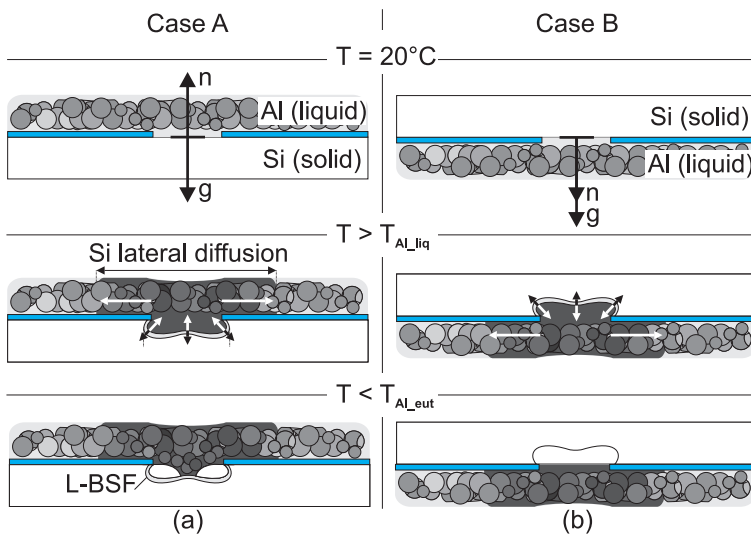


Figure 6.16: Model of the local Al-Si interaction through a dielectric window at different firing temperatures, showing the influence of the orientation of  $g$  (gravity field orientation) and  $n$  (direction of solidification), on the formation of voids. (a) Case A,  $n$  and  $g$  present opposite direction. The voids are partially filled and the BSF is formed. (b) Case B,  $n$  and  $g$  show the same parallel orientation. Too thin BSF is found.

has been shown. It has been mentioned, that the void formation is a result of a system of variables and that each paste is different in its voiding behavior [146].

In this section the microstructure during the transformation from liquid to solid phase is analyzed for both cases, gravity field oriented opposite and parallel to the solid/liquid (S/L) interface (Figure 6.16) and their effect on the formation of voids is analyzed. As in a standard solar cell process, the samples are alkaline textured in order to achieve a pyramidal structure on the surface. An optimized rear side passivation by PECVD technique can be used on the pyramidal structure for high-efficiency solar cell processes (see section 7.10).

Figure 6.16 illustrates the model of the local interaction between Al and Si for three temperatures during sintering. At room temperature (20 °C) the system is at equilibrium. When Al is liquid (above its melting temperature), the interaction starts (Al diffusion into Si, Si diffusion into Al) and a spot of liquid Al-Si is found. In the same place but after cooling (to below the eutectic temperature), the Al-Si eutectic is formed by recrystallization. A parallel orientation is assumed for both, the gravity field,  $g$ , and the normal direction of the S/L interface (direction of solidification),  $n$ . In case A,  $n$  and  $g$  are antiparallel and in case B,  $n$  and  $g$  are parallel. The diffusion of Si into Al is represented by the white arrows: firstly, Si diffusion from the Al-Si melt into the Al matrix and secondly, lateral diffusion of Si into Al along the matrix, as marked by the dark-gray region within the Al layer. This region has been defined as the spread limit of Si in the screen-printing Al after cooling (see section 6.4). The epitaxial recrystallization of the melt during cooling is represented by the black arrows (with the normal  $n$ , as the direction of solidification).

### 6.6.2 Cross-sectional SEM Analysis

Figure 6.17 shows the SEM cross-sectional analysis. The eutectic layer and void formations were found in more than 20 samples, fired at different peak firing temperatures, for the two cases of firing presented in the model of Figure 6.16.

In case A, the normal direction of the solid/liquid interface,  $n$ , is in opposite direction to the gravity field orientation,  $g$  ( $n$  and  $g$  are antiparallel). The microstructure of the Al-Si eutectic is shown in Figure 6.17(a), (c). In the opposite case B,  $n$  and  $g$  are parallel. The microstructure of the Al-Si eutectic is presented in Figure 6.17(b), (d). In the Al-Si interface, Si-rich structures along the  $\langle 111 \rangle$  planes are still found after cooling, due to the phenomenon of extrusion which may diminish open-circuit voltage at the solar cell level [107].

Voids were found in every sample, which leads to the conclusion that the void

formation may be dependent on the Kirkendall effect, and less on the optimization of firing parameters. Nevertheless, firing the wafers, as in the case of A minimized the number of voids due to a partial fill of the cavity through the Al paste (the gravity may affect the crystalline morphology of some alloys [147]). It has been explained - based on the Kirkendall effect - that during fast sintering processes (fast cooling), the diffusion of Si leads to vacancies or interstitials formation across the dielectric window, which coalesce and nucleate, forming voids [142] instead of an eutectic layer.

Firing the samples with the front side down on the belt furnace should not present any risk of degradation of the emitter qualities.

As shown in Figure 6.17(a) and (c), a triangular profile with an angle of  $65^\circ$  is formed and marked (this angle repeats regularly in all samples analyzed). The eutectic in this case has only formed at the edges of the tilt angle. Inside the angle only Al paste in hypereutectic composition could be found. Thus, the softened Al paste (saturated by Si) drops facing downwards in case A. In some cases no eutectic was found and only the Al paste was filling the cavity. Hence, the voids may have been formed during the alloying process at peak temperature (see section 6.7).

The spherical liquid Al particles recrystallize within the tilt angle where less

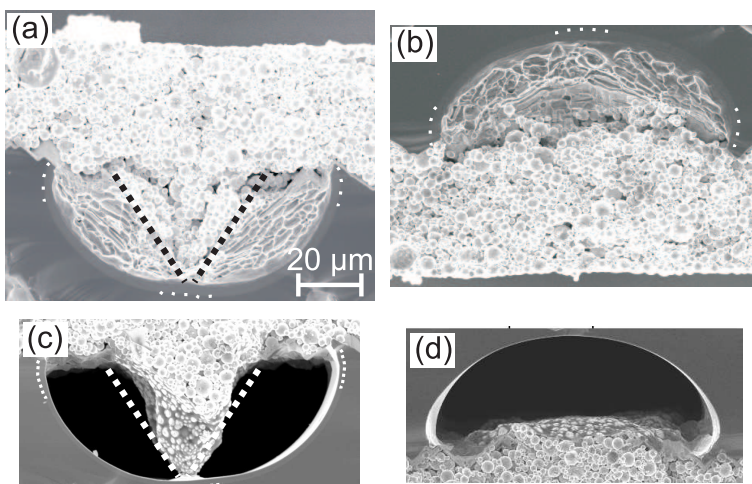


Figure 6.17: Cross section SEM micrographs showing the influence of the gravity on the solidification and microstructure of the Al-Si alloy. The local BSF is marked. On the left,  $n$  and  $g$  are antiparallel (case A): (a) completely filled Al-Si layer below the Al matrix, showing Al paste within the angle marked and eutectic composition on the rest; (c) partially filled void, presenting the same tilt angle than in (a), marked by the dotted line. On the right,  $n$  and  $g$  are parallel (case B): (b) completely formed eutectic layer below the Al matrix; (d) Void formed.

contact to the Si bulk is found than at the edges. The void formation process may be the same in both cases (A and B), however no paste fills the void in case B. In our case, melting and cooling could not be observed in real time and therefore it is extremely difficult to completely understand the process of void formation.

An important benefit of this phenomenon is that the Al paste can partially fill the voids, reducing their effect, improving the Al-Si contact, and increasing the formation of a BSF beneath the LCO. Because the solid Al spheres are visible within the void it can be concluded that the softened Al paste fills part of the void during cooling due to the impact of gravity.

### 6.6.3 Summary and Conclusions

It could be shown that the gravity field orientation has an important effect on the local Al-Si alloy morphology during sintering. The formation of voids can be completely or partially prevented when the gravity field orientation is antiparallel to the normal solidification direction of the solid/liquid phase. The formation of the local BSF is improved underneath the void. This approach may reduce series resistance losses normally found in these device structures. This discovery offers applications to the formation of local contacts for rear-passivated Si solar cells by local alloying of full-area, screen-printed Al pastes.

## 6.7 Understanding and Avoiding the Formation of Voids §

### Abstract

So far, several conclusions have been drawn within this study: the Al mass is responsible for mass transport during alloying; the diffusion of Si in Al within the Al matrix is limited by the contact spacing; two types of voids have been observed: voids with and without  $p^+$ -doped Si region (BSF) formation underneath. So far, it has been mentioned that the void formation may depend on the fast diffusion of Si in Al, the Kirkendall effect, the fast cooling, the contact spacing, lateral solidification within the Al. In the first part of the following section, the two types of voids formations are analyzed and a schematic model is presented to describe their formation. In the second part several issues to avoid void formation -as the presented in this work and in the literature- are reviewed.

### 6.7.1 Formation of Voids with and without Back Surface Field

So far, the formation of voids has been explained by the following effects:

- a. Due to the higher diffusivity of Si in Al than the diffusivity of Al in Si in Al-Si alloys, a high current of vacancies or interstitials across the dielectric window may occur (as explained by the Kirkendall effect). When increasing the firing temperature, the diffusivity of Si in Al increases and the process is accelerated.
- b. The concentration of Si in the Al matrix can be too low and the diffusion of Si back through the interface is not enough to form the eutectic and the BSF. This is mainly due to the spread of Si in Al due to large contact spacings.
- c. The volume of Al is too high and responsible for strong mass transport of the Al-Si melt during the alloying.
- d. The cooling process does not occur at equilibrium, as stated by the Al-Si phase diagram.

Figure 6.18 shows a simple scheme to explain the formation of voids with and without BSF, during the contact formation in narrow dielectric openings between screen-printed Al pastes to Si.

1. Reaching the peak temperature the Al-Si melt has deeply penetrated the interface in both cases. At this point no void formation is assumed.

---

§The main results of this section have been presented at the 3<sup>rd</sup> Workshop on Metallization for Crystalline Silicon Solar Cells, Charleroi (Belgium), 26.10.2011.

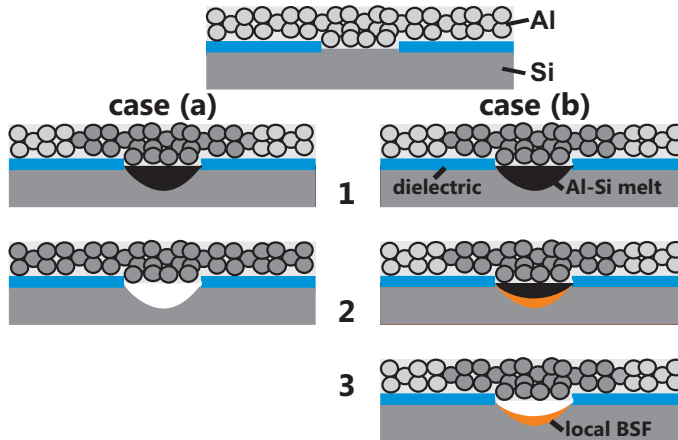


Figure 6.18: Simple scheme of void formation in the interface, underneath the Al layer. (1) The Al-Si melt increases in the Si bulk until the peak temperature is reached and Al saturated. (2) For case (a) the formation of a void appears before cooling, and therefore, no Al-Si melt is present during cooling and no epitaxially recrystallization of Si from the melt can occur, thus no BSF can be found. For case (b) the void is formed during cooling and a BSF is formed.

**2.** Case (a): Immediately afterwards, the void formation appears due to mass transport or Kirkendall effect, or both. During cooling no Al-Si melt is present and thus, no BSF can be formed. The remaining Si content in Al solidifies at the interface, above the void and underneath the Al layer, as shown in Figure 6.19(a).

**2.** Case (b): at this point the void has not yet formed. Thus, the recrystallization of Si from the Al-Si melt starts and a BSF is progressively formed (orange region in Figure 6.18).

**3.** Case (b): The voids appear during cooling too fast (faster than the solidification process: Si contained in Al does not reach the Al-Si interface to form the alloy). In this case the Kirkendall effect may also be present. The remaining Si content in Al solidifies at the interface, above the void and underneath the Al layer, as shown in Figure 6.19(b).

### 6.7.2 How to Reduce the Void Formation for Rear Passivated Solar Cells

The void formation in Al-Si alloys for rear passivated solar cells may be reduced by controlling the diffusion of Si into Al, by the following parameters:

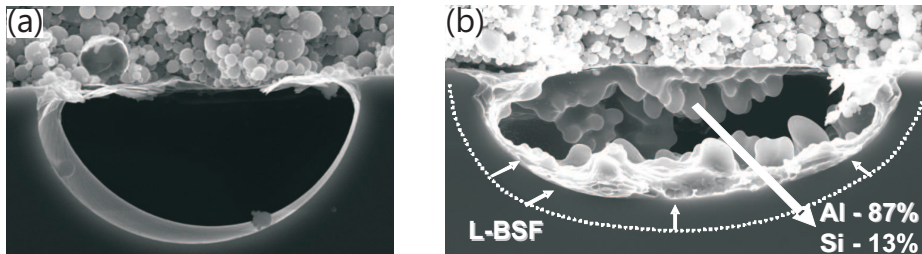


Figure 6.19: (a) In the case of a complete void formation, an alloy is found directly below the Al matrix. It means the void was formed before cooling started, and therefore Si solidified in the Al matrix. (b) In the second case, the local BSF started to grow and the Al-Si melt recrystallized. Probably due to cooling too fast the alloy was not completely formed. Afterwards the rest of Si solidified below the Al matrix where an hypereutectic concentration was found.

1. Due to the high diffusivity of Si in Al-Si alloys, an interesting approach is to add Si to Al paste before alloying. This has been mentioned recently by some authors [128, 140]. Another approach is to reduce the contact spacing as already shown within this chapter, where a thinner eutectic layer was found below the Al matrix and a well formed and deep local BSF was achieved, due to the reduced mass transport during heating. As shown in the literature a well formed local BSF is responsible for reduction of contact recombination [148].
2. Another approach is the development of new pastes to optimize Si-Al mass transfer, as already shown in the literature [149].
3. A well optimization of firing parameters together with new pastes may also help to achieve better results [150].
4. A novel approach is to sinter the solar cells with Al on top, in order to fill the voids with paste during the alloy.

### 6.7.3 Summary and Conclusions

Si diffusion into Al must be controlled in order to achieve best contact performance. Voids formation depends on many parameters such as diffusion of Si into Al, temperature, Kirkendall effect, concentration and distribution of Si in the Al layer, amount of Al and contact spacing. To avoid the phenomenon of void formation, many factors must be taken into account: reduction of the diffusivity of Si into Al by adding Si in the paste or by reduced contact spacings, and finally a tailored paste development is required to optimize Si-Al mass transfer.



## **Part III**

# **Analysis of Industrial Rear Passivated Solar Cells**



# PROCESSING OF REAR PASSIVATED SOLAR CELLS: ANALYSIS OF DEVICE STRUCTURES AND RESULTS

## Abstract

After the introduction of the rear passivated solar cell device (chapter 1) and the analysis of the local Al-Si contact formation (chapter 6), the goal of this chapter is to present the development of an industrially applicable process sequences for rear passivated solar cells on multicrystalline silicon substrates. The optimizations done in the previous chapter on the rear side contact formation between Al and Si will be applied in all the devices presented in this chapter. The improvement of the solar cell concepts and efficiency over the time span of this thesis is presented. Several passivation layers for the rear side are deposited and tested. Different reference structures were made in order to analyze the impact of several thermal budgets on the solar cell performance and their potential for increasing the efficiency of each device concept. The main difference between the batches is the preparation of the rear side before dielectric passivation. The single side polishing process was studied, in order to select the optimal etching procedure. Also, a chemical edge isolation approach is analyzed. A masking approach for protecting the front side emitter from the single side polishing is also presented. By the end of the chapter, the developed high efficiency solar cells on high quality mc-Si and Cz-Si material are presented.

## 7.1 Introduction

Many concepts for rear passivated solar cells have been developed throughout this thesis. In this chapter the main results, which may have the highest impact on the industrial production are summarized, and discussed. The main topic of rear passivated  $p$ -Si solar cell structures is the fabrication of a single side emitter\*.

Thus, the succession of rear side polishing and edge isolation is a critical step within the process. In order to further understand this topic, two studies are presented (on mc-Si), which are of paramount importance for the high efficiency solar cell presented here. Cz-Si material is incorporated in the batch, by the end of the chapter, in order to further analyze the impact of the approaches on high quality material.

The first study concentrates on the influence of an extra rear single side polishing step before phosphorus diffusion. The roughness of the rear side is shown to be related to the effective carrier lifetime of the bulk material. The influence of the roughness on the increase of the internal rear reflection and  $J_{SC}$  of the device will be shown in the spectral response of the solar cell. A chemical edge isolation step, however, is performed to achieve the single side emitter structure.

Therefore, a second process sequence is introduced which contains a masking of the front side phosphorus diffused emitter during the rear side polishing step, acting, at the same time, as a chemical edge isolation. Hence, the process sequence of the first study is simplified. Although the process cost are also reduced, this extra masking step might incorporate a new challenge for industrial application, which is the removal of the masking and of the phosphorous silicate glass (PSG), after single side polishing. After optimizing the process, the best concept is tested also on Cz-Si material, resulting in an innovative high efficiency solar cell concept.

## 7.2 Material

The different processing steps were carried out firstly on mc-Si feedstock with the properties shown in Table 7.1. Thin  $p$ -type boron doped large area mc-Si wafers were used. Special selection of the substrates from the middle part of silicon ingots delivered sister wafers for the process presented in this chapter.

---

\*The rear surface phosphorus doping should be removed before the deposition of a rear passivation layer, otherwise the  $p$ -type solar cell will be shunted.

Table 7.1: Substrates used for the studies as presented in this chapter.

Crystallinity	Type, dopant	Resistivity [ $\Omega\text{cm}$ ]	Thickness [ $\mu\text{m}$ ]	Size [ $\text{cm}^2$ ]	Quantity
mc-Si	<i>p</i> /Bor	$(2 \pm 1)$	$(180 \pm 10)$	243.36	200
Cz-Si	<i>p</i> /Bor	$(2 \pm 1)$	$(180 \pm 10)$	238.95	200

For mc-Si material a previous homogenization of the wafers is important due to the difference of quality within a mc-Si ingot. Thus, different process sequences are more comparable on homogenized material. By the end, high quality Cz-Si material is incorporated into the batch, in order to achieve high efficiency solar cells.

In this chapter three mc-Si material will be used.

### 7.3 Inline Phosphorous Gettering on As-Cut mc-Si

The potential of mc-Si material can be improved by removing metal impurities within the bulk from as-cut wafers by applying gettering techniques. The gettering qualities of a phosphorous inline diffusion are well known to improve the silicon bulk qualities [151]. The minority carrier diffusion length is increased by minimizing the number of recombination sites [105]. This is due to the accumulation of the contaminants in the highly doped regions, which are afterwards removed by chemical etching. The enhanced solar cells performance is mainly due to the strong increase of  $V_{OC}$ . In this work it is shown that up to 10 mV improvement is achieved with this approach, compared to mc-Si reference solar cells (see Figure 7.6).

The incorporation of an extra as-cut pregettering step in the production of mc-Si solar cells is not requested by the industry, because of its slow processing in the inline machine. It was used in this work, however, to maximize the available material quality.

A cleaning step is needed before the inline process, performed by low concentrated KOH at room temperature for 3 min. The saw damage remains on the surface after the short and cold cleaning. The metal residuals are removed by HCl/HF cleaning until a hydrophobic surface is achieved. The phosphorous pregettering takes place in a Tecnofimes inline furnace at 890 °C for 20 minutes.

## 7.4 Surface Roughness of Polished mc-Si Surfaces<sup>†</sup>

The improvement of polishing techniques for increasing surface quality is still a goal in the industry. It has been shown that the surface roughness highly influences the device qualities [152]. Lower costs in the industry line require more efficient processes which imply the use of thinner materials and rear side passivation techniques [11]. Furthermore, special requirements on surface treatment are also necessary, in order to further increase the light trapping [153, 154]. For this propose the surface is normally textured on the front side, randomizing the internal light reflection and increasing the internal front reflection [57]. By chemically polishing the rear side the surface qualities for dielectric layer deposition is enhanced, by minimizing surface recombination velocity [155], and increasing the internal rear reflection. The main results of the work conducted by the experts at the ISC-Konstanz on chemical etching of silicon surfaces are presented in this section. The aim of this work is to compare (on mc-Si) the alkaline with the acid polishing using roughness characterization.

This work has been performed on neighboring mc-Si wafers, which where split into two groups. The first group receives an isotropic texture (HF-HNO<sub>3</sub>) on both sides, and the second group material is left as-cut (saw damage remains on the surface). After HCl-HF cleaning, both groups receive a phosphorus inline gettering step. Each group is split again into two subgroups: one receives alkaline polishing (KOH, anisotropic etching) and the other acidic polishing (HF-HNO<sub>3</sub>, isotropic etching). The differences are shown by laser scanning microscopy analysis presented in Figure 7.1(a). The results in terms of reflectivity are presented in the next section. The influence of the etching depth,  $d$ , is analyzed on three grains of the mc-Si material, varying the etching time in order to achieve a depth range from  $d$  to  $3d$ . The lifetime of the samples is also characterized. For this purpose, the surfaces are specially cleaned and both sides passivated.

The lifetime is measured (after firing the samples under standard temperature profiles) by the quasi-steady-state photoconductance (QSSPC) technique introduced by Sinton (see reference [156]). This is a well-known technique to characterize surface passivation, by determining the bulk minority carrier lifetime in semiconductors, and also allows to predict the open-circuit voltage of solar cell before metallization (an important parameter for characterizing solar cells).

---

<sup>†</sup>Results reprinted with authorization of Dr. E. Wefringhaus, ISC-Konstanz e.V., and Dr. G. Schubert, Sunways AG.

## Characterization and Discussion of the Results

A strong parameter to characterize the roughness of a polished surface is the surfaces area ratio  $S_{dr}$ , also known as SDR roughness parameter, which expresses the increment of the interfacial surface area relative to the area of the projected (flat)  $xy$ -plane [157].

This parameter reflects slope gradients and its calculation is based on local  $z$ -slopes. The increase of  $S_{dr}$  means an increase of the roughness of the treated surface. Thus, a perfect polished surface (totally flat) has a surface area ratio,  $S_{dr} = 0$ , where the surface area and  $xy$ -plane are the same.

One might expect that the surface roughness should decrease with the chemical etching depth. However, the etching process strongly depends on the surface

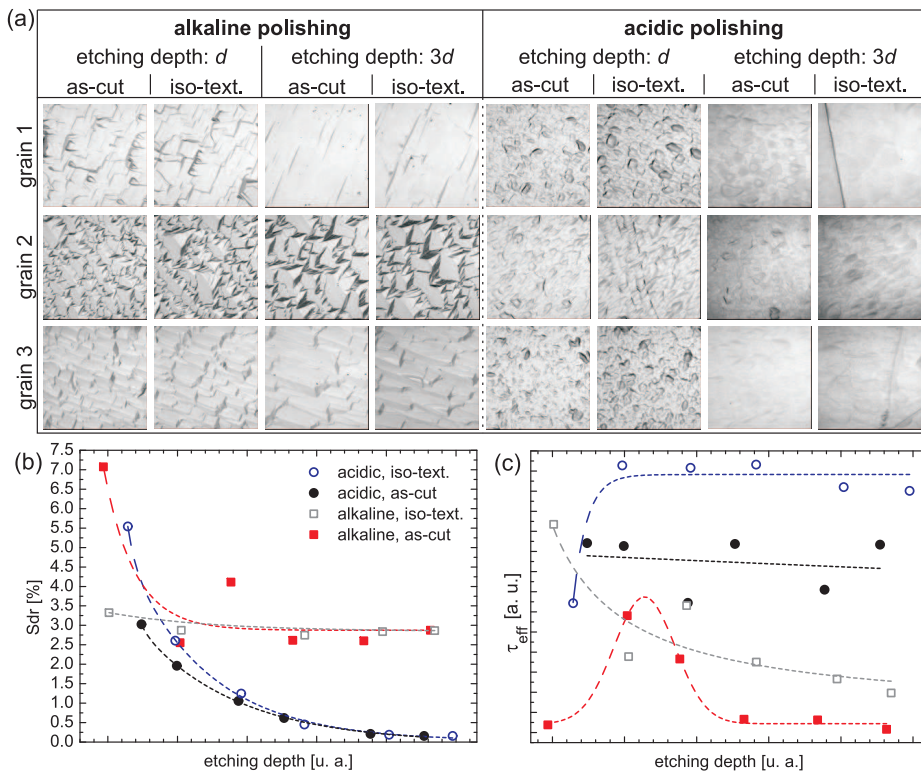


Figure 7.1: Study on the roughness of polished mc-Si substrates after two chemical approaches on as-cut and isotropic textured surfaces, for two etching depths. (a) Laser Scanning microscopy pictures of three crystal grains are chosen for each case. The etching time is varied, in order to achieve an etching depth range from  $d$  to  $3d$ . (b) The roughness analysis through the parameter  $S_{dr}$  shows the best results for acidic polishing. (c) The lifetime results show improvement after acidic polishing. Due to the removal of impurities by isotropic texturing, these samples represent the highest lifetime.

crystal orientation. As shown in Figure 7.1(b), the surface roughness steadily decreases with the etching depth for those samples treated with chemical acidic polishing, as this process is independent on the preceding state of the mc-Si surface (as-cut or isotropic textured). In a few minutes time, the acidic polishing easily achieves the minimum roughness  $S_{dr} = 0$ , where all gradients in  $z$ -axis are equal [the surface is perfectly smooth as shown in Figure 7.1(a)].

For alkaline polishing the result is peculiar on mc-Si surfaces, where a further increase of etching depth shows no influence on the smoothness of the surface, resulting in a constant value for the roughness ( $S_{dr} = 3\%$ ). This is due to the unwanted steps and crevasses caused by alkaline solutions between the grains of mc-Si surfaces [25]. Therefore, acidic etching solutions are to be used when polishing mc-Si surfaces, in order to achieve a near perfect smooth surface. This conclusion is corroborated by the carrier lifetime, which rapidly increases when using isotropic textured surfaces after an acidic etching step, as shown in Figure 7.1(c). The alkaline solutions diminish the lifetime of mc-Si surfaces, which decreases further with increasing etching depth. As-cut samples are normally treated with alkaline solutions for removing saw damage, and Figure 7.1(c) shows an optimal etching depth for this purpose, after which the lifetime is not further increased.

## 7.5 Reflectivity of Studied Si Surfaces

The reflectivity was measured on different surfaces as shown in Figure 7.2 (all measurements under air). Cz-Si material was used for this purpose, generalizing the reflectivity for one crystal orientation. The reflectivity of intrinsic Si is presented first: the experimental data (polished Si) goes in line with the data of intrinsic Si. The total reflectivity of intrinsic Si shows its minimum at 0.33 at 960 nm. The theoretical data for the intrinsic Si obviously assumes a transparent ingot for large wavelengths ( $\lambda > 1000$  nm), where the improvement of the rear internal reflection is ignored, which is contrary to the experimental measurement. The improvement by texturing the surface is paramount: the reflection is decreased by 22 % from a reflectivity of 0.33 for intrinsic Si to a reflectivity of 0.10 for textured samples, at 960 nm. As shown in the same Figure, when polishing the rear side of a textured sample, the specular internal rear reflection for long wavelengths is increased (compare red circle with black square in Figure 7.2)<sup>‡</sup>.

<sup>‡</sup>Remember that the absorption of Si shows that, above 1000 nm, the rear side of a 150  $\mu\text{m}$  device can be characterized.

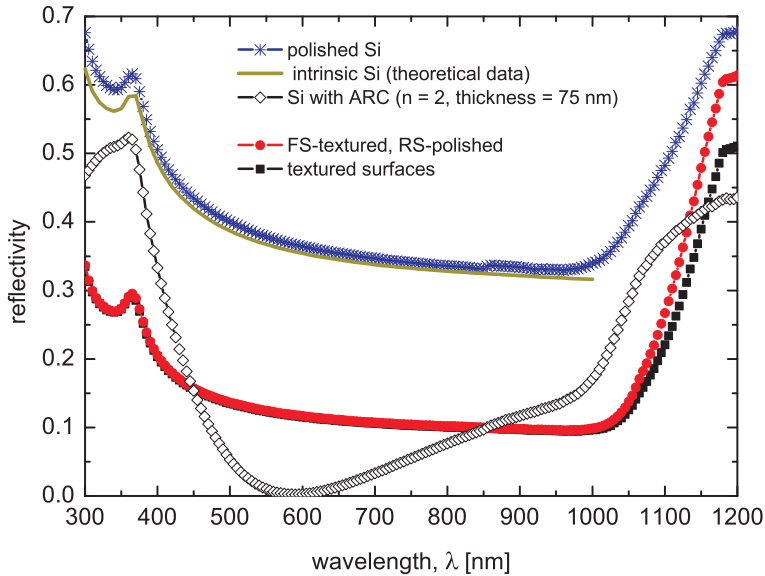


Figure 7.2: The reflectivity of incident light is measured as a function of wavelength measured on different surfaces, as studied throughout this thesis. The percentage of light reflected from bare Si is 40 % (as shown by experimental, total reflection of polished Si, and theoretical data of intrinsic Si). By texturing the surface the reflection is reduced down to 10 %. By polishing the rear surface of a textured sample, the specular rear internal reflection is increased for long wavelengths (red circle). The standard PECVD ARC shows a refractive index of 2 and a thickness of 75 nm to produce minimum reflection at 600 nm. All measurements performed under air. The theoretical data does not consider the internal reflection at the rear of the substrate above 1000 nm.

Table 7.2: The results on the total reflectivity of several surfaces, as shown in Fig 7.2, are compared to the internal reflectivity of a PERC solar cell and a Al-BSF reference solar cell.

Surface	Total front reflectivity	Rear internal reflectivity
Polished surface (planar)	0.33 at 946 nm	-
Textured surface	0.10 at 946 nm	-
Polished surfaces + optimized ARC	0.00 at 600 nm	
Al-BSF solar cell	0.00 at 600 nm	0.64
Rear passivated solar cell	0.00 at 600 nm	0.91

The internal reflectivity is further improved when the fully covered Al-BSF rear surface of a standard solar cell is replaced by a polished and passivated surface (see Table 7.2). A thin PECVD ARC with a refractive index of 2 and a thickness of 75 nm produce a reflectivity minimum at 600 nm for intrinsic Si (see section 2.5). In theory, the optimal light trapping in the solar cell device is achieved by a both sides textured and passivated Si material. In practice, however, better rear passivation qualities are achieved with polished Si surfaces than with textured.

## 7.6 Homogeneity of the Phosphorus Emitter Layer

The homogeneity of the phosphorus diffused layer was analyzed. This experiment is performed to gain knowledge of the emitter qualities which strongly influences the Ag-Si contact formation. For this propose the emitter sheet resistance ( $R_{SH}$ ) along the diffusion boat is tested on every 10 mc-Si wafers. The sheet resistance is measured on the upper part, middle part and lower part of each sample. The phosphorus diffusion is performed in a Centrotherm furnace using  $\text{POCl}_3$ . A standard recipe for a  $65 \Omega/\square$  phosphorus emitter is used for approximate 70 mc-Si wafers. The four point probe measurement of the emitter sheet resistance through the PSG is approximately  $\pm 5 \Omega/\square$  lower than the real value of the diffused layer.

Figure 7.3(a) shows the four point probe results of  $R_{SH}$  measured on the upper part (top), middle part (middle), and lower part (bottom) of each wafer (Figure 7.3(b)), from different positions of the diffusion boat (Figure 7.3(c)). An average of  $64 \Omega/\square$  for the sheet resistance is found without PSG removal. A large difference between the measurements performed on the upper part and on the lower part on the same wafer is found. This difference decreases from the first

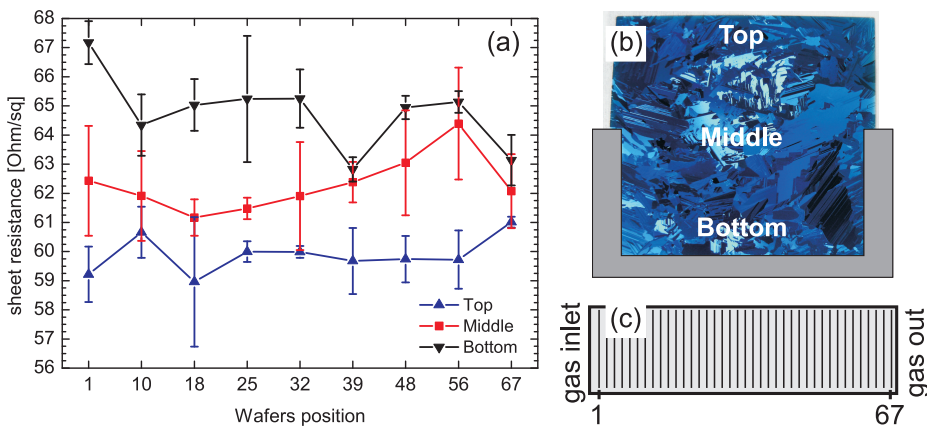


Figure 7.3: The influence of the boat position on the homogeneity of the phosphorous diffused emitter layer. (a) Sheet resistance measured by four point probe method through the boat of diffusion. The homogeneity of the emitter deposition strongly depends on the boat position, and varies within the wafer surface. (b) Schema of one wafer as located on the diffusion boat, showing the upper part (top), middle part (middle) and lower part (bottom) of the wafer, as used in the four point probe measurement. (c) Schematic of the wafer positions within the diffusion boat, showing the start position as the entrance into the diffusion oven, wafer 1, and the end position, wafer 67.<sup>¶</sup>

<sup>¶</sup>Result of 13 cells processed in the same batch.

wafer to the last one in almost 25 %.

The inhomogeneity of the sheet resistance is also remarkable along the boat. Absolute values vary from  $(64.79 \pm 1.52) \Omega/\square$  on the lower part,  $(62.31 \pm 1.51) \Omega/\square$  in the middle part, and  $(59.95 \pm 1.06) \Omega/\square$  on the upper part. A stronger diffusion is found on the upper part of the wafers than on the lower part, because the boat affects the flow of gas.

In conclusion, the sheet resistance of the deposited emitter used in this study might vary with a difference of  $\pm 5 \Omega/\square$  from the lower part to the upper part of the wafer. This difference needs to be taken into account when the contact formation of Ag pastes on the front side emitter is studied. It also influences the quality of the front side passivation, bulk gettering, and lifetime.

In order to overcome such inhomogeneities, another boat could be used or the wafers could be positioned more separately on the boat, allowing the gasses to reach the middle and lower part. This inhomogeneity could also be overcome by selective emitter concepts, using a second diffusion through oxide barriers with orientation dependent growth [158]. Nevertheless, a variation of  $\pm 5 \Omega/\square$  through the front surface of the wafer can be tolerated (within the tolerance of the device used).

## 7.7 Silver Pad Metallization for Module Assembly

In order to facilitate module assembly in industrial applications, solder pads have to be incorporated on the Al rear contact, parallel to the busbars on the front (see for instance references [159, 160]). For rear passivated solar cells, the pads should be screen printed directly on the passivation layer, and incorporated in the metallization process before the printing of the thick Al layer. The Al layer fully covers the entire rear surface except the Ag pads. The Ag pads should not fire through the dielectric layer, and therefore, the Ag paste should be low aggressive against the dielectric.

The goal of this section is to study the impact of the Ag pads on the rear surface passivation. An Ag paste is used which shows small tendency to fire through the rear PECVD stack. Three tests are performed: (a) the peel off test, (b) the impact of the Ag pads on the lifetime, and (c) the analysis of the penetration of the Ag pads into the dielectric. Due to the high density of the paste [Figure 7.4(left)] and maybe due to the homogeneous distribution of the glass content, the Ag pads remain on the dielectric layer, after sintering.

**a.** An important analysis for module assembly pads is the ribbon peel off test, where the sintered connection of the ribbon to the Ag pads are tested by pulling the ribbon in order to analyze its adhesion to the surface. The results of the peel off test are shown in Figure 7.4(right), for an Al-BSF reference cell (Ag pads on naked Si) and for a PERC cell (Ag pads on dielectric). The graph shows the bonding force of the Ag pads along the rear side of the wafer vs. the distance in cm. It is well-known from industrial application (see for instance reference [161]), that the accepted bonding force of solder pads should be higher than 1 N/mm. Thus, the bonding force of the Ag paste used here is more than acceptable for both solar cells, all along the length of the busbars. The following images in Figure 7.5(a) and (b) show the mechanical removal of the Ag pads as a result of the peel off test. The adhesion of the Ag ribbons is strong enough, so that the Ag pads cannot be peeled off from the Si surface during the test without destroying the wafer.

**b.** Figure 7.5(c) shows the carrier lifetime analysis of a both-sided passivated mc-Si wafer. On top of the dielectric three Ag busbar pads are screen printed and sintered (as shown by the white boxes). The average of the carrier lifetime over the complete wafer with Ag pads is approx.  $80 \mu\text{s}$ . Although the Ag pads are not clearly visible in the map shown in Figure 7.5(c), the average of the effective carrier lifetime measured directly where the Ag pads were located was about  $30\text{-}40 \mu\text{s}$ , and the result between the busbars for the average bulk lifetime was about  $100 \mu\text{s}$ . The incorporation of soldering pads on the rear side is investigated

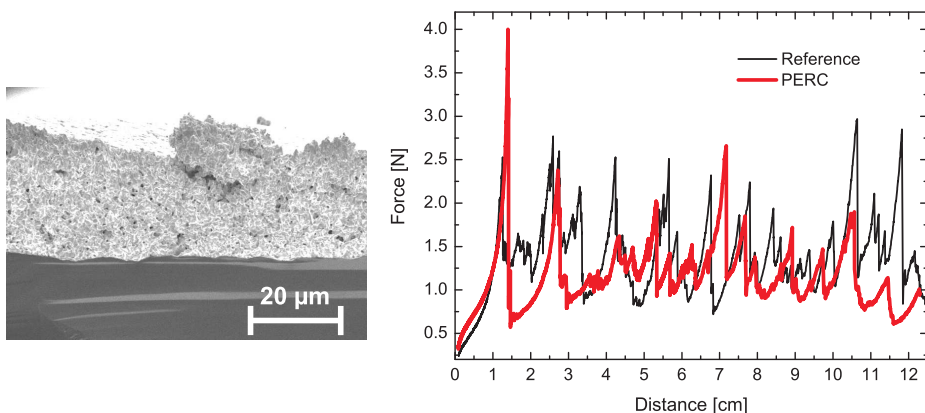


Figure 7.4: Left: Cross sectional SEM micrograph of an Ag finger printed and fired on a dielectric barrier. The Ag paste is more viscous than a standard silver paste, probably therefore its adhesion to the printed surface is strong enough without firing through. Right: Ribbon peel off test in [N] for a reference and a PERC cell.

in study 7.9.

c. Another test was the analysis of the penetration of the Ag pads into the dielectric. It is well-known that Ag does not react with dielectric layers. To make contact to the Si bulk possible, glass is incorporated in the Ag paste to open the dielectric during firing [37]. However, in the case of solder pads for rear passivated solar cells, the Ag paste must not be too aggressive against dielectrics. Therefore, further analysis of the alloy junction between the Ag paste and the sample surface was performed. To test how aggressive the Ag paste is, the elemental composition of the bulk alloy and on the surface was measured by EDS/EDX analysis after 8 min HF etching, as shown in Table 7.3. From literature it is well-known that glasses and oxides are easily removed by wet chemical etching with HF [118, 162]). HF does not react with Ag but etches the glass composition within the paste. Therefore, the Ag fingers will be easily separated from the surface<sup>||</sup>.

After an etching process with 5 % HF the Ag fingers were immediately separated from the dielectric layer (few seconds were needed). The glass contained in the Ag paste was etched off from the top of the dielectric (below the fingers) cutting the adhesive element of the Ag lines. After removing the Ag fingers, the dielectric was still under the Ag pads even after sintering.

The original atomic composition of the dielectric layer is shown in Table 7.3. Most of the dielectric is formed by Si and N. O is also found in the stack, due to a previous wet thermal oxidation. After HF etching a part of the N content of the

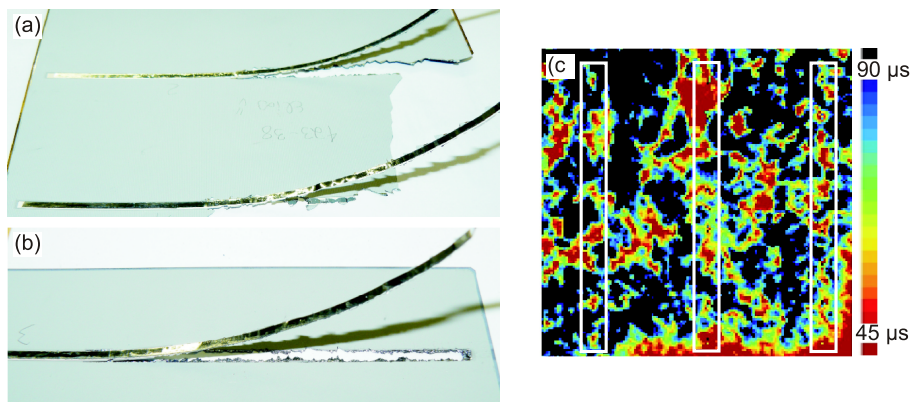


Figure 7.5: (a), (b) Ag pads after the peel off test performed to monitor the bonding force. (c) Effective carrier lifetime measurement on one both sides passivated mc-Si wafer, with 2 Ag pads busbars.

<sup>||</sup>To etch Ag, mixed acids or aqua regia types HF:HNO<sub>3</sub> are needed.

Table 7.3: EDS/EDX analysis of an screen printed Ag finger on a thick dielectric layer, after different HF etching times.

Surface and HF etching	Element	Atomic %
SiO <sub>2</sub> /SiN <sub>x</sub> without etching.	N	28.90
	O	4.25
	Si	66.85
Ag paste on bare Si after a few seconds HF etching.	Si	89.85
	Ag	10.15
Ag paste on SiO <sub>2</sub> /SiN <sub>x</sub> after 8 min HF etching.	N	11.18
	O	0.95
	Si	87.27
	Ag	0.60

dielectric layer has been removed. Thus, the SiN<sub>x</sub> layer in the stack thins down.

A reference sample was obtained by printing and sintering Ag fingers directly on bare Si. The EDS/EDX analysis shows that the content of Ag in Si is 10.15 %. The other sample was produced by sintering Ag on SiO<sub>2</sub>/SiN<sub>x</sub> and removing the finger by 8 min HF etching. Only a 0.6 % Ag content is found below the fingers compared to 10.15 % content on bare Si.

Concluding, this work showed that the used Ag paste is suitable for the application on thick dielectric layers (100 nm) for the base pads of the PERC structure.

## 7.8 Study 1: Single Side Polishing before $\text{POCl}_3$ Diffusion

### 7.8.1 Introduction

The first study concentrates on single side polishing before  $\text{POCl}_3$  diffusion and on an extra chemical edge isolation to remove the rear side phosphorus emitter\*\*.

First of all, the preparation of the samples is introduced and a table with the reference cells (Al-BSF solar cells) and the device structures (referring to PERC cells) is presented. The processes are evaluated by means of  $I$ - $V$  measurement of the solar cells. A light beam induced current analysis is performed to discriminate the influence of the processing steps from the dislocations typically found in mc-Si. By the end, the main conclusions of the impact of the different steps on bulk performance and the influence of an extra thermal oxidation step are given.

### 7.8.2 Preparation of the Samples

The process steps of rear passivated solar cells from mc-Si for study 1 are found in table 7.4. Three device structures incorporating rear passivation and local rear contacts are shown, as well as their respective reference structures. Each device plays an important role in understanding the strengths and weaknesses of each extra processing step. They are compared with the reference, in terms of possible industrial implementation. All devices are rear side polished before the diffusion step and afterwards, a chemical edge isolation is performed. The description of each solar cell structure is presented as follows:

- **Reference 1** presents the standard process of a solar cell with chemical edge isolation instead of laser edge isolation as presented in chapter 2. It is tested on material 1 (Ref. 1-1), on material 1 with an extra as-cut gettering step (Ref. 1-2), and on material 2 (Ref. 1-3).
- **Device 1** shows a rear passivated solar cell with an extra thermal oxidation step on both sides. The impact of the thermal oxidation on the emitter will be analyzed. Both, the front and rear passivation may be improved with this technique. This device is tested on material 1 (Dev. 1).
- **Device 2** shows a rear passivated solar cell with a thick PECVD layer as a barrier for the thermal oxidation (protecting the front side emitter). This

---

\*\*The wafers are not processed back to back in the diffusion.

Table 7.4: Processing steps for study 1 (single side polishing before  $\text{POCl}_3$  diffusion). Reference and rear passivated solar cells structures are studied on  $p$ -type mc-Si. For some solar cell structures different c-Si materials were used: material 1 (M1), and material 2 (M2).

Reference 1	Device 1	Device 2	Device 3	Reference 2
Ref. 1-1, M1 Ref. 1-2, M1 Ref. 1-3, M2	Dev. 1, M2	Dev. 2, M1	Dev. 3-1, M1 Dev. 3-2, M2	Ref. 2, M1
Isotropic texturing				
Rear side acidic polishing				
HCl, HF cleaning				
$\text{POCl}_3$ diffusion				
Chemical edge isolation				
PSG removal				
		FS PECVD	FS PECVD deposition 1	
IMEC cleaning				
Thermal oxidation				
FS PECVD deposition			FS PECVD deposition 2	
RS PECVD deposition				
RS dielectric ablation				Oxide removal
Ag, Al metallization and sintering				

technique was called SiNTO process by Wolf *et al.* [163], who recently published an analysis of the impact of the thermal oxidation on the nitride layer. Due to the front side barrier, the growth of the thin oxide layer occurs only at the rear side. This device is tested on material 1 (Dev. 2).

- **Device 3** presents a process similar to Device 2. In this case, two PECVD ARC coatings are deposited. A first layer is deposited before thermal oxidation as a thin barrier for the emitter. The cleaning step needed for the oxidation, which contains HF, etches down the dielectric layer a few nanometer as already studied in section 2.9.2. Immediately after the thermal oxidation (without cleaning) a second ARC layer is deposited on top of the first one, which may improve the hydrogen passivation qualities of the stack. The potential of two types of materials is analyzed in this device: material 1 (Dev. 3-1) and material 2 (Dev. 3-2).
- **Reference 2** presents a standard process which participates in the thermal oxidation process. It is tested with material 1 (Ref. 2). The oxide barrier at

Table 7.5:  $I$ - $V$  results of structures from study 1: the average and the best cell of each group are shown. See Figure 7.6

Structure	Material	$\eta$ [%] avg. /best	$V_{OC}$ [mV] avg. /best	$J_{SC}$ [mA/cm <sup>2</sup> ] avg. /best	FF [%] avg. /best
<b>Ref. 1-1</b>	M1	15.5 /15.6	598 /600.6	34.4 /34.6	75.1 /75.4
<b>Ref. 1-2</b>	M1	15.8 /16.0	614.4 /616.1	33.0 /33.3	77.9 /78.2
<b>Ref. 1-3</b>	M2	16.6 /16.8	625.4 /632.6	34.2 /34.5	77.9 /78.0
<b>Dev. 1</b>	M2	16.0 / <b>17.1</b>	625.9 / <b>633.5</b>	34.6 / <b>35.1</b>	71.8 /76.8
<b>Dev. 2</b>	M1	15.5 /15.9	614.9 /618.1	33.5 /33.8	75.3 /76.7
<b>Dev. 3-1</b>	M1	15.8 /16.0	616.9 /619.7	33.4 /33.7	76.9 /77.2
<b>Dev. 3-2</b>	M2	16.3 /16.7	623.2 /629.5	34.2 /34.7	73.5 /77.0
<b>Ref. 2</b>	M1	15.6 /15.6	611.1 /612.3	32.8 /32.9	77.6 /77.6

the rear side is etched off before the deposition of Al.

### 7.8.3 $I$ - $V$ Results and Discussions

The best results and average of the  $I$ - $V$  measurement are summarized in Table 7.5 and shown in a schematic form in Figure 7.6, for better understanding<sup>††</sup>.

#### Reference Solar Cells

The results of Al-BSF reference cells are separated from those of the rear passivated ones by a dotted line. The main results of the reference solar cells processed on material 1 (Ref. 1-1, Ref. 1-2, Ref. 2) and on material 2 (Ref. 1-3), are discussed as follows:

- The bulk quality of M1 was significantly enhanced after an as-cut gettering step, as shown by the  $V_{OC}$  gain of Ref. 1-2 up to 17 mV in average.
- The solar cell efficiency is increased up to 0.9 % absolute from Ref. 1-1 to Ref. 1-3. This is due to the better bulk properties of M2 compared to M1, as suggested by the increase in  $V_{OC}$  up to 28 mV on average.
- The thermal oxidation may be a critical issue on this type of materials. Ref. 2 (M1) participated in the thermal oxidation and shows no efficiency gain but a  $V_{OC}$  gain up to 12 mV compared to Ref. 1-1 (M1). In the case of Ref. 2, an important topic is the poor removal of the rear side oxidation layer by an

<sup>††</sup>The box plot is useful for descriptive statistics, showing the numerical data with the minimum, lower quartile, median, upper quartile, and maximum.

etching step, restricting the optical properties of the fully covered rear side Al-BSF (shown by the losses in  $J_{SC}$ ).

- Fill factors up to 78 % are achieved for reference cells due to the improvement of Ag pastes and the screen printing procedure.

Concluding, the potential of increasing the solar cell efficiency was strongly enhanced by the use of material with higher bulk qualities, more than that by improving the process sequence.

### Rear Passivated Devices

The main results of the rear passivated solar cells processed on material 1 (Dev. 2, Dev. 3-1) and on material 2 (Dev. 1, Dev. 3-2), are discussed as follows:

- **Material 1, Dev. 2 vs Dev. 3-1.** The bulk material M1 shows an efficiency limit of 15.8 % for both concepts. This is the same limit for the Al-BSF reference cells (Ref. 1-2) on the same material. The quality of the material is of paramount importance for further enhancement of the solar cell efficiency.

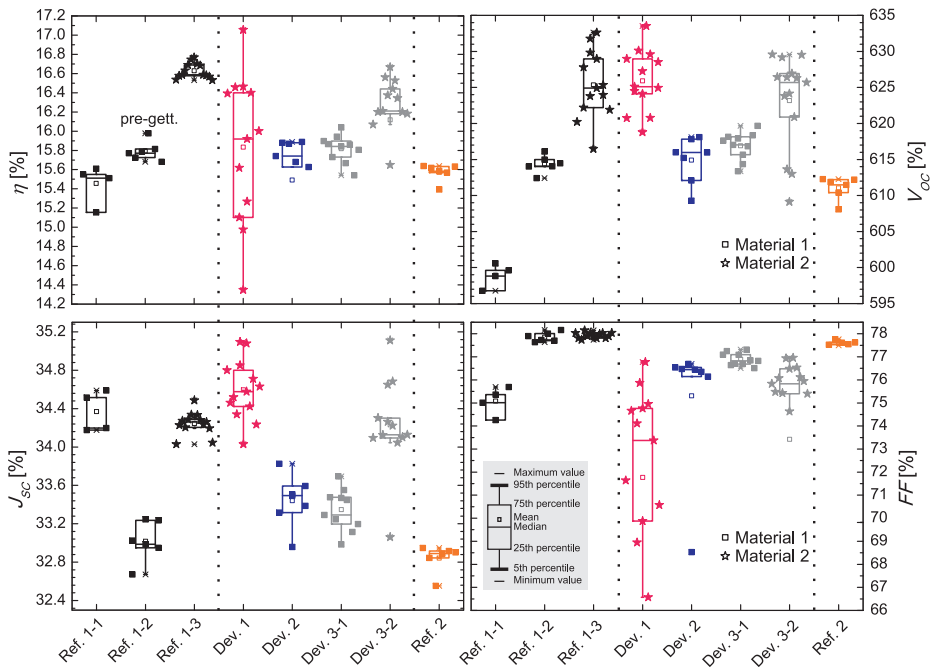


Figure 7.6:  $I$ - $V$  results of study 1. On the left-hand side and on the right-hand side the  $I$ - $V$  parameters are shown. On the bottom, each structure name is listed. The reference structures are separated by dotted lines. The different materials used are also shown. The structures are described in Table 7.5.

It seems that the properties of the  $\text{SiN}_x$  layer are diminished by a thermal budget, and that a second deposition after the oxidation may improve its qualities. This difference, however, is not clear with M1.

- **Material 2, Dev. 1 vs Dev. 3-2.** Although the incorporation of a PECVD barrier on the front side to protect the emitter from the thermal oxidation means an extra processing step, nevertheless, a more homogeneous process is achieved, as shown by Dev. 3-2 compared to Dev. 1. Both structures, Dev. 1 and Dev. 3-2, show the highest  $J_{SC}$  and  $V_{OC}$  results, with promising high FF. The properties of M2 are beyond the potential limit of M1. Nevertheless, no large improvement is found compared to the reference Ref. 1-3 on the same material.
- **Record cell of Dev. 1.** Although a remarkable inhomogeneity in terms of the efficiency is found within the process of Dev. 1, a high efficiency up to 17.1 % on rear passivated  $p$ -type mc-Si solar cell was achieved with this process, using standard screen printing metallization pastes and bulk material M2. This result presents the record of the whole batch of study 1, mainly due to the high  $J_{SC}$  up to  $35.1 \text{ mA/cm}^2$  and  $V_{OC}$  up to 633.5 mV. Nevertheless, a large variation in the FF result is remarkable, due to the difference within the metallization process and bulk material of the mc-Si ingot used (this difference is fully studied in section 7.9.4).
- The main result when comparing the references and the rear passivated devices is the improvement of  $J_{SC}$  up to  $0.4 \text{ mA/cm}^2$  for Dev. 1 compared with Ref. 1-3, mainly due to the thermal oxidation on both sides.
- The losses in FF for the rear passivated cells compared to the references are remarkable. This can be explained by the series resistance losses from the local contact at the rear side.

To draw a conclusion it has to be stated, that the best cell concept for rear passivated solar cells within this study is achieved by both processes: firstly, by a thermal oxidation on both sides of the material (directly on the front side emitter and on the polished rear surface); and secondly, by a deposition only on the rear side, protecting the emitter with a PECVD barrier and adding an extra front PECVD layer after thermal oxidation.

### 7.8.4 Analysis of Dislocations in mc-Si

It has been shown within this thesis, that the solar cell efficiency can be improved by processes which increase the quality of the bulk material. Nevertheless, it is well known that defects within the material diminish the performance of the solar cell device. Dislocations are crystallographic defects within the crystal structure such as grain boundaries.

This part concentrates on the analysis of dislocation within the mc-Si material used in study 1.

The mc-Si material used in study 1 is characterized by EL-Analysis and LBIC (see section 3.1.4). Figure 7.7 shows two pictures taken by EL-analysis, in high (a) and low current regime (b). The dislocations within the bulk material are electrically active when passing high current through the material, as shown by the dark lines visible.

In order to understand shunts resistance losses and to find the non-uniformities of the structure, LBIC mapping analysis is performed, obtaining the effective diffusion length for further analysis of rear side properties and contact formation. The light wavelengths used for carrier excitation are 405, 878, 948 and 980 nm. The LBIC mapping allows also to differentiate between those regions passivated by PECVD deposited layers and those regions passivated by alloyed Al-BSF.

Figure 7.8 shows our record cell from Dev. 1. The diffusion length ( $L$ ) is approx.  $L$  618  $\mu\text{m}$  on average. Higher values ( $L > 1000 \mu\text{m}$ ) are found near the lines with local  $p^+$ -doped Al. This result proves the good passivation qualities of the rear oxide nitride stack. On the LBIC map the many red and orange regions found in the mc-Si substrates represent areas of high dislocation density [125].

The inhomogeneity of the LBIC maps is remarkable on mc-Si material due to the difference in roughness and reflection on each crystal orientation. As

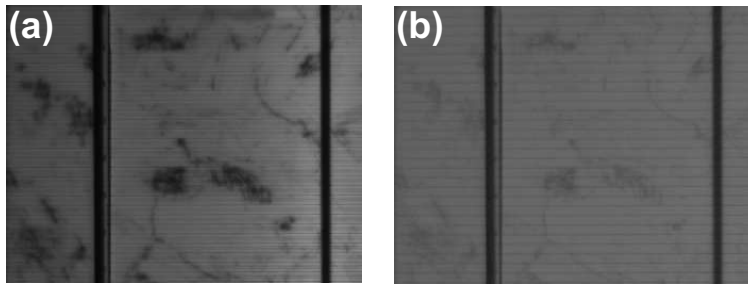


Figure 7.7: EL-analysis of dislocations in a mc-Si rear passivated solar cell, material 2. (a) high current. (b) low current.

shown in Figure 7.8 the streaks are caused by dislocation clusters [164], which are electrically active and clearly visible. The diffusion length,  $L$ , describes the recombination of minority carriers, which decreases exponentially with the distance. Many dislocation centres which represent recombination centers in the material are visible.

Some lines, however, might be associated with marks of saw damage removal, which remains after chemical polishing or texturing [60]. Also some recombination active grain boundaries (GB) are made visible with the LBIC approach [165]. The physics of GB have been further studied in the literature [166], showing that the transport properties are usually dominated by the formation of potential barriers at the GB, affecting the density of interface states, their trapping cross section and the relaxation time. Although the positive effect of the hydrogen passivation is completed after a thermal treatment of the samples, nevertheless, a few GB in the mc-Si material may still have a negative effect on the solar cell efficiency [61].

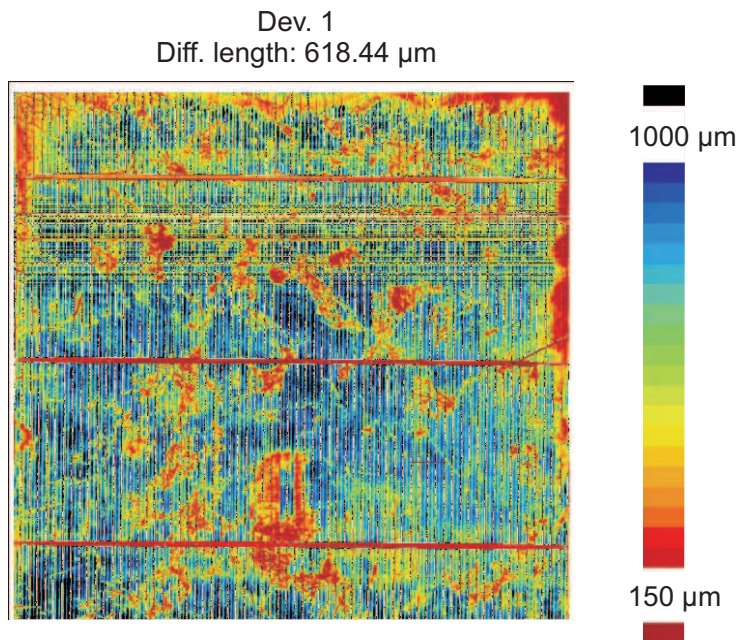


Figure 7.8: LBIC map at 980 nm of one solar cell of Dev. 1.

### 7.8.5 Summary and Conclusions

A promising average efficiency up to 16.8 % was achieved with Al-BSF solar cells on mc-Si material 2. The phosphorous gettering increases the bulk qualities of the mc-Si material. The record cell 17.1 % was achieved with oxide on both sides, emitter and rear, and obtained with mc-Si material 2. The rear was single side polished. Nevertheless, high inhomogeneities are found within this process, maybe due to the impact of the thermal oxidation on the mc-Si material qualities. The achievement of high efficiency on mc-Si material is not obvious and the PERC concepts still have a large potential and they need further optimization.

## 7.9 Study 2: Front Side Emitter Masking Approach

### 7.9.1 Introduction

Another process sequence for solar cells with polished and passivated rear side is presented and discussed. The front side phosphorus diffused layer (still with PSG) is masked by a special screen printable paste, in order to protect it from chemical etching.

This approach allows two processes at the same time: the polishing of the surface and the isolation of the rear side emitter. It has been shown in this thesis, that an acidic polishing of isotropic textured surface provides the highest effective carrier lifetime for mc-Si material (etching depth  $3d$ , see section 7.4). Thus, the smoothness of the surface is an important factor for the deposition of the dielectric layer. When etching the unprotected rear the phosphorous layer is removed, saving the chemical edge isolation as presented in section 7.8.

In the following section also a thermal oxidation is used. Although no modules were made, the impact of Ag pads for module assembly within the rear metallization layer on the cell efficiency is studied.

### 7.9.2 Preparation of the Samples

The processing of rear passivated solar cells from mc-Si for the study 2 is summarized in table 7.6. Two device structures with rear passivation and local rear contacts are shown, as well as their respective Al-BSF reference cells.

- **Reference 3** presents a reference for Device 4. It receives the same base treatment, with the exception of a fully covered Al rear side. The front side emitter is protected from a single side polishing by a masking approach. The rear side is fully covered by an Al rear side. Its performance is tested on two base materials: Ref. 3-1 (on material 2), and Ref. 3-2 (on material 3).
- **Device 4** presents a rear passivated solar cell with a thermal oxide nitride stack on both sides for passivation. Its performance is tested on two base materials: Dev. 4-1 on material 3, and Dev. 4-2 on material 2. **Dev. 4-1** was also tested on thinner material with a single side polishing depth of  $3d$ . However, due to the un-optimized firing parameters for thinner materials the performance was low, and, therefore, the results are not shown here (see the FF analysis in 7.9.4). For **Dev. 4-1** Ag pads were incorporated on the

Table 7.6: Processing steps for study 2 (front side emitter masking approach). Reference and rear passivated solar cells structures are studied on  $p$ -type mc-Si. For some solar cell structures different c-Si materials were used: material 2 (M2), and material 3 (M3).

Reference 3	Device 4	Reference 4
Ref. 3-1, M2 Ref. 3-2, M3	Dev. 4-1, M3 Dev. 4-2, M2	Ref. 4, M2
Texture ~ 10 $\mu\text{m}$		
HCl, HF cleaning		
$\text{POCl}_3$ diffusion		
FS mask deposition		
Rear side polishing ~ 10 $\mu\text{m}$		
FS mask removal		
PSG removal		
FS PECVD deposition		
IMEC cleaning		
Thermal oxidation		
FS PECVD deposition		
RS PECVD deposition		
RS dielectric ablation		
Ag, Al metallization and sintering		

Table 7.7:  $I$ - $V$  results of structures from study 2. See Figure 7.9

Structure	Material	$J_{SC}$ [ $\text{mA}/\text{cm}^2$ ] avg. /best	$V_{OC}$ [mV] avg. /best	FF [%] avg. /best	$\eta$ [%] avg. /best
<b>Ref. 3-1</b>	M2	33.6 /33.8	619.3 /619.9	78.0 /78.6	16.3 /16.5
<b>Ref. 3-2</b>	M3	34.5 /34.6	624.8 /626.4	77.7 /78.3	16.7 /17.0
<b>Dev. 4-1</b>	M3	33.5 /34.2	612.0 /619.5	77.4 /77.8	15.9 /16.5
<b>Dev. 4-2</b>	M2	33.7 /34.6	620.5 /627.7	78.1 /78.9	16.3 /17.0
<b>Ref. 4</b>	M2	34.5 /34.5	622.1 /625.0	76.8 /78.7	16.5 /17.0

rear for module assembly. As discussed in study 1, the Ag paste used for pads has no diminishing effect on the performance of the solar cell device.

- **Reference 4.** All structures are front side masked except Reference 4 which presents actually an industrial standard process for mc-Si.

### 7.9.3 *I-V* Measurements and Discussions

Averages and best results of the *I-V* measurement are summarized in Table 7.7 and shown in a schematic form in Figure 7.9, for better understanding.

The main results of the solar cells are discussed as follows:

#### Reference Solar Cells

The results of the Al-BSF reference cells are separated from those of the rear passivated ones by a dotted line. The main results of the reference solar cells processed on material 2 (Ref. 3-1, Ref. 4) and on material 3 (Ref. 3-2), are discussed as follows:

- The quality of material 3 and the higher potential for achieving high efficiency in Al-BSF structures is remarkable compared to material 2. This is clearly shown by the  $V_{OC}$  gain up to 5.5 mV on average for Ref. 3-2 compared to Ref. 3-1.
- A small difference is visible between the industrial reference cells (Ref. 4) and the reference cells with an extra masking and polishing step (Ref. 3-1)

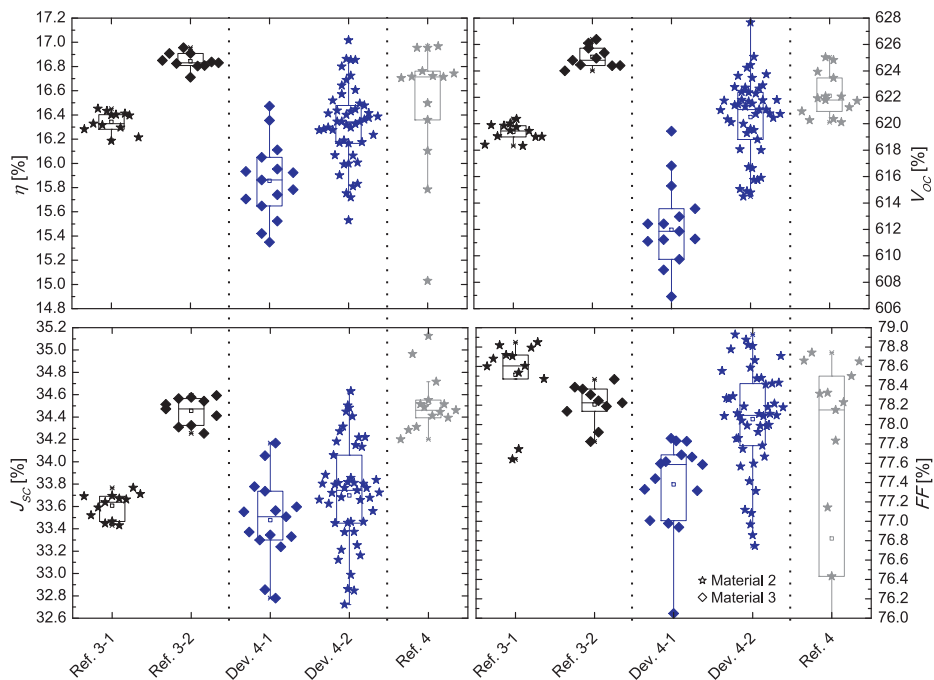


Figure 7.9: *I-V* results of the reference and rear passivated solar cell devices on *p*-type mc-Si. The reference structures are separated by dotted lines. Two materials were used. The structures are described in Table 7.7.

on material 2, mainly, due to a gain in  $J_{SC}$  and  $V_{OC}$ . Thus, the extra masking and polishing step does improve the Al-BSF solar cell concept of this study.

### Rear Passivated Devices

The main results of the rear passivated solar cells processed on material 2 (Dev. 4-2) and on material 3 (Dev. 4-1), are discussed as follows:

- In this study, a record efficiency up to 17.0 % was achieved by both, the Al-BSF solar cells of Ref. 3-2 and Ref. 4, and by the rear passivated solar cell of Dev. 4-2. Hence, no improvement of the solar cell performance by the rear passivated solar cell concept can be detected.
- The rear passivated solar cells do not show an increase in efficiency, when tested on material 3. On the contrary, better results are achieved with material 2, as shown by Dev. 4-2 compared to Dev. 4-1. Most likely the thermal oxidation had a strong impact on material 3, diminishing its material quality.
- Generally, in Device 4 a larger inhomogeneity of  $J_{SC}$  is visible, compared to Al-BSF structures. This may be due to the non-optimized rear surface passivation as a possible source of shunt at the rear side. Therefore, a study on the bias dependence for Dev. 4-1 will be performed in the following section, for a deeper understanding of the loss properties by shunt on the rear side passivation.
- A promising result is shown by Dev. 4-2 where Ag pads were incorporated on the rear. High efficiency and FF were achieved what shows that the impact of Ag pads on the rear dielectric surface does not diminish the performance of the solar cell structure.
- An extremely high variation in FF is found for Dev. 4-1, Dev. 4-2 and Ref. 4, however. The lowest FF results are found for Dev. 4-1, with an average of 77.4 %, compared to 78.1 % for Dev. 4-2. In the following section, a closer look at the FF variation for Dev. 4-1 will be taken, comparing it to the reference Ref. 3-2 which was processed in the same batch. It is extremely important to understand the losses in FF in this type of solar cells, where the potential to achieve high efficiency is not yet visible in study 2.

In conclusion, all devices produced on material 3 were limited by material quality. The Ag pads did not diminish the performance of the rear passivated solar cell. Masking the front side emitter before the rear side polishing is an

interesting approach to save the chemical edge isolation, but it did not show a gain in efficiency.

#### 7.9.4 Characterization of Solar Cells through FF, Printing Sequence, and Ag Paste Amount

In order to further understand the variation of FF as presented in study 2, a deeper analysis of the screen print sequence and paste amount is needed. For this analysis the Al-BSF structure Ref. 3-2 is compared with the PERC structure presented by Dev. 4-1, both processed in the same batch.

The single side polishing is tested on Dev. 4-1 for two etching depths,  $d$  and  $3d$  (see analysis presented in section 7.4). As shown in Figure 7.10, the group **Dev. 4-1**, polishing  $d$ , is thicker than the material used for **Dev. 4-1**, polishing  $3d$  (cells down to  $160\ \mu\text{m}$ ).

In Figure 7.10 the FF of the reference and PERC cells (left  $y$ -axis) and the amount of printed Ag (right  $y$ -axis) are plotted against the cleaning sequence.

The plotted data shows the cells from Ref. 3-2, from Dev. 4-1 with a single side polishing depth of  $d$ , and from Dev. 4-1 with a single side polishing depth

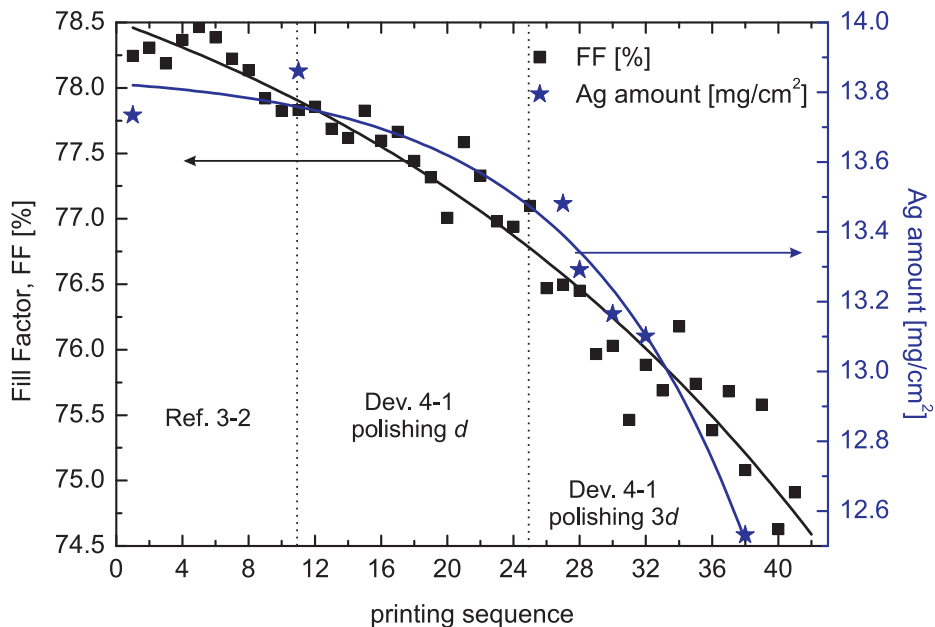


Figure 7.10: FF analysis of **Ref. 3-2** vs. **Dev. 4-1** (with two different polishing steps) depending on the Ag paste amount and screen printing sequence.

of  $3d$ . As mentioned in the last section, the  $I$ - $V$  characteristic of Dev. 4-1 with a polishing depth of  $3d$  were not shown in Figure 7.9.

The Ag paste is applied on a grid area of approx.  $15.8 \text{ cm}^{2\ddagger}$  formed by fine lines and three busbars. The amount of Ag paste printed on the wafer was measured during the process sequence, immediately after printing and before drying. The FF is measured after sintering the contacts in the firing furnace. The paste amount of printed Ag decreases with the printing sequence due to the non-optimal printing conditions, its variation along the printing is approx.  $1.5 \text{ mg/cm}^2$

The constant decrease of the FF value along the printing sequence is remarkable. The contact resistivity,  $\rho_c \sim 3 \text{ m}\Omega\text{cm}^2$ , is acceptable and its value remains constant along the printing sequence, as expected. The emitter is well contacted and no shunt is found in the thin phosphorous layer. The screen printed Al amount remains constant and close to  $10 \text{ mg/cm}^2$ .

The reduction of the volume of printed Ag by more than 11 % is high enough to influence the line resistance and to strongly decrease the FF of the device. Even higher FF losses are found on much thinner materials, as shown by Dev. 4-1, with an etching depth  $3d$ , mainly due to the non-optimized sintering parameters. Two issues reduce the performance of the device: first, the volume of Ag decreases due to non-optimal screen-printing, and second, the firing temperature are non-optimal for the thin material that is used.

In conclusion, to understand FF losses it is extremely necessary to analyze losses in line and contact resistance. Therefore, it is necessary to follow the screen-printing sequence to understand variations within the same batch during process. Furthermore it was shown that thinner material needs optimization of firing conditions.

### 7.9.5 Spectral Response Characterization

The spectral response of three cells is compared in the following section. All structures present similar front side emitter and passivation, and therefore, the spectral response is only shown for the infrared spectrum.

The record PERC solar cell from Dev. 1 ( $\eta = 17.1 \%$ ,  $J_{SC} = 35.1 \text{ mA/cm}^2$ , study 1, material 2, with polishing before diffusion) is compared with the best PERC solar cell from Dev. 4-1 ( $\eta = 16.5 \%$ ,  $J_{SC} = 34.2 \text{ mA/cm}^2$ , study 2, material 3, with polishing after diffusion), and with the best reference solar cell from Ref. 3-2 ( $\eta = 17.0 \%$ ,  $J_{SC} = 34.6 \text{ mA/cm}^2$ , study 2, material 3, with polishing after diffusion).

---

$\ddagger$ Front side screen.

Both PERC devices have the same thermal budget and passivation; a stack of thermal oxide and silicon nitride on both sides. The reference cell has also been single side polished (isolation of rear side emitter). Figure 7.11 shows the IQE response and reflection (R) in infrared spectra from 800 to 1200 nm, for the three structures analyzed under zero and 0.1 sun  $\S\S$ .

A small difference between the IQE response of both devices (Dev. 1 and Dev. 4-1) is due to a narrow difference in the rear internal reflection (difference on the optic of the dielectric layer). However, a  $J_{SC}$  gain up to 0.9 mA/cm<sup>2</sup> absolute is found (for Dev. 1 compared to Dev. 4-1), explained by the higher internal rear reflection.

Both rear passivated devices (Dev. 1 and Dev. 4-1), show a gain in the IQE response at large wavelengths compared to the reference Al-BSF solar cell

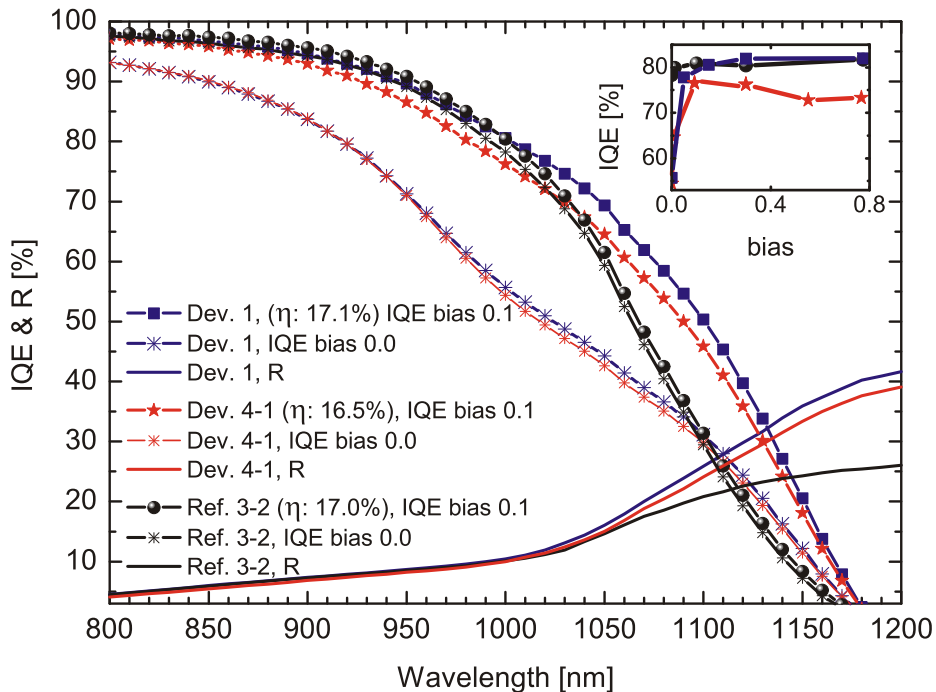


Figure 7.11: Spectral response (internal quantum efficiency, IQE, and reflection, R) analysis of an Al-BSF solar cell (Reference 3-2) vs. rear passivated devices (Device 1, Device 4-1). Top right corner: Bias dependence of the IQE at 1000 nm.

$\S\S$  The data was measured by a Spectral quantum efficiency and reflectance measurement device from PV-tools GmbH. This measurement is performed at 1000 nm, where EQE is sensitive to changes in diffusion length [55]. The measurement corresponds to the corrected (differential) EQE which is equal to the absolute EQE at 0.3 sun. In this case the results are shown for 0.1 suns for the corrected EQE.

(Ref. 3-2)<sup>¶¶</sup>.

The top right corner shows the IQE response at 1000 nm for the three structures plotted against the bias light<sup>\*\*\*</sup>. For the reference Al-BSF cell of Ref. 3-2 and for the PERC cell of Dev. 1 the EQE at 1000 nm is observed to be stable at the low bias light regime applied. Nevertheless, the PERC cell of Dev. 4-1 shows instability all over the bias light regime.

It is well known from literature [167] that SiN<sub>x</sub> applied directly on *p*-type surfaces causes shunting of the cell due to the inversion layer induced at the rear surface [167]. In the same paper it has been mentioned that the shunting is visible when the EQE decreases in the long-wavelength regime under low bias illumination.

The PERC cell of Dev. 4-1 may be strongly affected by parasitic shunting at the rear (maybe due to the presence of a too thin oxide layer below the nitride).

The IQE response for both PERC cells at long wavelengths strongly depends on the bias light variation as compared to the Al-BSF. Accordingly, our devices show the behavior of inverse layer shunting. In other words, the rear side stack SiO<sub>2</sub>/SiN<sub>x</sub> still needs further improvement (optic and passivation).

The maximum IQE at 1000 nm reaches approx. 83 % for the record cell of Dev. 1. This value is not achieved with Dev. 4-1. This could be also due to the low quality of the rear surface passivation.

## 7.9.6 Summary and Conclusions

It is shown, that the rear surface coating improves the internal reflectivity of the rear side, compared to a standard fully covered Al area, increasing the density of charge carriers in the cell, resulting in a gain on  $J_{SC}$ . The acidic polishing is of paramount importance before the deposition of a dielectric layer for optimal smoothness of the surface and maximal lifetime achievements. Different structures have been studied. An extra thermal oxidation is highly applicable on thermally stable mc-Si material, with the result of an improved passivation of the front side emitter and rear surface. Furthermore, a front side masking approach shows an innovative approach for industrial implementation.

---

<sup>¶¶</sup>The internal reflection with a dielectric layer is approximately 91 % compared to 64 % with an Al-BSF layer [15]. Thus, the absorption by the Al-layer should be considered here.

<sup>\*\*\*</sup>At 1000 nm the absorption depth of light in the Si material bulk is deeper than 150 μm.

## 7.10 High Efficiency Industrial Solar Cell with PECVD-Based Rear Surface Passivation

### 7.10.1 Introduction

If a state-of-the art front side silicon nitride layer is applied to the rear side, an inversion layer is found to diminish the rear side performance due to a highly positive fixed charge, increasing shunting on the rear [167, 168]. The most common solution to avoid the parasitic charge is the incorporation of a thin thermal oxide layer below the silicon nitride (in the last section this approach did not work optimally and need further improvement).

In the present section an all PECVD-based rear surface passivation is incorporated on the rear of mc-Si and Cz-Si material, in order to further analyze its impact on solar cell level. This innovative and industrially applicable Si-based passivation layer deposited by PECVD was developed by ISC-Konstanz, and was used within this thesis with the goal of reaching higher efficiencies without the need of a thermal oxide layer.

The applied PECVD layer enables high passivation qualities for the undoped *p*-type rear surface of PERC solar cells. Efficiencies up to 19.0 % on Cz-Si substrate with an efficiency gain of up to 0.9 % absolute compared to the reference (full Al-BSF) has been achieved and will be discussed here. Parallel to that, efficiencies up to 17.2 % on mc-Si material are shown (comparable to the SiO<sub>2</sub>/SiN<sub>x</sub> stack as presented in the last section), with an efficiency gain up to 0.2 % absolute compared to the Al-BSF cell. Avoiding an extra thermal oxidation step with its afore mentioned drawbacks, the PERC process presented in this section might be completely feasible for industrial applications.

### 7.10.2 Preparation of the Samples

*P*-type mc-Si and Cz-Si wafers with base resistivities of 2 and 1 Ωcm, respectively, were used in this investigation. Figure 7.12(a) shows the flowchart of the solar cell process. Passivation on both sides is achieved using an industrial PECVD reactor. The contacts are screen printed on the front and rear, with local BSF formation. As shown by the flow chart, the process is similar to that of **Device 4** except for the thermal oxidation step. Both sides are passivated using an industrially accessible standard PECVD device. The rear side passivation layer has been optimized for undoped and polished *p*-Si surfaces and presents high applicability and reproducibility for PERC solar cell structures. The rear side

pattern (geometry and spacing), has been optimized throughout this thesis for best solar cell performance, minimizing series resistance and alloyed Al-Si area (see chapter 6).

The process requires just a few steps more than a state-of-the-art standard solar cell, of which all are industrially applicable. No extra and special equipment is needed (no thermal silicon dioxide or aluminum oxide were used).

### 7.10.3 Results and Discussions

Table 7.8 summarizes the  $I$ - $V$  results (average and best). The processing of the wafers is developed at a standard industrial level and no special equipment or processing was required for achieving these efficiencies. For our best mc-Si cell, an efficiency of 17.2 % was obtained on large area 156x156 mm<sup>2</sup>, with an efficiency gain of 0.2 % compared to the reference with fully Al-BSF covered rear side. The best cell on Cz-Si material exhibits efficiency as high as 19.0 %, an efficiency gain up to 0.9 % compared to the reference with fully Al-BSF covered rear side. On mc-Si material an average gain of 0.6 mA/cm<sup>2</sup> in  $J_{SC}$ , 2.3 mV in  $V_{OC}$ , and 0.2 % in  $\eta$  is achieved for the PERC cells, compared to the Al-BSF cell. On Cz-Si material, an average gain of 1.9 mA/cm<sup>2</sup> in  $J_{SC}$ , 5.7 mV in the open circuit voltage, and 0.9 % in  $\eta$  is achieved for the PERC cells. Due to the possible series resistance losses by different rear side structure, a gain in FF cannot be detected.

Using the QSSPC method on unmetallized substrate the implied open circuit

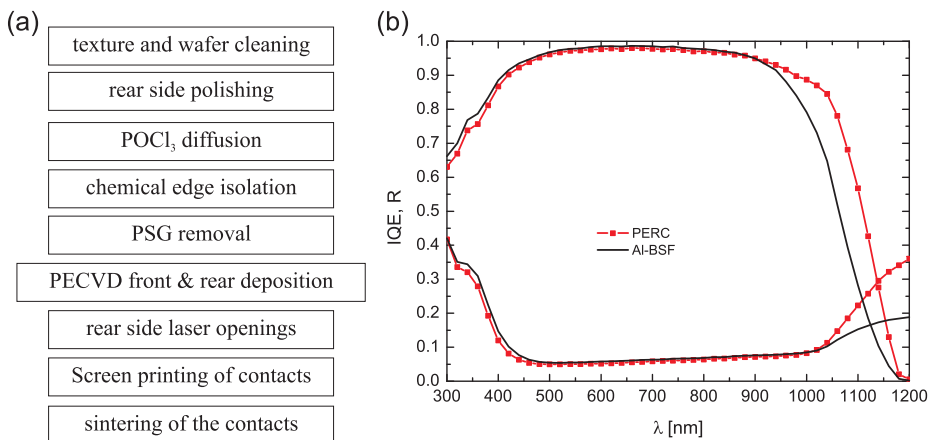


Figure 7.12: (a) Flowchart of the main solar cell process steps, using only industrially available equipment. (b) Spectral response and reflection response along the wavelength for the best Cz-Si PERC solar cell developed through this thesis vs. the Al-BSF reference.

Table 7.8: Comparison of the average and best solar cell parameters on 243.36 cm<sup>2</sup> c-Si substrate.

Rear surface passivation	Substrate	$J_{SC}$ [mA/cm <sup>2</sup> ] avg./best	$V_{OC}$ [mV] avg./best	FF [%] avg./best	$\eta$ [%] avg./best
PECVD	Cz-Si	37.7 /37.8	637.0 /637.5	79.0 /79.1	18.9 /19.0
	mc-Si	35.0 /35.2	625.9 /626.7	78.1 /78.3	17.1 /17.2
Al-BSF	Cz-Si	35.8 /36.0	631.3 /631.9	79.7 /79.9	18.0 /18.5
	mc-Si	34.4 /34.6	623.6 /625.1	78.9 /79.3	16.9 /17.2

voltages was determined to be 655 mV for mc-Si cells and 695 mV for Cz-Si cells, showing the high potential of the rear side passivation.

Figure 7.12(b) shows the spectral response of the best 19.0 % PERC solar cell with the novel PECVD rear side passivation vs. the standard fully covered Al-BSF. The better passivation quality of the rear side compared to the reference is clearly visible in the long wavelength regime (infrared response). Also, the reflection is low over a wide wavelength range which shows the high quality of the front side texturing. Nevertheless, the efficiency can be further improved by increasing the blue spectral response, with a better front side passivation and more shallow emitter, since the problem of contacting shallow emitters has recently been overcome by new silver pastes.

The rear side reflectivity for rear passivated cells is typically 90 %, compared to the effective rear surface reflectivity of a Al-BSF solar cell, determined to be approximately 70 %. The improved optical properties increase the  $J_{SC}$  values accordingly.

### 7.10.4 Electroluminescence Analysis

EL-analysis was performed to compare the reference Al-BSF solar cell with the high efficiency rear passivated solar cell. Figure 7.13 shows the EL-analysis for both cells. Although the results of FF and efficiency are promising, dark regions within the PERC structure are found. Many regions within both solar cells are quite bright, and for the PERC cell some regions are even more brighter than the reference cell, due to the rear surface passivation and smaller contacted area. Some dark regions are remarkable within the EL-images, as shown by the black arrows in Figure 7.13. After cross-sectional analysis by SEM micrographs of these regions we found that most of the dark regions are represented by void formations without BSF instead of an eutectic alloy with BSF, as already discussed in last chapter. In fact, the Al-BSF has been widely demonstrated to reduce the

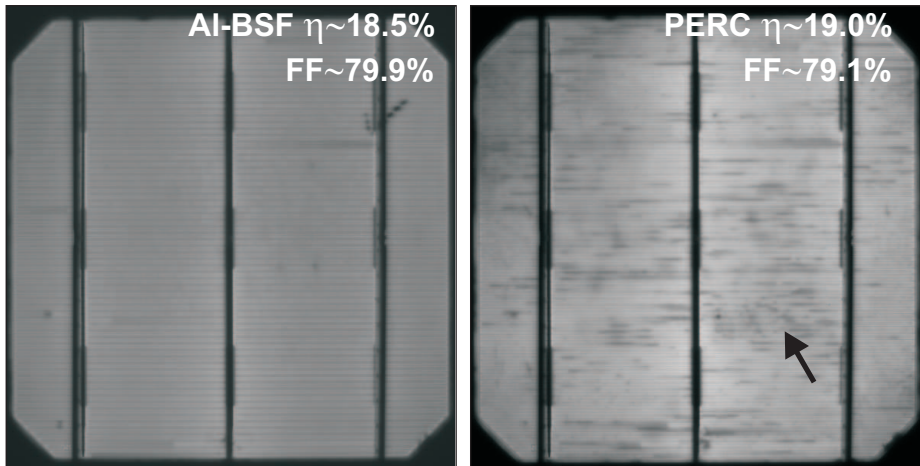


Figure 7.13: EL-analysis of an Al-BSF and a PERC solar cells. The black arrow shows some of the dark regions presented during EL-analysis. These regions are mostly presented by voids instead of eutectic and BSF formation.

recombination at the rear of the solar cell. This result corroborates the hypothesis, that void formations are source of both, series resistance losses and centers of bad passivation (see chapter 6).

### 7.10.5 Summary and Conclusions

A simple low cost industrial process has been proposed for the fabrication of PERC solar cells for industrial application leading to high efficiency gains. PECVD deposition has been used as an alternative to thermal oxidation, saving processing costs and minimizing the thermal budget for the substrate (critical for mc-Si). The use of industrial PECVD equipment and standard screen printing shows the high potential of the concept to be incorporated into existing industrial cell lines. Moreover, as shown by the implied  $V_{OC}$  and spectral response, a further optimization of the front side emitter and metallization reducing emitter recombination and improving the diffusion length in mc-Si wafers may significantly increase the blue response of the solar cell device, where an efficiency up to 19.5 % can be expected. The present results also corroborate the good performance of the local Al-Si contact formation on the rear of the device, as analyzed in chapter 6. This is a significant step for industrial production of *p*-type advanced mc-Si, or Cz-Si rear passivated solar cells. The high potential of the PERC structure to be incorporated in the industry should ideally be based on industrially available processes.

## THESIS SUMMARY AND OUTLOOK

The research presented in this thesis addresses several insights into a deeper understanding of local contact formation during sintering of screen printed aluminum pastes with *p*-type silicon substrates. The physical observations showed that the contact resistivity of thin aluminum fingers depends on the dielectric opening areas where the Al-Si alloy is formed. Contrary to our expectations, the shallowest dielectric barrier opening resulted in the lowest contact resistivity of  $8 \text{ m}\Omega\text{cm}^2$ . On solar cell level a reduction of the contact area for screen printed Al fingers led to a reduction of the series resistance losses. At the same time, narrow Al-Si alloy formations minimized the impact of the openings on the optical properties of the rear side, increasing the dielectric passivated area below the contacts, and reducing the short circuit current and open circuit voltage losses.

The study presented in this thesis contributed to the understanding of diffusion of silicon through dielectric openings into the aluminum thick layer. For the first time, the spread limit of silicon in a screen printed aluminum layer was determined, and it was found that its value on each side of the dielectric opening does not depend on the contact area size but rather on the firing temperature. The spread limit of silicon in the screen printed thick aluminum layer is thus predicted to 75, 225, and 375  $\mu\text{m}$  for temperatures of 750, 850, and 950  $^{\circ}\text{C}$ , respectively. Additionally, the formation of voids instead of an Al-Si eutectic layer was explained by the Kirkendall effect (diffusivity of Si is higher than diffusivity of Al in Al-Si alloys), and also depends on the contact spacing, aluminum paste amount, temperature and cooling rate, factors that limit the diffusion of silicon during the sintering in this type of alloys.

It was also shown that gravity may strongly affect the local Al-Si eutectic morphology. The presence of voids was partially avoided by changing the gravity field orientation parallel to the normal solidification direction of the solid/liquid phase (*i.e.* by sintering the solar cells front side down). Several suggestions to minimize the presence of voids in the alloy were presented which should lead to a better formation of the local back surface field (extremely important for the solar cell performance). The results presented may be applied to the sintering of screen-printed pastes on solar cells in order to reduce series resistance losses due to a better local back surface field formation. Thus, the understanding and avoiding of the well known problem of voids was thoroughly analyzed.

Furthermore, simple low cost industrial processes with optimized rear local

contacts for the fabrication of PERC solar cells for industrial application were presented, leading to high efficiency gains. By the end of the thesis, an all PECVD-based rear surface passivation was used as an alternative to thermal oxidation, saving processing costs and minimizing the thermal budget for the multicrystalline substrate.

The use of industrial accessible equipment and processing, such as screen printing for metallization and PECVD deposition for antireflection coatings, showed the high potential of those concepts to be incorporated into existing industrial cell lines.

The results presented in the field of contact formation are supported by the high efficiency results that were achieved. This thesis presents advancement in applying the rear passivated solar cell concept in industrial production.

**Outlook:** The incorporation of a selective emitter concept, as presented in the beginning of this thesis, to improve the blue response of the front side of the solar cell together with the rear passivation and local contacts as deeply studied in the last chapters, results in an interesting device to study. It may show higher efficiency than state-of-the-art solar cell and a high potential to incorporate this concept into the industry.

## ZUSAMMENFASSUNG (GERMAN SUMMARY)

Die hier dargestellte Forschung gibt einen Einblick in die lokale Kontaktbildungen, die während des Sinterns von siebgedruckten Aluminium Pasten mit *p*-Typ-Silizium-Substraten entsteht, und dient zum besseren Verständnis derselbigen.

Auf der Ebene der Solarzelle ist festzustellen, dass Füllfaktor-Verluste durch eine Reduzierung der Kontaktfläche der siebgedruckten Aluminium-Finger mit dem darunter liegenden Silizium verringert werden können (Kontaktfläche < metallisierte Fläche). Hinsichtlich der optischen Eigenschaften der Rückseite der Solarzelle ist festzustellen, dass die schmalen Al-Si-Legierungsbildungen zu einer Vergrößerung des dielektrisch passivierten Bereichs unterhalb der Kontakte und damit zu einer Verringerung der Verluste bei Kurzschlussstrom und Leerlaufspannung beitragen.

Diese Dissertation leistet einen Beitrag zum Verständnis der Diffusion von Silizium aus lokalen Kontaktöffnungen in die Aluminiumkontaktschicht. Es wurde zum ersten Mal die begrenzte Verbreitung von Silizium in einer siebgedruckten Aluminiumschicht gemessen. Darüber hinaus wurde festgestellt, dass die Siliziumkonzentration auf beiden Seiten der Kontaktöffnungen nicht von der Kontaktfläche abhängig ist, sondern nur von der Feuertemperatur. Die Verteilungsbreite von Silizium in der siebgedruckten Aluminiumschicht kann somit vorausgesagt werden, und verändert sich entsprechend der Feuertemperatur in konstanten Werten von 75, 225, und 375  $\mu\text{m}$  für 750, 850 und 950  $^{\circ}\text{C}$ .

Die Entstehung von Hohlräumen anstelle von Al-Si Eutektikumschichten wurde anhand des Kirkendall-Effekts erklärt. Es wurde auch gezeigt, dass die Ausrichtung des Gravitationsfeldes einen starken Einfluss auf die lokale Al-Si Eutektikum Morphologie hat. Das Auftreten von Hohlräumen wurde teilweise durch eine Änderung der Ausrichtung des Gravitätfeldes parallel zur normalen Kristallisierungsrichtung der fest/flüssig-Phase verhindert. Diese Herangehensweise führte zu einer verbesserten Bildung des (lokalen) BSF, das für die Leistung der Solarzelle extrem wichtig ist.

Durch Anwendung des hier gewonnen Wissens und bei entsprechender Reduzierung der durch Hohlräume verursachten Probleme, könnten die Serienwiderstandsverluste durch bessere lokale Kontakt-Bildung verringert werden. Außerdem wurden einfache und kostengünstige industrielle Prozesse zur Herstellung von PERC Solarzellen vorgeschlagen, die zu einer industriellen Anwendung von hocheffizienten Solarzellen führen sollen.

Am Ende der Arbeit wurde eine PECVD-basierte Rückseitenpassivierung als Alternative zur thermischen Oxidation eingesetzt, die Prozesskosten sparen kann, und das thermische Budget für multikristalline Silizium-Substrate reduziert.

Die Verwendung einer industriell zugänglichen Ausstattung und Verarbeitung, wie Siebdruck für die Metallisierung und PECVD für die Abscheidung von Antireflexschichten, zeigten das hohe Potential dieser Konzepte, die zweifelsohne in bestehende industrielle Zelllinien integriert werden können. Die Ergebnisse der vorliegenden Arbeiten können angewendet werden, um den Wirkungsgrad von industriell produzierten Solarzellen zu erhöhen.

Die hohen erzielten Wirkungsgrade bestätigen die Anwendbarkeit der Forschungsergebnisse für den Bereich der Kontaktbildung. Die vorliegende Arbeit zeigt, wie das Konzept der auf der Rückseite passivierten Solarzellen verbessert und dementsprechend in der industriellen Produktion verwendet werden kann.

## BIBLIOGRAPHY

- [1] D. S. Jenkinson, D. E. Adams, and A. Wild, *Model estimates of CO<sub>2</sub> emissions from soil in response to global warming*, *Nature* **351**, 304 (1991).
- [2] S. Rahmstorf, and H. J. Schellnhuber, *Der Klimawandel. Diagnose, Prognose, Therapie*, C. H. Beck, München (2006).
- [3] T. L. Delworth and T. R. Knutson, *Simulation of Early 20th Century Global Warming*, *Science* **287**, 2246 (2000).
- [4] T. L. Root *et al.*, *Fingerprints of global warming on wild animals and plants*, *Nature* **421**, 57 (2003).
- [5] R. A. Kerr, *Global Warming Is Changing the World*, *Science* **316**, 188 (2007).
- [6] L. Elliott, *Environmental Conflict: Reviewing the Arguments*, *The Journal of Environment and Development* **5**, 149 (1996).
- [7] S. R. Bull, *Renewable energy today and tomorrow*, in *Proc. IEEE* **89**, 1216 (2001).
- [8] I. Dincer, *Renewable energy and sustainable development: a crucial review*, *Renew. Sustain. Energ. Rev.* **4**, 157 (2000).
- [9] S. Solomon S, J. S. Daniel, T. J. Sanford, D. M. Murphy, G. K. Plattner, R. Knutti, and P. Friedlingstein, *Persistence of climate changes due to a range of greenhouse gases*, in *Proc. Natl. Acad. Sci, USA.* **107**, 18354 (2010).
- [10] A. Ortega, R. Escobar, S. Colle, and S. L. de Abreu, *The state of solar energy resource assessment in Chile*, *Renewable Energy* **35**, 2514 (2010).
- [11] S. W. Glunz, *New concepts for high-efficiency silicon solar cells*, *Sol. Energy Mater. Sol. Cells* **90**, 3276 (2006).
- [12] A. W. Blakers, A. Wang, A. M. Milne, J. Zhao, and M. A. Green, *22.8% efficient silicon solar cell*, *Appl. Phys. Lett.* **55**, 1363 (1989).
- [13] G. Agostinelli, P. Choulat, and G. Beaucarne, *Rear surface passivation for industrial solar cells on thin substrates*, in *Proc. 4rd IEEE WCPEC, Waikoloa*, pp. 2-5 (2006).

- [14] G. Agostinelli, P. Choulat, H.F.W. Dekkers, S.D. Wolf, G. Beaucarne, *Screen printed large area crystalline silicon solar cells on thin substrates*, in Proc. 20th EUPVSEC, Barcelona, Spain, pp. 1-4 (2005).
- [15] P. Choulat, G. Agostinelli, F. Duerinckx, and G. Beaucarne, *Above 17% industrial type PERC Solar Cell on thin Multi-Crystalline Silicon Substrate*, in Proc. 22rd EUPVSEC, Milan, pp. 1011-1014 (2007).
- [16] S. H. Lee, *Cost effective process for high-efficiency solar cells*, Solar Energy **83**, 1285 (2009).
- [17] G. Beaucarne, *et al.*, *Thin, thinner, thinnest: an evolutionary vision of crystalline si technology*, in Proc. 21st EUPVSEC, Dresden (2006).
- [18] D. Niinobe, H. Morikawa, S. Hiza, T. Sato, S. Matsuno, H. Fujioka, T. Katsura, T. Okamoto, S. Hamamoto, T. Ishihara, and S. Arimoto, *Large-size multi-crystalline silicon solar cells with honeycomb textured surface and point-contacted rear toward industrial production*, Sol. Energy Mater. Sol. Cells **95**, 49 (2011).
- [19] D. Y. Lee, H. H. Lee, J. Y. Ahn, H. J. Park, J. H. Kim, H. J. Kwon, and J. W. Jeong, *A new back surface passivation stack for thin crystalline silicon solar cells with screen-printed back contacts*, Sol. Energy Mater. Sol. Cells **95**, 26 (2010).
- [20] M. Hofmann, S. Janz, C. Schmidt, S. Kambor, D. Suwito, N. Kohn, J. Rentsch, R. Preu, and S. W. Glunz, *Recent developments in rear-surface passivation at Fraunhofer ISE*, Sol. Energy Mater. Sol. Cells **93**, 1074 (2009).
- [21] F. Huster, *Investigation of the alloying of screen printed aluminium pastes for the BSF formation on silicon solar cells*, in Proc. 20th EUPVSEC, Barcelona, Spain, pp. 1466-1469 (2005).
- [22] M. Meuris, *et al.*, *The IMEC clean: A new concept for particle and metal removal on Si surfaces*, Solid State Technology **38**, 109 (1995).
- [23] Y. Ein-Eli, N. Gordon, and D. Starosvetsky, *Reduced light reflection of textured multicrystalline silicon via NPD for solar cells applications*, Sol. Energy Mater. Sol. Cells **90**, 1764 (2006).
- [24] E. Yablonovitch and G. D. Cody, *Intensity enhancement in textured optical sheets for solar cells*, IEEE Trans. Electron Dev. **29**, 300 (1982).

- [25] D. Macdonald, *Texturing industrial multicrystalline silicon solar cells*, Solar Energy **76**, 277 (2004).
- [26] B. Sopori, *Reflection characteristics of textured polycrystalline silicon substrates for solar cells*, Solar cells **25**, 15 (1988).
- [27] Y. Komatsu, A. F. Stassen, P. Venema, A. H. G. Vlooswijk, C. Meyer, and M. Koorn, *Sophistication of doping profile manipulation-emitter performance improvement without additional process step-*, in Proc. 25th EUPVSEC, Valencia, pp. 1924-1929 (2010).
- [28] B. J. Baliga and S. K. Ghandhi, *PSG masks for diffusions in gallium arsenide*, IEEE Trans. Electron Dev. **19**, 761 (1972).
- [29] D. Biro, *Durchlaufdiffusion für die Photovoltaik*, Ph.D. Thesis, University of Freiburg (2003)
- [30] A. Bentzen, *Phosphorus diffusion and gettering in silicon solar cells*, Ph.D. Thesis, University of Oslo (2006).
- [31] W. O'Mara, R. B. Herring, and L. P. Hunt, *Handbook Of Semiconductor Silicon Technology*, Crest Publishing House, South Africa (2007).
- [32] C. D. Salzberg and J. J. Villa, *Infrared Refractive Indexes of Silicon Germanium and Modified Selenium Glass* **47**, 244 (1957).
- [33] M. A. Green, *Solar cells: Operating principles, technology, and system applications*, Englewood Cliffs, NJ, Prentice-Hall, Inc. (1982).
- [34] R. Santbergen, *Optical absorption factor of solar cells for PVT systems*, PhD Thesis, Technische Universiteit Eindhoven (2008).
- [35] A. G. Aberle, *Crystalline silicon solar cells: advanced surface passivation and analysis*, University of New South Wales, Sydney NSW 2052, Australia (1999).
- [36] M. A. Green, *Ag requirements for silicon wafer-based solar cells*, Prog. Photovoltaics **19**, 911 (2011).
- [37] G. Schubert, F. Huster, and P. Fath, *Physical understanding of printed thick-film front contacts of crystalline Si solar cells-Review of existing models and recent developments*, Sol. Energy Mater. Sol. Cells **90**, 3399 (2006).

- [38] A. Schneider, R. Kopecek, G. Hahn, S. Noel, and P. Fath, *Comparison of gettering effects during phosphorus diffusion for one-and double-sided emitters*, in Proc. 31st IEEE PVSC IEEE, pp. 1051-1054 (2005).
- [39] D. Kray, S. Hopman, A. Spiegel, B. Richerzhagen, and G. P. Willeke, *Study on the edge isolation of industrial silicon solar cells with waterjet-guided laser*, Sol. Energy Mater. Sol. Cells **91**, 1638 (2007).
- [40] <http://www.merck-chemicals.com>
- [41] W. van Gelder, and V. E. Hauser, *The Etching of Silicon Nitride in Phosphoric Acid with Silicon Dioxide as a Mask*, J. Electrochem. Soc. **114**, 869 (1967).
- [42] P. Ferrada, R. Harney, E. Wefringhaus, J. Lossen, and K. Meyer, *Diffusion through semitransparent barriers on p-type silicon wafers*, in Proc. 24th EUPVSEC, Hamburg, pp. 1897-1900 (2009).
- [43] A. E. Becquerel, *Mémoire sur les effets électriques produits sous l'influence des rayons solaires*, Comptes Rendus **9**, 561 (1839).
- [44] M. Riordan and L. Hoddeson, *The origins of the pn junction*, IEEE Spectrum **34**, 46 (1997).
- [45] G. W. Pickard, *Means for receiving intelligence communicated by electric waves*, U.S. Patent 836531 (1906).
- [46] R. S. Ohl, *Light-sensitive electric device*, U.S. Patent 2402662 (1946).
- [47] W. Shockley and H. J. Queisser, *Detailed Balance Limit of Efficiency of p-n Junction Solar Cells*, J. Appl. Phys. **32**, 510 (1961).
- [48] T. Tiedje, E. Yablonovitch, G. D. Cody, and B. G. Brooks, *Limiting efficiency of silicon solar cells*, IEEE Trans. Electron Dev. **31**, 711 (1984).
- [49] M. A. Green, *Limits on the open-circuit voltage and efficiency of silicon solar cells imposed by intrinsic Auger processes*, IEEE Trans. Electron Dev. **31**, 671 (1984).
- [50] M. A. Green, *Accuracy of analytical expressions for solar cell fill factors*, Solar Cells **7**, 337 (1982).
- [51] E. Sanchez and G. Araujo, *On the analytical determination of solar cell fill factor and efficiency*, Solar Cells **20**, 1 (1987).
- [52] S. M. Sze, and K. K. Ng, *Physics of semiconductor devices*, John Wiley & Sons, Inc., Hoboken, NJ, USA. (2006).

- [53] S. R. Wenham, M. A. Green, M. E. Watt, and R. Corkish, *Applied Photovoltaics*, Centre for Photovoltaic Devices and Systems, Sydney, pp. 47-49 (2007).
- [54] R. Fowler, *The Analysis of Photoelectric Sensitivity Curves for Clean Metals at Various Temperatures*, *Physical Review* **38**, 45 (1931).
- [55] B. Fischer, *Loss Analysis of Crystalline Silicon Solar Cells using Photoconductance and Quantum Efficiency Measurements*, Ph.D Thesis, University of Konstanz (2003).
- [56] P. A. Basore, *Extended spectral analysis of internal quantum efficiency*, in Proc. 23th IEEE PVSC, pp. 147-152 (1993).
- [57] M. A. Green, *High Efficiency Silicon Solar Cells*, Trans Tech Publications, Switzerland (1987).
- [58] M. D. Lammert, R. J. Schwartz, *The interdigitated back contact solar cell: A silicon solar cell for use in concentrated sunlight*, *IEEE Trans. Electron Devices* **24**, 337 (1977).
- [59] C. P. Sealy, M. R. Castell, and P. R. Wilshaw, *Mechanism for secondary electron dopant contrast in the SEM*, *J. Electron Microsc.* **49**, 311 (2000).
- [60] G. J. Russell, M. J. Robertson, B. Vincent, and J. Woods, *An electron beam induced current study of grain boundaries in zinc selenide*, *J. Mater. Sc.* **15**, 939 (1980).
- [61] F. Greuter and G. Blatter, *Electrical properties of grain boundaries in polycrystalline compound semiconductors*, *Semicond. Sci. Tech.* **5**, 111 (1990).
- [62] B. S. Mitchell, *An introduction to materials engineering and science*, Wiley Online Library (2004).
- [63] D. K. Schroder, and D.L. Meier, *Solar cell contact resistance-A review*, *IEEE Trans. Electron. Dev.* **31**, 637 (1984).
- [64] F. Kröger, G. Diemer, and H. Klasens, *Nature of an Ohmic Metal-Semiconductor Contact*, *Phys. Rev.* **103**, 279 (1956).
- [65] A. Goetzberger, J. Knobloch, and B. Voß, *Physik und Technologie der Solarzelle*, Teubner-Verlag, Stuttgart (1994).
- [66] J. P. Colinge and C. A. Colinge, *Physics of semiconductor devices*, Kluwer Academic Publishers, USA (2002).

- [67] C. Y. Chang, and Y. K. Fang, *Specific contact resistance of metal-semiconductor barriers*, Solid-State Electron. **14**, 541 (1971).
- [68] P. Gutknecht, *Schottky barrier height dependence on Si crystal orientation*, Appl. Phys. Lett. **21**, 405 (1972).
- [69] E. Cabrera, S. Olibet, J. Glatz-Reichenbach, R. Kopecek, D. Reinke, and G. Schubert, *Experimental evidence of direct contact formation for the current transport in silver thick film metallized silicon emitters*, J. Appl. Phys. **110**, 114511 (2011).
- [70] C. J. Kircher, *Contact metallurgy for shallow junction Si devices*, J. Appl. Phys. **47**, 5394 (1976).
- [71] J. McCarthy, *Failure of aluminium contacts to silicon in shallow diffused transistors*, Microelectronics and Reliability **9**, 187 (1970).
- [72] D. K. Schroder, *Semiconductor material and device characterization*, John Wiley and Sons (1990).
- [73] H. H. Berger, *Contact Resistance and Contact Resistivity*, J. Electrochem. Soc. **119**, 507 (1972).
- [74] H. H. Berger, *Models for contacts to planar devices*, Solid-State Electron. **15**, 145 (1972).
- [75] F. M. Smits, *Measurement of sheet resistivities with the four-point probe*, Bell Syst. Tech. J. **37**, 711 (1958).
- [76] M. S. Tyagi and R. V. Overstraeten, *Minority carrier recombination in heavily-doped silicon*, Solid-St. Electron. **26**, 577 (1983).
- [77] M. J. Kerr and A. Cuevas, *General parameterization of Auger recombination in crystalline silicon*, J. Appl. Phys. **91**, 2473 (2002).
- [78] J. Dziewior and W. Schmid, *Auger coefficients for highly doped and highly excited silicon*, Appl. Phys. Lett. **31**, 346 (1977).
- [79] A. Luque and S. Hegedus, *Handbook of photovoltaic science and engineering*, John Wiley & Sons Inc (2003).
- [80] W. Shockley and W. Read, *Statistics of the Recombinations of Holes and Electrons*, Phys. Rev. **87**, 835 (1952).
- [81] R. Hall, *Electron-Hole Recombination in Germanium*, Phys. Rev. **87**, 387 (1952).

- [82] A. R. Beattie and P. T. Landsberg, *Auger Effect in Semiconductors*, in Proc. R. Soc. London A **249**, 16 (1959).
- [83] A. B. Sproul, M. A. Green, and A. W. Stephens, *Accurate determination of minority carrier- and lattice scattering-mobility in silicon from photoconductance decay*, J. Appl. Phys **72**, 4161 (1992).
- [84] J. Schmidt, A. Merkle, R. Brendel, B. Hoex, M.C.M. van de Sanden, and W.M.M. Kessels, *Surface passivation of high-efficiency silicon solar cells by atomic-layer-deposited Al<sub>2</sub>O<sub>3</sub>*, Prog. Photovolt. **16**, 461 (2008).
- [85] S. Gatz, K. Bothe, J. Müller, T. Dullweber, R. Brendel, *Analysis of local Al-doped back surface fields for high efficiency screen-printed solar cells*, Energy Procedia (to be published) (2011).
- [86] M. A. Green, M. J. Keevers, *Optical properties of intrinsic silicon at 300 K*, Prog. Photov. **3**, 189 (1995).
- [87] R. Chaoui, A. Messaoud, *Screen-printed solar cells with simultaneous formation of porous silicon selective emitter and antireflection coating*, Desalination **209**, 118 (2007).
- [88] J. H. Bultman, R. Kinderman, J. Hoornstra, M. Koppes, *Single step selective emitter using diffusion barriers*, in Proc. 16th EPVSEC, Glasgow, pp. 1424-1426 (2000).
- [89] F. Book, B. Raabe, and G. Hahn, *Two Diffusion Step Selective Emitter*, in Proc. 23rd EUPVSEC, Valencia, pp. 5-8 (2010).
- [90] J. Szlufcik, J. Horzel, F. Duerinckx, R. Einhaus, E. Demesmaeker, J. Nijs, and R. Mertens, *Selective-emitter solar cells - from laboratory to production processes*, in Proc. of the 8th Workshop on Crystalline Silicon Solar Cell Materials and Processing, Copper Mountain, Belgium pp. 69-76 (1998).
- [91] N. Stem, and M. Cid, *Physical limitations for homogeneous and highly doped n-type emitter monocrystalline silicon solar cells*, Solid-St. Electron. **48**, 197 (2004).
- [92] K. Peter, R. Kopecek, A.K. Sjøiland, E. Enebak, *Future Potential for SoG-Si Feedstock from the Metallurgical Process Route*, in Proc. 23th EUPVSEC, Valencia, Spain, pp. 947-950 (2008).

- [93] J. Mandelkorn, J. H. Lamneck, Jr., *Simplified fabrication of back surface electric field silicon cells and novel characteristics of such cells*, in Proc. 9th IEEE Photovoltaic Spec. Conf., IEEE, New York, 66 (1972).
- [94] M. Wolf, *Drift fields in photovoltaic solar energy converter cells*, in Proc. of the IEEE **51**, 674-693 (1963).
- [95] P. L. Lölgén, *Surface and volume recombination in silicon solar cells*, PhD Thesis, Universiteit Utrecht (1995).
- [96] J. del Alamo, J. Eguren, and A. Luque, *Operating limits of Al-alloyed high-low junctions for BSF solar cells*, Solid-St. Electron. **24**, 5 (1981).
- [97] J. Mandelkorn and J. H. Lamneck Jr., *A new electric field effect in silicon solar cells*, J. Appl. Phys. **44**, 4785 (1973).
- [98] J. Mandelkorn, J. H. Lamneck, Jr., *Simplified fabrication of back surface electric field silicon cells and novel characteristics of such cells*, Solar Cells **29**, 121 (1990).
- [99] S. Narasimha, A. Rohatgi, and A.W. Weeber, *An optimized rapid aluminum back surface field technique for silicon solar cells*, IEEE Trans. Electron Devices **46**, 1363 (1999).
- [100] J. Mandelkorn, J. H. Lamneck, Jr., *Advances in the theory and application of BSF cells*, in Proc. of 11th Photovoltaic Specialists Conference, (1975).
- [101] P. A. Basore, *Numerical modeling of textured silicon solar cells using PC-1D*, IEEE Trans. Electron Dev. **37**, 337 (1990).
- [102] P. G. Shewmon, *Diffusion in Solids*, McGraw-Hill Book Co., New York (1963).
- [103] P. Choulat, Y. Ma, B. T. Chan, J. John, H. Nagel, J. Horzel, S. Forment, G. Agostinelli, and G. Beaucarne, *High efficiency industrial type PERC Solar Cell on very thin EFG Substrates*, in Proc. 23rd EUPVSEC, Valencia, Spain, pp. 1-5 (2008).
- [104] I. Romijn, A. A. Mewe, M. W. P. E. Lamers, E. Kossen, E. Bende, A. W. Weeber, *An Overview of MWT Cells and Evolution to the ASPIRe Concept: A New Integrated mc-Si Cell and Module Design for High-Efficiencies*, in Proc. 23rd EUPVSEC, Valencia, Spain, pp. 1000-1005 (2008).

- [105] J. Nijs, *Overview of solar cell technologies and results on high efficiency multicrystalline silicon substrates*, Sol. Energy Mater. Sol. Cells **48**, 199 (1997).
- [106] A. Cuevas, M. Stocks, D. McDonald, M. Kerr, and C. Samundsett, *Recombination and trapping in multicrystalline silicon*, IEEE Trans. Electron Dev. **46**, 2026 (1999).
- [107] H. C. Fang, C. C. Chang, C. P. Liu, H. S. Chung, and C. L. Huang, *Effects of Back Surface Textures on Contact Formation and Solar Cell Performance*, J. Electrochem. Soc. **157**, p. H246 (2010).
- [108] A. Rohatgi, Z. Chen, P. Doshi, T. Pham, and D. Ruby, *High-efficiency silicon solar cells by rapid thermal processing*, Appl. Phys. Lett. **65**, 2087 (1994).
- [109] G. Santana, A. Morales-Acevedo, and L. Hernandez, *Gettering effects by aluminum upon the dark and illuminated I-V characteristics of N<sup>+</sup>-P-P<sup>+</sup> silicon solar cells*, Sol. Energy Mater. Sol. Cells **62**, 369 (2000).
- [110] V. A. Popovich, M. Janssen, I.M. Richardson, T. van Amstel, and I.J. Bennett, *Microstructure and mechanical properties of aluminum back contact layers*, Sol. Energy Mater. Sol. Cells **95**, 93 (2011).
- [111] J. G. Fossum, *Physical operation of back-surface-field silicon solar cells*, IEEE Trans. Electron Devices **24**, 322 (1977).
- [112] P. Würfel, *Physics of Solar Cells, From Basic Principles to Advanced Concepts*, Wiley-Vch Verlag GmbH & Co. KgaA, Weinheim, Germany (2009).
- [113] J. L. Murray, and A. J. McAlister, *The Al-Si (Aluminum-Silicon) system*, J. Phase Equilibria **5**, 74 (1984).
- [114] M. Warmuzek, *Aluminum-Silicon Casting Alloys: Atlas of Microfractographs*, ASM International, Materials Park, OH, pp.1-2 (2004).
- [115] R. A. Gudmundsen and J. Maserjian Jr., *Semiconductor Properties of Recrystallized Silicon in Aluminum Alloy Junction Diodes*, J. Appl. Phys. **28**, 1308 (1957).
- [116] L. Sardi, S. Bargioni, C. Canali, P. Davoli, M. Prudenziati, V. Valbusa, *Some features of thick film technology for the back metallization of solar cells*, Solar cells **11**, 51 (1984).
- [117] J. O. McCaldin and H. Sankur, *Precipitation of Si from the Al Metallization of Integrated Circuits*, Appl. Phys. Lett. **20**, 171 (1972).

- [118] P. Walker and W. H. Tarn, *CRC Handbook Of Metal Etchants*, CRC Press, Boca Raton, FL (1991).
- [119] H. Plagwitz, and R. Brendel, *Analytical model for the diode saturation current of point-contacted solar cells*, Prog. Photovoltaics **14**, 1 (2006).
- [120] S. M. Yang, and J. Plá, *Optimization of the back contact in c-Si solar cells*, Solid-St. Electron. **53**, 925 (2009).
- [121] J. Müller, K. Bothe, S. Gatz, F. Haase, C. Mader, and R. Brendel, *Recombination at laser-processed local base contacts by dynamic infrared lifetime mapping*, J. Appl. Phys. **108**, 124513 (2010).
- [122] A. W. Y. Ho, and S. R. Wenham, *Fabrication of silicon solar cells with rear pinhole contacts*, Sol. Energy Mater. Sol. Cells **91**, 1234 (2007).
- [123] A. Uruëña, J.L. Hernández, J. John, J. Poortmans, and R. Mertens, *Controlling the Depth of the Local Al BSF in PERC Crystalline Solar Cells Using Alternative Back Side Metallization*, in Proc. 25th EUPVSEC, Hamburg, pp. 2562-2564 (2010).
- [124] F. S. Grasso, L. Gautero, J. Rentsch, R. Preu, and R. Lanzafame, *Characterisation of Local Al-BSF Formation for PERC Solar Cell Structures*, in Proc. 25th EUPVSEC, Hamburg, pp. 371-374 (2010).
- [125] J. Krause, R. Woehl, and D. Biro, *Analysis of Local Al-p<sup>+</sup>-Layers for Solar Cells Processed by Small Screen-Printed Structures*, in Proc. 25th EUPVSEC, Hamburg, pp. 1899-1904 (2010).
- [126] A. Kaminski, B. Vandellea, A. Fave, J. P. Boyeaux, L. Q. Nam, R. Monna, D. Sarti, A. Laugier, *Aluminium BSF in silicon solar cells*, Sol. Energy Mater. Sol. Cells **72**, 373 (2002).
- [127] G. Beaucarne, *Local Al-alloyed contacts for next generation Si solar cells*, presentation at the first Workshop on Metallization for Crystalline Silicon Solar Cells, Utrecht, The Netherlands (2008).
- [128] A. Uruëña, J. John, G. Beaucarne, P. Choulat, P. Eybe, and G. Agostinelli, *Local Al-alloyed contacts for next generation Si solar cells*, in Proc. 24rd EUPVSEC, Hamburg, pp. 1483-1486 (2009).
- [129] U. Zastrow, L. Houben, D. Meertens, A. Grohe, T. Brammer, and E. Schneiderlöchner, *Characterization of laser-fired contacts in PERC solar cells:*

- SIMS and TEM analysis applying advanced preparation techniques*, Appl. Surface Science **252**, 7082 (2006).
- [130] E. E. Bende, I. Cesar, I. Romijn, and A. W. Weeber, *Open-rear side H-pattern optimization based on 2D computer simulations*, in Proc. 33rd IEEE PVSC, San Diego, pp. 1-6 (2008).
- [131] R. Bock, J. Schmidt, R. Brendel, H. Schuhmann, and M. Seibt, *Electron microscopy analysis of crystalline silicon islands formed on screen-printed aluminum-doped p-type silicon surfaces*, J. Appl. Phys. **104**, 043701 (2008).
- [132] J. M. Ford, *Al/Poly Si specific contact resistivity*, IEEE Electron Dev. Lett. **4**, 255 (1983).
- [133] M. Melczarsky, G. G. Garcia, N. E. Posthuma, E. Van Kerschaver, and G. Beaucarne, *Contact resistance measurement techniques for Ag thick-film screen-printed contacts to solar cells*, in Proc. 34th IEEE Photovoltaic Specialists Conference (PVSC), pp. 960-963, (2009).
- [134] M. Finetti, P. Ostojca, S. Solmi, and G. Soncini, *Aluminum-silicon ohmic contact on 'shallow'  $n^+ / p$  junctions*, Solid-State Electron. **23**, 255 (1980).
- [135] V. D. Kurochkin, L. P. Kravchenko, L. N. Kuzmenko, and L. A. Tsurpal, *Structural Effects in Determining Silicon Concentration in Al-Si Alloys by X-Ray Fluorescence and Mass Spectrometry*, Powder Metall. Met. C+ **44**, 191 (2005).
- [136] A. Paccagnella, G. Ottaviani, P. Fabri, G. Ferla, and G. Queirolo, *Silicon diffusion in aluminium*, Thin Solid Films **128**, 217 (1985).
- [137] J. O. McCaldin, *Diffusivity and solubility of Si in the Al metallization of integrated circuits*, Appl. Phys. Lett. **19**, 524 (1971).
- [138] T. Lauermann, T. Lüder, S. Scholz, B. Raabe, G. Hahn, B. Terheiden, *Enabling dielectric rear side passivation for industrial mass production by developing lean printing-based solar cell processes*, in Proc. 35th IEEE PVSC, Hawaii, pp. 28-33 (2010).
- [139] T. Chung, *Study of Aluminum Fusion into Silicon*, J. Electrochem. Soc. **109**, 3 (1962).
- [140] M. Rauer *et al.*, *Aluminum Alloying in Local Contact Areas on Dielectrically Passivated Rear Surfaces of Silicon Solar Cells*, IEEE Electron Device Letters **32**, 916 (2011).

- [141] S. I. Fujikawa, K. I. Hirano, and Y. Fukushima, *Diffusion of silicon in aluminum*, Metall. Trans. A **9**, 1811 (1978).
- [142] A. Paul, *The Kirkendall effect in solid state diffusion*, Ph.D Thesis, Technische Universiteit Eindhoven (2004).
- [143] E. O. Kirkendall, *Diffusion of zinc in alpha brass*, Transaction AIME **147**, 104 (1942).
- [144] L. Zhang, S. Ou, J. Huang, K. N. Tu, S. Gee, and L. Nguyen, *Effect of current crowding on void propagation at the interface between intermetallic compound and solder in flip chip solder joints*, Appl. Phys. Lett. **88**, 012106 (2006).
- [145] C. Chen, H. M. Tong, and K. N. Tu, *Electromigration and thermomigration in Pb-free flip-chip solder joints*, Annu. Rev. Mater. Res. **40**, 531 (2010).
- [146] R. Lathrop, *Avoiding the solder void*, in Proc. of APEX Anaheim, CA, pp. S02-2-1-S02-2-7 (2003).
- [147] G. Li, Z. Zhan, L. Wang, L. Cao, L. Sun, D. Dai, J. Zhang, and W. Wang, *Effects of gravity on the microstructure of  $Zr_{41}Ti_{14}Cu_{12.5}Ni_{10}Be_{22.5}$  bulk glass forming alloy*, Chin. Sci. Bull. **46**, 11 (2001).
- [148] J. Müller, K. Bothe, S. Gatz, H. Plagwitz, G. Schubert, R. Brendel, *Contact Formation and Recombination at Screen-Printed Local Aluminum-Alloyed Silicon Solar Cell Base Contacts* IEEE Trans. Electron Dev. **58**, 3239 (2011).
- [149] V. Meemongkolkiat *et al.*, *Investigation of modified screen printing Al pastes for local back surface field formation*, in Proc. 4th IEEE WCPVEC, Hawaii, pp. 1338-1341 (2006).
- [150] T. Lauer mann, A. Zuschlag, S. Scholz, G. Hahn, B. Terheiden, *The Influence of Contact Geometry and Sub-Contact Passivation on the Performance of Screen-Printed  $Al_2O_3$  Passivated Solar Cells*, in Proc. 26th EUPVSEC, Hamburg, pp. 1137-1143 (2011).
- [151] D. Macdonald, A. Cuevas, and F. Ferrazza, *Response to phosphorus gettering of different regions of cast multicrystalline silicon ingots*, Solid-St. Electron. **43**, 575 (1999).
- [152] C. Teichert, J. F. MacKay, D. E. Savage, M. G. Lagally, M. Brohl, and P. Wagner, *Comparison of surface roughness of polished silicon wafers*

- measured by light scattering topography, soft-x-ray scattering, and atomic-force microscopy*, Appl. Phys. Lett. **66**, 2346 (1995).
- [153] J. D. Hylton, *Light coupling and light trapping in alkaline etched multicrystalline silicon wafers for solar cells*, PhD Thesis, Utrecht University (2006).
- [154] M. Hofmann, C. Schmidt, N. Kohn, J. Rentsch, S. Glunz, and R. Preu, *Stack system of PECVD amorphous silicon and PECVD silicon oxide for silicon solar cell rear side passivation*, Prog. Photovoltaics **16**, 509 (2008).
- [155] S. Kontermann, A. Wolf, D. Reinwand, A. Grohe, D. Biro, and R. Preu, *Optimizing Annealing Steps for Crystalline Silicon Solar Cells with Screen Printed Front Side Metallization and an Oxide - Passivated Rear Surface with Local Contacts*, Prog. Photovoltaics **17**, 554 (2009).
- [156] R. A. Sinton and A. Cuevas, *Contactless determination of current-voltage characteristics and minority-carrier lifetimes in semiconductors from quasi-steady-state photoconductance data*, Appl. Phys. Lett. **69**, 17 (1996).
- [157] S. Su, F. Chen, and D. Dutta, *Surface Textured Implants*, US Patent 20100114303 (2009).
- [158] P. Ferrada, PhD Thesis, Universität Konstanz (to be published).
- [159] A. Halm, L. M. Popescu, J. Theobald, K. Peter, R. Kopecek, *Low Temperature Pads on Al-Emitter or Al-BSF*, in Proc. 24th EUPVSEC, Hamburg, pp. 1462-1464 (2009).
- [160] R. Kopecek, A. Halm, L. Popescu, K. Peter, M. A. Vázquez, *Industrial large area n-type solar cells with aluminium rear emitter with stable efficiencies*, in Proc. 35th IEEE PVSC, Honolulu, HI, pp. 001423-001426 (2010).
- [161] P. Grunow, *Soldering of Crystalline Silicon Modules: Losses, Reliability and Improvements*, in Proc. 2nd Workshop on Metallization, Konstanz, pp. 59-62 (2010).
- [162] S. Wenham and M. A. Green, *Dry Phosphorus Silicate Glass Etching for Multicrystalline Silicon Solar Cells*, Prog. Photovoltaics **11**, 445 (1996).
- [163] A. Wolf, *et al.*, *The SiNTO process: Utilizing a SiNx anti-reflection layer for emitter masking during Thermal Oxidation*, in Proc. 34th IEEE PVSC, Philadelphia, pp. 534-539.

- [164] M. Rinio, H. J. Möller, and M. Werner, *LBIC Investigations of the Lifetime Degradation by Extended Defects in Multicrystalline Solar Silicon*, Solid State Phenomena **63-64**, 115 (1998).
- [165] L. Mittelstädt, S. Dauwe, A. Metz, R. Hezel, and C. Häßler, *Front and rear silicon-nitride-passivated multicrystalline silicon solar cells with an efficiency of 18.1%*, Prog. Photovoltaics **10**, 35 (2002).
- [166] G. Blatter and F. Greuter, *Carrier transport through grain boundaries in semiconductors*, Phys. Rev. B **33**, 3952 (1986).
- [167] S. Dauwe, L. Mittelstädt, A. Metz, and R. Hezel, *Experimental evidence of parasitic shunting in silicon nitride rear surface passivated solar cells*, Prog. Photovoltaics **10**, 271 (2002).
- [168] I. Cesar, E. E. Bende, G. Galbiati, L. Janßen, A. A. Mewe, P. Manshanden, A. W. Weeber, and J. H. Bultman, *Parasitic shunt losses in all-side SiNx passivated mc-Si solar cells*, in Proc. 24th EUPVSEC, Hamburg, pp. 21-25 (2009).

## LIST OF FIGURES

1.1	Rear passivated solar cell structure and aluminum rear side . . . . .	4
2.1	Principle of a quarter wavelength antireflection coating . . . . .	13
2.2	Etching rate of SiNx by HF and of Si by NaOH . . . . .	17
3.1	Total series resistance losses . . . . .	26
3.2	Recombination in semiconductors . . . . .	31
3.3	Absorption coefficient of Si and penetration depth . . . . .	34
4.1	Flow diagram sequence of the selective emitter process . . . . .	39
4.2	Optical fiducial alignment . . . . .	41
4.3	Dielectric ablation and screen printer alignment . . . . .	41
4.4	EQE and Voc gain for the selective emitter process . . . . .	43
5.1	Influence of the BSF effect on the charge carriers . . . . .	48
5.2	PC1D numerical simulations of the BSF effect on Voc . . . . .	50
5.3	Al-Si equilibrium diagram . . . . .	52
5.4	Model of contact formation between Al and Si . . . . .	53
5.5	SEM micrographs of the Al-Si alloying junction . . . . .	55
5.6	Lamellar structure of Al-Si alloy . . . . .	56
5.7	Peeling off of the Al fingers . . . . .	57
6.1	Model of the alloyed junction of Al lines on dielectric openings . . . . .	62
6.2	TLM result of the contact and line resistance for different Al line widths . . . . .	64
6.3	Contact resistivity variation . . . . .	66
6.4	SEM micrographs of Al-Si alloying junction for different contact areas . . . . .	68
6.5	Model to calculate the real Al-Si contact surface . . . . .	71
6.6	SEM micrographs of the contact area after HCl etching . . . . .	73
6.7	Rear passivated solar cell in cross section . . . . .	74
6.8	Temperature linear dependency of the spread limit of Si . . . . .	76
6.9	SEM/EDX analysis of Si distribution in Al . . . . .	77
6.10	Schematic model of contact formation for narrow contact areas . . . . .	80
6.11	SEM micrographs of samples with different contact spacings . . . . .	83
6.12	SEM micrographs of eutectic and void . . . . .	84
6.13	EDX line analysis of the Si content in the Al matrix . . . . .	84

---

6.14	EDX volume analysis of distribution of Si in the thick Al layer . . . . .	86
6.15	Hypothesis of lateral solidification . . . . .	87
6.16	Model of the local Al-Si contact and influence of gravity . . . . .	89
6.17	SEM micrographs of the influence of gravity on solidification . . . . .	91
6.18	Simple scheme of void formation . . . . .	94
6.19	SEM micrographs of two types of voids found . . . . .	95
7.1	Study on the roughness of polishing surfaces . . . . .	103
7.2	Reflectivity measurements for different surfaces . . . . .	105
7.3	The influence of the boat position on the homogeneity of the emitter .	106
7.4	SEM micrograph of Ag pads and ribbon peel off test . . . . .	108
7.5	Ag pads after the peel off test performed to monitor the bonding force	109
7.6	I-V characteristic results for study 1 . . . . .	114
7.7	EL-analysis of dislocations in rear passivated mc-Si solar cell . . . . .	116
7.8	LBIC map of rear passivated solar cell . . . . .	117
7.9	I-V results for reference and device structures for study 2 . . . . .	121
7.10	FF analysis depending on Ag paste amount and printing sequence .	123
7.11	Spectral response analysis . . . . .	125
7.12	High efficiency solar cell process and spectral response . . . . .	128
7.13	EI-analysis of an Al-BSF and a PERC solar cell . . . . .	130

## LISTS OF ACRONYMS AND SYMBOLS

The following list aims to help the reader, resuming the acronyms, symbols and some definitions used throughout this thesis.

<b>Acronym</b>	<b>Description</b>
Ag	Silver
Al	Aluminum
AM1.5	Air mass 1.5
ARC	Anti-reflection coating
BSF	Back-surface-field
c-Si	Crystalline silicon
Cz-Si	Czochralski crystalline silicon material
Dev.	Device
EDS/EDX	Energy dispersive X-ray spectrometry
EG-Si	Electronic-grade silicon
EL	Electroluminescence
EQE	External quantum efficiency
FS	Front side of device
FSF	Front surface field
GaAs	Gallium arsenide
GB	Grain boundaries
Ge	Germanium
IQE	Internal quantum efficiency
ISC-Konstanz	International Solar Energy Research Center Konstanz
<i>I-V</i>	Current-voltage characteristic
LBIC	Light beam induced current
mc-Si	Multicrystalline silicon material
N	Nitride
NH <sub>3</sub>	Ammonia
O	Oxygen
P	Phosphorus
PECVD	Plasma-enhanced chemical vapor deposition
PERC	Passivated emitter and rear cell

Acronym	Description
POCl <sub>3</sub>	Phosphorous oxychloride
PSG	Phosphorous silicate glass
PV	Photovoltaics
QE	Quantum efficiency
QSSPC	Quasi steady state photoconductance
R	Reflectivity
$R_{min}$	Minimum of Reflection
Ref.	Reference
RS	Rear side of device
RT	Room temperature at 300 K
SEM	Scanning electron microscopy
Si	Silicon
SiH <sub>4</sub>	Silane
SiN <sub>x</sub>	Silicon nitride
SoG-Si	Solar grade silicon
SR	Spectral response (responsivity)
TLM	Transmission line method

Symbol	Description	Unit
$A$	Area	[cm <sup>2</sup> ]
$\alpha$	Absorption coefficient	[cm <sup>-1</sup> ]
$c$	Speed of light in vacuum	[cm/s]
$D$	Diffusion coefficient or diffusivity	[cm <sup>2</sup> /s]
$d$	Etching depth	[ $\mu$ m]
$d_i$	Thickness, length	[ $\mu$ m]
$d_p$	Contact spacing	[ $\mu$ m]
$d_1$	Contact size (dielectric window)	[ $\mu$ m]
$d_2$	Spread of Si in Al, or Al finger width	[ $\mu$ m]
$E_g$	Energy bandgap	[eV]
$E_C$	Conduction band	[eV]
$E_V$	Valence band	[eV]
$E_F$	Fermi level	[eV]
$FF$	Fill factor	[%]
$I_{ph}$	Photocurrent	[A]
$I_0$	Dark saturation current	[A]

Symbol	Description	Unit
$J_{SC}$	Short-circuit current	[mA/cm <sup>2</sup> ]
$J_O$	Reverse saturation current	[mA/cm <sup>2</sup> ]
$k$	Wave vector	[cm <sup>-1</sup> ]
$L$	Diffusion length	[μm]
$g$	Gravity field orientation	
$L_{eff}$	Effective carrier diffusion length	[μm]
$L_R$	Line resistance	[Ω/cm]
$N$	Excess carrier concentration	[cm <sup>-3</sup> ]
$n$	Concentration of free electron	[cm <sup>-3</sup> ]
$n$	Normal direction of solidification	
$n_i$	Refractive index	
$n_{opt}$	Refractive index of Si	
$N_A$	Ionized acceptor impurity concentration	[cm <sup>-3</sup> ]
$N_D$	Ionized donor impurity concentration	[cm <sup>-3</sup> ]
$\rho$	Concentration of free hole	[cm <sup>-3</sup> ]
$P_{opt}$	Optical power ( $P_{opt} = \Phi_{in} h\nu$ )	[W]
$P_{mp}$	Maximum output power point	[W]
$R_S$	Series resistance	[Ωcm <sup>2</sup> ]
$R_P$	Shunt resistance	[Ωcm <sup>2</sup> ]
$R_{SH}$	Sheet resistance	[Ω/□]
$R_C$	Contact resistance	[Ω]
$R$	Total recombination rate	[cm <sup>-3</sup> -s <sup>-1</sup> ]
$S_{dr}$	Surfaces area ratio	[nm]
$S_{eff}$	Back surface recombination velocity	[cm/s]
$S_f$	Front surface recombination velocity	[cm/s]
S/L	Solid/liquid interface	
$T$	Absolute temperature	[°C]
$T_{eut}$	Eutectic temperature	[°C]
$T_{melt}$	Melting temperature	[°C]
$V_{OC}$	Open-circuit voltage	[mV]
$W$	Solar cell base thickness	[μm]
$x_j$	Junction depth	[μm]
$\eta$	Conversion efficiency	[%]
$\rho_c$	Contact resistivity	[mΩcm <sup>2</sup> ]
$\Phi_{in}$	Photon flux	[s <sup>-1</sup> ]

Symbol	Description	Unit
$\lambda$	Wavelength	[nm]
$h\nu$	Photon energy	[eV]
$\nu$	Frequency of light	[Hz]
$\rho$	Resistivity	[ $\Omega$ -cm]
$\sigma$	Conductivity	[S-cm <sup>-1</sup> ]
$\mu_n$	Electron mobility	[cm <sup>2</sup> /V-s]
$\mu_p$	Hole mobility	[cm <sup>2</sup> /V-s]
$\tau$	Lifetime	[ $\mu$ s]

Constants	Quantity	Value
$h$	Planck constant	$4.1357 \times 10^{-15}$ eV-s
$k$	Boltzmann constant	$8.6174 \times 10^{-5}$ eV/K
$q$	Elementary charge	$1.60218 \times 10^{-19}$ C

# LIST OF PUBLICATIONS

## Refereed Journal Papers

- E. Urrejola, K. Peter, H. Plagwitz, and G. Schubert, *Al-Si alloy formation in narrow p-type Si contact areas for rear passivated solar cells*, Journal of Applied Physics, vol. **107**, 124516 (2010).
- E. Urrejola, K. Peter, H. Plagwitz, and G. Schubert, *Silicon diffusion in aluminum for rear passivated solar cells*, Applied Physics Letters, vol. **98**, 153508 (2011).
- E. Urrejola, K. Peter, H. Plagwitz, and G. Schubert, *Effect of gravity on the microstructure of Al-Si alloy for rear passivated solar cells*, Journal of Applied Physics, vol. **110**, 056104 (2011).
- E. Urrejola, K. Peter, H. Plagwitz, and G. Schubert, *Distribution of silicon in the aluminum matrix for rear passivated solar cells*, Energy Procedia, vol. **8**, 331 (2011).

## Refereed Conference Proceedings

- E. Urrejola, K. Peter, A. Soiland, and E. Enebak, *POCl<sub>3</sub> diffusion with in-situ SiO<sub>2</sub> barrier for selective emitter multicrystalline solar grade silicon solar cells*, Proceedings of the 24th European Photovoltaic Solar Energy Conference and Exhibition, Hamburg, Germany (2009), pp. 1835-1837.
- E. Urrejola, K. Peter, J.G. Reichenbach, E. Wefringhaus, H. Plagwitz, and G. Schubert, *Al-Si alloy formation in narrow p-Si contact areas*, Proceedings of the 2nd Workshop on Metallization, Constance, Germany (2010), pp. 11-14.
- E. Urrejola, K. Peter, J.G. Reichenbach, E. Wefringhaus, H. Plagwitz, and G. Schubert, *Influence of the Al-Si alloy formation in narrow dielectric barrier openings on the specific contact resistance*, Proceedings of the 25th European Photovoltaic Solar Energy Conference and Exhibition, Valencia, Spain (2010), pp. 2176-2178.

- E. Urrejola, R. Petres, J. Glatz-Reichenbach, K. Peter, H. Plagwitz, G. Schubert, *High efficiency industrial PERC solar cells with all PECVD-based rear surface passivation*, Proceedings of the 26th European Photovoltaic Solar Energy Conference and Exhibition, Hamburg, Germany (2011), pp. 2233-2235.

## Oral Presentations

- *Silicon Solar Cells*, by E. Urrejola *et al.*, "Encuentros: 3rd Conference of Young Chilean Scientists in Europe", Göttingen (Germany), 11.02.2009.
- *Al-Si alloy formation in narrow p-Si contact areas*, by E. Urrejola, 2<sup>nd</sup> Workshop on Metallization for Crystalline Silicon Solar Cells, Constance (Germany), 14.04.2010.
- *Distribution of silicon in the aluminum matrix for rear passivated solar cells*, by E. Urrejola, 1<sup>st</sup> Silicon PV Conference, Freiburg (Germany), 17.04.2011.
- *Understanding and avoiding the formation of voids for rear passivated silicon solar cells*, by E. Urrejola, 3<sup>rd</sup> Workshop on Metallization for Crystalline Silicon Solar Cells, Charleroi (Belgium), 26.10.2011.

## Visual Presentations

- *POCl<sub>3</sub> Diffusion with in-situ SiO<sub>2</sub> barrier for Selective Emitter Multicrystalline Solar Grade Silicon Solar Cells*, by E. Urrejola, 24th European Photovoltaic Solar Energy Conference and Exhibition, Hamburg (Germany), 23.09.2009. Session code: 2CV.5.35.
- *Influence of the Al-Si Alloy formation in narrow dielectric barrier openings on the specific contact resistance*, by E. Urrejola, 25th European Photovoltaic Solar Energy Conference and Exhibition, Valencia (Spain), 08.09.2010. Session code: 2CV.3.31.
- *High efficiency industrial PERC solar cells with all PECVD-based rear surface passivation*, by E. Urrejola, 26th European Photovoltaic Solar Energy Conference and Exhibition, Hamburg (Germany), 07.09.2011, Session code: 2CV.4.34.

## ACKNOWLEDGMENTS

First of all, I would like to thank Professor Ernst Bucher for having traveled to Chile in 2007 to give a talk on solar energy. This opened my eyes and inspired a way forward to my future. From then until today, I have studied and worked in the field of solar energy, bringing good fruits as it is the case of this Thesis. These years of work in the International Solar Energy Research Centre Konstanz (ISC-Konstanz), started as a pleasant learning experience; and resulted with maturity as a scientist. I would like to thank specially Dr. Kristian Peter, for being my advisor and giving to me, with great patience, the guidance needed for this stage of my development.

At the beginning of my Ph.D it was my friend and colleague Dr. Valentin Mihailetchi, who was instrumental in my growth as a scientist. Through his great talent as a scientist he showed me the importance of publishing my ideas and improving my self. He gave me the important feedback I needed.

I would also especially like to thank Dr. Gunnar Schubert for believing in me and giving me the opportunity to take such an interesting project into my own hands. I am also deeply grateful to Dr. Heiko Plagwitz for the fruitful discussions in the microscopic world of physics, which motivated me to publish several articles in scientific magazines, and guide me to reach my established goals. I greatly appreciated their feedback during the development and correction of this thesis.

There have been many people involved, directly or indirectly, in inspiring and facilitating my work in this thesis. Therefore I sincerely thank all the staff of the ISC-Konstanz, and in particular: Lejlja Hildebrand, Annette Helfricht, Dr. Eckard Wefringhaus, Florian Buchholz (thank you for the English corrections), and Pedro Diaz-Perez for their great support. I'd also like to thank Dr. Radovan Kopecek and Rudolf Harney for the efficient and pleasant working environment, Angela Schellinger for her patience, joy and optimism, Stephan Eisert, Engelbert Lemp, and Jens Theobald for their strong technical support, Dr. Joachim Glatz-Reichenbach (thank you for your feedback and coffee breaks during this work), Dr. Lăcră Popescu, Andreas Halm, Lejo Joseph, Christoph Peter, Giuseppe Galbiati, Corrado Comparotto, and Dr. Razvan Roescu, and for their friendship and pleasant moments at work. I would also like to thank my new colleagues from the solar cell research and development department at Sunways AG for their great feedback and atmosphere.

I want to express special thanks to Prof. Peter Nielaba for being chairman of the doctoral committee and many thanks to Prof. Johannes Boneberg for being the second referee of my Ph.D thesis.

After this scientific and technical framework, I would like also to thank my great friends Enrique Cabrera and Pablo Ferrada, for the incredible moments we had during our Ph.D work, when we demonstrated to ourselves that cultural and language barriers are only small doors, which can be fully opened to reveal wonderful new opportunities and possibilities. I would also like to thank my great friend Johannes Theisen for his true friendship and perception, always suggesting different new points of view.

This work would not have been possible without the unconditional support of my girlfriend Susanne Kruza, who has accompanied me on this journey with patience and love. I dedicate this work, with all my love, to my parents Manuel and Susi, and my family in Chile: Bernarda, Luisa, Alberto, Amalia, who illuminate my endeavors with bright light from the distance.

Finally, I hope that this work would be read, quoted and criticized, and never neglected on the dusty library shelves.

Elías Urrejola Davanzo

Konstanz, Germany, November 2011

## CURRICULUM



**Elias Urrejola Davanzo** was born on 21 February 1981 in Santiago de Chile. In March 2000 Elias started his studies of Electrical Engineering at the University of Santiago in Chile in the area of Automatic Control. His scientific connection with Germany began in August 2005, when he was awarded a two semester scholarship at the RWTH-Aachen University by the German Academic Exchange Service (DAAD). After one year in Aachen, towards the end of his scholarship, he started to write his diploma thesis at the Institute of Automatic Control (IRT) entitled: Automation of a Recycling Process. Shortly after finishing his studies in Chile in January 2008, he met Prof. Ernst Bucher, who committed himself to increasing scientists' and politicians' understanding on Chile's important position and potential in renewable energies. Meeting Prof. Bucher marked a turning point in Elias' professional career and consequently he dedicated his work to investigating Solar energy. In May 2008 Elias started to work as a Ph.D student at the International Solar Energy Research Center Konstanz e.V. (Germany), in the area of research and development of high efficiency rear-passivated crystalline silicon solar cells with local back metallization for industrial application. Since August 2011 he works as a scientist in the field of research and development at Sunways AG in Konstanz, Germany.